UNIVERSITY OF TECHNOLOGY SYDNEY

On the Thermal Stability of Ligand-Stabilised Gold Nanoparticles

Shirin Rose King

A thesis submitted for the degree of
Doctor of Philosophy

April 2018

Certificate of Original Authorship

I certify that the work in this thesis has not previously been submitted for a degree nor has it been submitted as part of requirements for a degree except as fully acknowledged within the text.

I also certify that the thesis has been written by me. Any help that I have received in my research work and the preparation of the thesis itself has been acknowledged. In addition, I certify that all information sources and literature used are indicated in the thesis.

This research is supported by an Australian Government Research Training Program Scholarship.

Signature of Candidate:

Production Note:
Signature removed prior to publication.

Date: 24/01/18

Acknowledgements

This PhD project and resulting thesis were made possible with the help of many people, for which I am sincerely grateful. Firstly I would like to thank my wonderful family, who have always been immensely supportive and inspiring, and helped me believe in myself. Throughout my life my parents have eagerly facilitated my studies, while encouraging me to explore my own interests and abilities. My husband Daniel King has given me emotional and practical support throughout my project, and more recently helped with proofreading chapters of this thesis and offering suggestions. Thanks also to my brother Lawrence Heggie for creating a beautiful diagram of my sintering apparatus for me with his amazing new design skills.

Of course, this whole project would not have been possible without the guidance of my brilliant supervisor, Assoc. Prof. Andrew McDonagh. In my whole undergraduate course I only had a handful of first-year chemistry lectures that were taught by Andrew, but he stood out in my memory as one of the best teachers, and it has been a great privilege to work with him over the last few years and learn what it is to be a good scientist. My co-supervisor, Prof. Michael Cortie, was also an outstanding lecturer from my undergraduate course and the first to introduce me to the fascinating study of gold nanoparticles. Both Andrew and Mike were happy to make time for me in their busy schedules to discuss results, share their expertise, and edit my papers and thesis, for which I am extremely grateful. I could not have wished for better supervisors!

I would also like to thank all those who helped me in the laboratory, namely: Dr Angus Gentle, who helped create the setup I used for the sintering experiments and then helped me fix it whenever something went wrong, and who also helped a great deal with the optical reflectance experiments and data analysis; Mr Geoff McCredie, who also helped me with the sintering experiments; Ms Katie McBean, who so expertly adjusted the SEM for me each time, allowing me to take nice, clear images of my tiny nanoparticles; Miss Juliette Massicot, who worked with me on the gold chloride synthesis study, spending many long hours in the lab to collect each data point; Dr Susan Shimmon and Ms Melissa Birkett, who each synthesised compounds for me to use; Mr Alexander Angeloski, who helped me with the TGA instrument and various other things in the chemistry and materials labs; Dr Annette Dowd, Mr Daniel Totonjian and Dr David Mitchell, who each did TEM imaging for me; Dr David Bishop and Mr Mika Westerhausen, who did the ICP-MS and LA-ICP-MS analysis for me; Dr Ronald Shimmon, who was always happy to answer my questions; the staff at the Australian Synchrotron who allowed us time on the Powder Diffraction beamline to run a few of my experiments; and finally all my fellow PhD students both in the lab and in the office, who helped create such an enjoyable study environment. Thank you!

Table of Contents

List of Figures

List of Tables

List of Abbreviations

AU	arbitrary units
AuNP	gold nanoparticle
BT@AuNPs	1-butanethiol-stabilised AuNPs
$CDCl_3$	deuterated chloroform (chloroform-d)
Citrate@AuNPs	tri-sodium citrate-stabilised AuNPs
CTAB	cetyltrimethylammonium bromide
DCM	dichloromethane
DD	n-dodecane
DDT	1-dodecanethiol
DDT@AuNPs	1-dodecanethiol-stabilised AuNPs
DPDI	*N,N′*-dioleyl-3,4,9,10-perylenedicarboximide
DSC	differential scanning calorimetry
EDS	energy dispersive spectroscopy
fcc	face-centred cubic
FWHM	full width at half maximum
$HAuCl_4$	tetrachloroauric acid
HBC	hexabenzocoronene
HBC-acetylene	penta(*tert*-butyl)-substituted hexa-*peri*-hexabenzocoronene-acetylene
HCl	hydrochloric acid
HD	n-hexadecane
HDT	1-hexadecanethiol
HDT@AuNPs	1-hexadecanethiol-stabilised AuNPs
HNO_3	nitric acid
HPB	hexaphenylbenzene
ICP-MS	inductively coupled plasma mass spectrometry
IR	infrared spectroscopy
$KMnO_4$	potassium permanganate
LA-ICP-MS	laser ablation inductively coupled plasma mass spectrometry
LSPR	localised surface plasmon resonance
molecules/NP	molecules per nanoparticle
MS	mass spectrometry
$NaBH_4$	sodium borohydride

NaClO	sodium hypochlorite
$Na_2S_2O_3$	sodium thiosulfate
NIR	near-infrared
NMR	nuclear magnetic resonance
OA	oleylamine
OA@AuNPs	oleylamine-stabilised AuNPs
OT	1-octanethiol
OT@AuNPs	1-octanethiol-stabilised AuNPs
Pc	phthalocyanine
PyBuOH	1-pyrenebutanol
PyBuSH	1-pyrenebutanethiol
Py@AuNPs	1-pyrenebutanethiol-stabilised AuNPs
4-py^{t}Bu	4-*tert*-butylpyridine
RGB	red green blue
RuPc	ruthenium phthalocyanine
[RuPc(4-py^{t}Bu)$_2$]	[(4-*tert*-butylpyridine)$_2$ruthenium phthalocyanine]
[RuPc(4-py(CH$_2$)$_3$SAc)(4-py^{t}Bu)]	[(*S*-[3-(4-Pyridinyl)propyl]ethanethioate)(4-*tert*-butylpyridine)ruthenium phthalocyanine]
[RuPc(4-pyCH$_2$SAc)$_2$]	[(*S*-[4-Pyridinylmethyl]ethanethioate)$_2$ruthenium phthalocyanine]
SAED	selected area electron diffraction
SEM	scanning electron microscopy
SERS	surface-enhanced Raman spectroscopy
TEM	transmission electron microscopy
TGA	thermogravimetric analysis
THF	tetrahydrofuran
TOAB	tetraoctylammonium bromide
T_{SE}	temperature of the sintering event
UOW	University of Wollongong
UTS	University of Technology Sydney
UV-visible	ultraviolet visible spectroscopy
XRD	X-ray diffraction

Publications Arising From This Work

- **King, S.R.**; Massicot, J.; McDonagh, A.M. A Straightforward Route to Tetrachloroauric Acid from Gold Metal and Molecular Chlorine for Nanoparticle Synthesis.
  Metals **2015**, *5* (3), 1454–1461.
  DOI: 10.3390/met5031454

- **King, S.R.**; Shimmon, S.; Gentle, A.R.; Westerhausen, M.T.; Dowd, A.; McDonagh, A.M. Remarkable Thermal Stability of Gold Nanoparticles Functionalised with Ruthenium Phthalocyanine Complexes.
  Nanotechnology **2016**, *27* (21), 215702.
  DOI: 10.1088/0957-4484/27/21/215702

- **King, S.R.**; Shimmon, S.; Totonjian, D.D.; McDonagh, A.M. Influence of Bound versus Non-Bound Stabilizing Molecules on the Thermal Stability of Gold Nanoparticles.
  The Journal of Physical Chemistry C **2017**, *121* (25), 13944–13951.
  DOI: 10.1021/acs.jpcc.7b04266

- Dehn, M.H.; Arseneau, D.J.; Buck, T.; Cortie, D.L.; Fleming, D.G.; **King, S.R.**; MacFarlane, W.A.; McDonagh, A.M.; McFadden, R.M.L.; Mitchell, D.R.G.; Kiefl, R.F. Evidence for Magnetism in Thiol-Capped Gold Nanoparticles Observed with Muon-Spin-Rotation.
  Applied Physics Letters **2018**, *112* (5), 053105
  DOI: 10.1063/1.5017768

- **King, S.R.**; Gentle, A.R.; Cortie, M.B.; McDonagh, A.M. Development of Optical Properties during Thermal Coarsening of Gold Nanoparticle Composites.
  2018, *Submitted*.

Abstract

Gold nanoparticles possess many interesting and useful properties, which have made them the subject of extensive research. The most notable of these are their optical properties, which can be tuned to suit a variety of applications or monitored as conditions change for sensing applications. The thermal stability of gold nanoparticles is also of particular interest, as this affects their sintering behaviour and therefore their utility in applications such as printed electronics, catalysis and sensing. The bulk of the research on thermal stability has focussed on lowering their stability to facilitate the formation of continuous, electrically conducting films at moderate to low temperatures. However, relatively little is known about increasing their thermal stability for applications where it is necessary for their useful properties to be retained at higher temperatures. This thesis presents an investigation into the thermal stability of gold nanoparticles, with a focus on probing the upper temperature limits of stabilising the particles using organic compounds. Firstly, a new method was developed for synthesising gold chloride as a precursor to gold nanoparticle synthesis, using the known reaction of gold metal with chlorine gas. The resulting gold chloride solutions were of high purity and stability, and were used directly for synthesising the nanoparticles used in this project. For the thermal stability studies, a selection of compounds was tested for their ability to delay the onset of nanoparticle sintering upon heating at a constant rate. Samples were analysed using a range of techniques including electrical resistance measurements, SEM, TGA, and XRD. Comparisons were made between stabilisers that were bound to the particles and those that were mixed with the particles without being chemically attached. A number of compounds of high thermal stability and compatible solubility were identified as particularly effective stabilisers, such as a ruthenium phthalocyanine complex, oleylamine, 1-pyrenebutanethiol and a perylenedicarboximide derivative, with sintering of the particles not occurring until more than 300 °C with these stabilisers, up to an unprecedented 540 °C. Important insights were also gained into the interactions between nanoparticles and unbound stabilisers and the qualities required for an effective stabiliser. Some of the highly stable gold nanoparticles were then monitored for changes in their optical and structural properties with temperature using reflection spectroscopy and SEM, with the results having potential applications in high temperature optical sensing and thermal history indicators.

Chapter 1:

The Thermal and Optical Properties of Gold Nanoparticles

Chapter 1: The Thermal and Optical Properties of Gold Nanoparticles

1.1. Introduction

The term “nanoparticle” may be defined[1] as a particle of any shape with at least one dimension between 1–100 nm, where 1 nm = 10^{-9} m. The maximum limit of 100 nm has been adopted since it corresponds to the approximate scale at which materials often transition from nanoproperties to bulk behaviour. It is these “nanoproperties” that attract research efforts and drive the use of nanoparticles.[2] Colloidal gold nanoparticles (AuNPs) were utilised for their unique optical properties in decoration as early as the 4th century BC in Egypt and China, and later in the 4th century AD by the ancient Romans.[3] It was not until 1857, in a publication by Michael Faraday,[4] that a scientific description of their optical properties emerged. The present-day interest in nanoparticles stems from the broader concept of nanotechnology, itself made popular by the understanding gained through quantum mechanics and the development of technology capable of studying and manipulating matter on the nanoscale. A visionary talk by Richard Feynman in 1959[5] is thought to have contributed to much of the widespread interest in nanotechnology. By the late 1970s, studies adopting the term “nanoparticles” began to be published.[6]

To date, AuNPs have attracted a great deal of interest, contributing to about a quarter of all nanoparticle literature.[a] This is due to their unique optical properties, ease of synthesis, chemical stability, biocompatibility, and their ability to be functionalised with a wide range of molecules, in comparison to other nanoparticles.[3] These properties have enabled the use of AuNPs in numerous applications, such as chemical and biological sensing,[7] optical storage,[8] diagnostic and therapeutic applications in medicine,[9–11] catalysis,[12] printed electronics,[13] and the enhancement of photocurrent generation and Raman spectra.[14]

The application that the research efforts described within this thesis are directed towards would best be described as high-temperature optical sensing. This draws from concepts developed in printed electronics where nanoparticles are deposited onto a substrate and processed into continuous, conductive films via a process known as sintering (discussed in detail in Section 1.2), which also results in a visible colour change. However, this process is often required to occur at moderate to low temperatures (<200 °C), with the majority of the

---

[a] Web of Knowledge database, June 2017.

research focussing on reducing the temperature at which sintering occurs.[13,15–17] Relatively few studies have investigated using AuNPs with a much higher degree of thermal stability, which is important for catalysis and sensing applications where it is necessary to retain the size- and shape-dependent properties of individual nanoparticles at elevated temperatures.

The work presented here is an investigation of the thermal stability of ligand-stabilised AuNPs, focussing on the influence of different stabilising compounds and their ability to induce resistance to thermal sintering. In pursuit of the main objectives, a new and improved method of synthesising gold(III) chloride as a precursor to AuNP synthesis was developed, and is presented within this thesis. Furthermore, *in situ* analysis during thermal treatment of highly stabilised AuNPs showed a prolonged process of nanoparticle coarsening prior to sintering.

The work within this thesis is presented as follows: Chapter 1 provides an overview of the literature relating to the thermal stability of AuNPs and their optical properties, along with a detailed description of the project aims. Chapter 2 provides an in-depth description of the synthesis and analysis methods, where the new synthesis method mentioned above is introduced. The results and discussion of this new synthesis method are then presented in Chapter 3. Chapter 4 presents an investigation of the sintering behaviour of AuNPs stabilised by a variety of compounds. Chapter 5 describes the evolution of some optical and structural properties of stabilised AuNPs at elevated temperatures. Chapter 6 presents the conclusions made from this work and suggests future work that can be done as a result.

1.2. Thermal Stability of Gold Nanoparticles

When subjected to elevated temperatures, AuNPs can coalesce to form continuous, electrically conductive films of gold in a process known as sintering. This property is highly useful for applications such as printing electronic circuits using an “ink” of AuNPs,[17] and much work has been done to reduce the temperature needed to achieve sintering for these purposes. On the other hand, applications in catalysis and sensing devices require the size- and shape-dependent properties of individual nanoparticles to be retained, despite high temperature fabrication and operating conditions.[18,19] In both cases a thorough understanding of AuNP thermal stability is essential, which will allow for improved development of nanomaterials for such applications.

1.2.1. Mechanisms of the Sintering Process

Due to the extreme surface curvature and high surface area to volume ratio of nanoparticles, contact between bare AuNPs results in them fusing together, thereby reducing the surface energy of the system.[15] By definition, ligand-stabilised AuNPs are coated in a layer of molecules, generally chemically bonded to the gold surface via sulfur atoms, which physically separate the nanoparticles from each other and thus prevent their aggregation. Disruption of the stabilising ligands, e.g. through exposure to heat,[20] certain chemicals,[15] intense laser light[21] or a strong electron beam,[22] allows the same process of fusing, or *sintering*, to occur.

There are two main mechanisms by which sintering, of both bare and ligand-stabilised AuNPs, can occur: particle migration and Ostwald ripening. Particle migration involves the movement of entire nanoparticles by surface diffusion, leading to coalescence of the particles as they approach each other.[18] Ostwald ripening, on the other hand, involves the migration of individual atoms from one particle to another, such that larger particles grow at the expense of smaller particles, which become entirely consumed.[18,23] Numerous studies have been conducted to determine which mechanism is active under various conditions, and these have been extensively reviewed elsewhere.[18,24,25] For most ligand-stabilised AuNPs, particle migration appears to be the primary mechanism for sintering.[16] However, in cases where AuNPs are immobilised on a substrate or encapsulated within a mesoporous material (techniques often employed in catalysis applications), Ostwald ripening becomes the dominant mechanism for nanoparticle growth.[26]

When particles sinter by particle migration, two adjacent particles first form a neck at their point of contact, creating a peanut-like shape, before surface area minimisation draws the formerly two particles into a single, larger spheroidal particle.[16] This process can be seen in the transmission electron microscopy (TEM) time-lapse study performed by Chen *et al.* of a monolayer film of ligand-stabilised AuNPs sintering under electron beam irradiation (Figure 1.1).[22] Their study also revealed that sintering would only occur between AuNPs that were initially separated by just 1–2 nm; further sintering was inhibited by the increasing distance between particles as they coalesced, which indicates a limited particle mobility over the substrate.

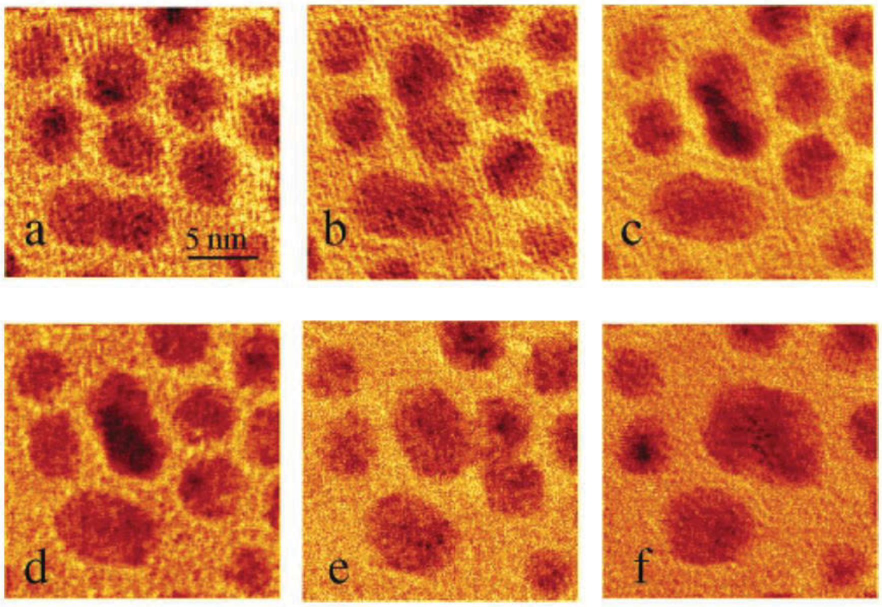

Figure 1.1. TEM images of dodecanethiol-stabilised AuNPs (a) before and after electron exposure with a dose of (b) 7.1, (c) 16.4, (d) 33.7, (e) 73.7, and (f) 149.8 $\mu C/\mu m^2$, showing coalescence of two pairs of nanoparticles. Image reproduced from Chen *et al.*[22]

The process of particle coalescence, which is driven by surface area minimisation, releases energy in the form of heat. This phenomenon was first predicted theoretically by Lehtinen and Zachariah,[27,28] who also demonstrated that the initial neck formation proceeds relatively slowly, but the consequent release of heat then increases the rate of coalescence by up to a few orders of magnitude, releasing additional heat as the surface area decreases further. This release of heat during coalescence was later confirmed experimentally through the observation of an exothermic peak in differential scanning calorimetry (DSC),[15] which has since been used in sintering studies as an indication that sintering has occurred.[20,29,30]

Two possible models have been suggested in the literature regarding the loss of stabilising ligands during the sintering process. The first model proposes that sintering is activated by ligand loss; as the AuNPs are heated, an initial loss of ligands destabilises the particles, allowing them to sinter in an exothermic event that drives off the remaining ligands.[15,16,20] The second model suggests that sintering triggers ligand loss; heating the nanoparticles allows them to begin sintering, and the resulting decrease in surface area serves to both reduce the number of available binding sites for the ligands and releases heat that induces their volatilisation.[29] Martin *et al.* proposed this model based on their observation during thermal analysis of an exothermic peak that preceded the main mass loss event assigned to the loss of alkanethiol ligands.[29] However, this model implies that either the nanoparticles are not fully coated with ligands, thus allowing the ligands to rearrange on the surface to enable sintering, or that the ligands do detach from the particle but do not immediately volatilise and therefore do not register as a mass loss during thermal analysis.[30] It also follows that if sintering causes ligand loss, the temperature at which sintering occurs should be independent of ligand identity, however several studies have shown this is not the case, as discussed in detail in Section 1.2.2. In a recent study, Smith and Hutchison conducted an extensive investigation to ascertain which model for ligand loss is correct, and they concluded that the first model, where ligand loss leads to sintering, is the more accurate of the two.[30] It is important to note that only a relatively small fraction of the ligands must be removed to initiate sintering, with the remaining bulk of the ligands being lost during or soon after the sintering event, as depicted in Figure 1.2, which may explain the conclusions made by Martin *et al*.

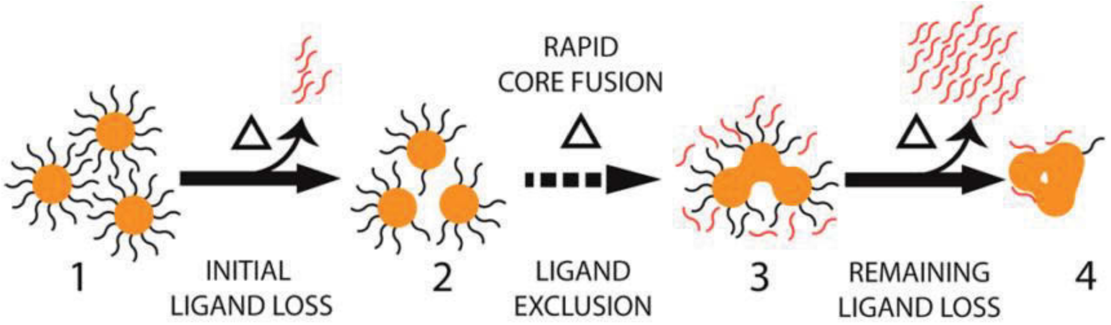

Figure 1.2. Schematic model for the sintering of small, ligand-stabilised AuNPs. Image reproduced from Smith & Hutchison.[30]

1.2.2. Factors Affecting the Thermal Stability of AuNPs

Several factors are known to influence the thermal stability of AuNPs. Firstly, it is important to note that the sintering of AuNPs is a thermally activated *kinetic* process, dependent on the activation energy barrier (ΔG_{act}) introduced by the stabilising ligands (Figure 1.3), and therefore the rate of heating will affect the temperature at which sintering occurs.[15] As a result of this, there is no specific "sintering temperature" for a given nanomaterial in the way there are specific melting points. The slower the heating rate, the lower the temperature of the sintering event (T_{SE}) for a particular sample. For example, Gupta *et al.* noted a difference in T_{SE} between their octanethiol-stabilised AuNPs heated at 3 °C min^{-1} (203.8 °C) and those of Martin *et al.* that were heated at 5 °C min^{-1} (211.6 °C),[20,29] while Cortie *et al.* observed the initial signs of sintering for butanethiol-stabilised AuNPs at ~80 °C for a heating rate of 2.5 °C min^{-1} and at

~100 °C for a rate of 6 °C min^{-1}, during *in situ* XRD experiments.[16] This property suggests that, given enough time, ligand-stabilised AuNPs will eventually sinter at room temperature.

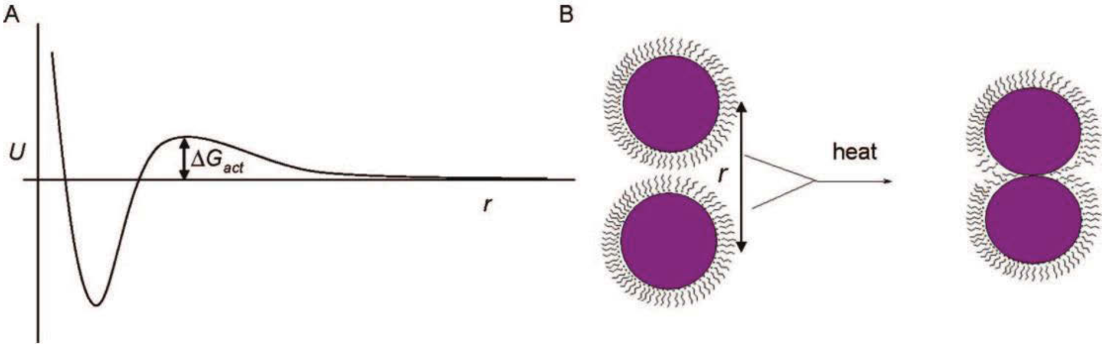

Figure 1.3. (A) Potential energy (U) curve depicting the energy barrier (ΔG_{act}) for ligand-stabilised AuNPs separated by a distance, r. (B) Schematic diagram of the sintering of two AuNPs, showing the required partial disruption of the stabilising ligands. Image reproduced from Coutts *et al.*[15]

Longer alkane chain lengths on stabilising ligands lead to an increased resistance to sintering. AuNPs coated with butanethiol (C_4H_9SH) sinter at temperatures in the range of 120–150 °C,[15,20,31] depending on various conditions explained in detail below, which increases to ~220 °C for AuNPs coated with tetradecanethiol ($C_{14}H_{29}SH$).[29] Many studies suggest this phenomenon is due to the lower volatility and higher boiling point of long chain alkanethiols,[20,29,31] while experiments of heating AuNPs under vacuum, or in an inert atmosphere of nitrogen or argon, show sintering at a significantly higher temperature than in ambient air, along with a greatly reduced dependence on alkanethiol chain length.[15] This is explained to be a result of the longer alkane chains providing increased shielding from oxidation of the gold-sulfur bond.

Another factor, therefore, is the nature of the atmosphere surrounding the AuNPs. Thiol-stabilised AuNPs can be destabilised by oxidation of the sulfur atoms by atmospheric oxygen, which weakens the Au–S interaction, allowing the protective ligands to volatilise and thus the AuNPs to sinter.[16] A long-term shelf life study of films of alkyldithiol-stabilised AuNPs showed that storage under ambient conditions led to coalescence of the AuNPs, while storage under an inert atmosphere did not.[32] Coutts *et al.* exploited this effect to achieve the sintering of AuNPs at room temperature.[15] They exposed a film of AuNPs to a stream of strongly oxidising NO_2 gas (produced by dropping concentrated nitric acid onto copper shavings), while recording the electrical resistance. The film displayed a significant and rapid drop in resistance upon exposure to the gas, and within 50 min had achieved a level of conductivity consistent with sintered particles. However, it has been noted by Wünscher *et al.* that this room temperature sintering technique would only work for nanoparticles of gold, since those of silver or copper would also be oxidised by NO_2, forming less or non-conductive oxide species and thus defeating the purpose.[17] In a similar vein to the nature of the atmosphere, the presence in AuNP samples of halide-containing surfactants, such as the commonly used tetraoctylammonium bromide, has been found to destabilise the Au–S bond and greatly lower the thermal stability when heated under ambient conditions but not when heated under an inert atmosphere.[33]

Particle size has a small effect on the thermal stability of AuNPs, with larger particles sintering at slightly lower temperatures than smaller ones when passivated with the same ligand. This effect has been attributed to the significantly larger volume fraction of passivating ligands on the smaller particles, thus requiring a higher temperature to remove enough of the ligands for sintering to occur.[31] Additionally, the ligand binding strength has been shown by Smith & Hutchison to vary with particle size, seen in thermogravimetric analysis as an earlier onset of ligand mass loss for larger AuNPs, which is likely due to the differing surface curvatures for different nanoparticle sizes.[30]

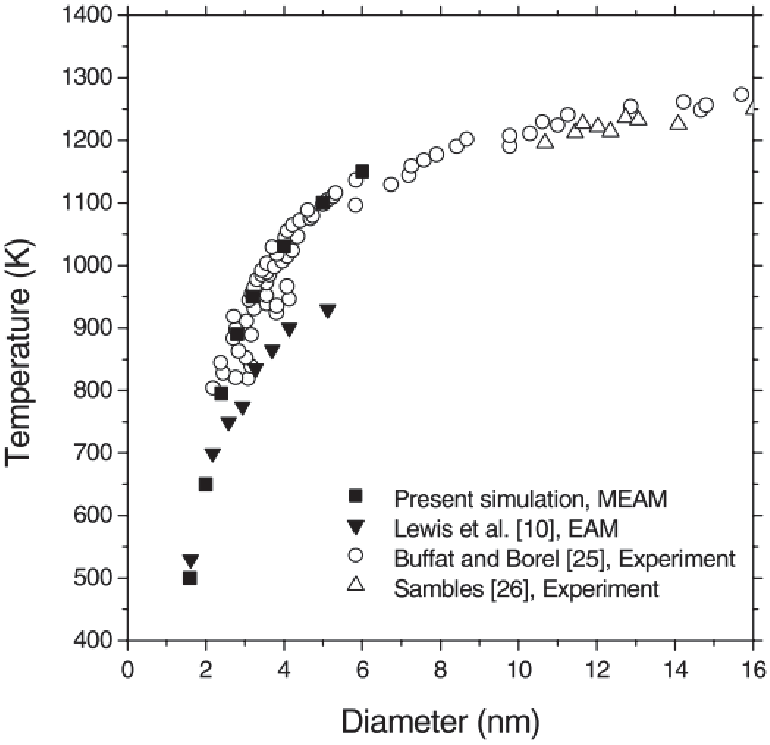

Figure 1.4. Melting point as a function of AuNP diameter, comparing theoretical and experimental results from Shim *et al.* ("Present simulation"),[34] Lewis *et al.*,[35] Buffat and Borel,[36] and Sambles.[37] Image reproduced from Shim *et al.*[34]

Decreasing particle size also considerably reduces the melting temperature of nanoparticles, a phenomenon that affects a wide variety of nanoparticulate materials in addition to gold.[38] Since the liquid/vapour interface energy is usually lower than the solid/vapour interface energy, a decrease in particle size (and corresponding increase in surface to volume ratio) leads to increased free energy at the nanoparticle surface, which lowers the melting point.[34] For AuNPs, the melting point drops rapidly for particles below 5 nm in diameter (Figure 1.4). However, the melting range of AuNPs as small as 1.5 nm, shown experimentally[38] to be ~400 °C (which is higher than the theoretical values shown in Figure 1.4 for that size), is still reasonably high compared to the T_{SE} of most alkanethiol-stabilised AuNPs of comparable size (140–220 °C); as such, the phenomenon of AuNP sintering is not a result of the particles melting.[15]

1.2.3. Strategies for Controlling the Thermal Stability of AuNPs for Various Applications

Depending on the intended application, AuNPs can be required to have either a high or a low thermal stability, and many strategies have been employed by researchers to either prevent or promote nanoparticle sintering. For the example of AuNP ink printing mentioned previously, electrical circuits can be made for use in flexible electronic devices (Figure 1.5).[13,17] A film of AuNPs has a very high electrical resistance, but once sintered the conductivity of the film increases to a level comparable to bulk gold.[39] However, to be utilised in flexible electronics, the AuNPs must be able to sinter at temperatures that are compatible with low-cost plastics, i.e. below 150 °C.[31] Huang *et al.* first reported a plastic-compatible AuNP ink in 2003,[31] composed of 1.5 nm hexanethiol-stabilised AuNPs dispersed in toluene, which could be deposited by inkjet printer onto films of polyester and annealed at 150 °C to obtain films with conductivity 70% that of bulk gold. They found that while butanethiol-stabilised AuNPs could be sintered at an even lower temperature than hexanethiol-stabilised AuNPs, there was an associated decrease in stability. Due to the shorter alkane chain of the stabiliser, there was an inherent reduction in shelf life of the AuNPs in powder form compared to those coated with longer chain alkanethiols. Therefore, balance had to be found between long-term stability and anneal temperature.

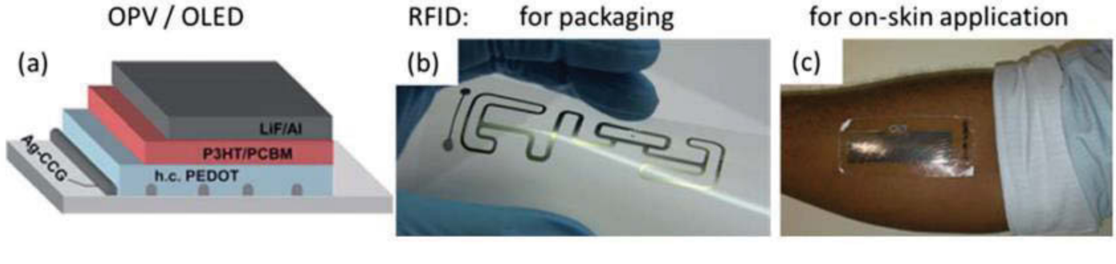

Figure 1.5. Examples of applications for inkjet printed metal nanoparticle sinter inks: (a) current collecting grids (CCG) in organic photovoltaic (OPV) or organic LED (OLED) devices, (b) radio frequency identification (RFID) antenna printed on a sheet of PET and (c) skin-transferrable printed RFID tag. Image reproduced from Wünscher *et al.*[17]

Since the study by Huang *et al.*, many others have been performed to optimise the development of low thermal stability AuNPs for use as plastic-compatible sinter inks.

Alkylamine capping ligands have been tested as a cheaper and less toxic alternative to alkanethiols, and these too have been found to follow the pattern of shorter alkane chains giving lower thermal stability.[13,40] One strategy to avoid the high temperatures, and often long processing times, required to generate conductive patterns from inkjet printed AuNPs is to use alternative methods of sintering instead of heating the entire printed sample. Such alternatives include inducing localised heating through exposure to lasers,[21,41] other high intensity light sources,[42] microwave radiation,[43] or electrical currents,[44] as well as low temperature disruption of the stabilising ligands by exposure to chemicals or plasma.[15,45] These approaches have been reviewed in detail by Wünscher *et al*.[17]

As mentioned previously, two applications that require highly thermally stable AuNPs are sensing and catalysis, where fabrication and operating conditions are often at high temperatures (>300 °C).[19] In the field of sensing technology, nanostructured semiconductor metal oxides (e.g. TiO_2, SnO_2, ZnO, WO_3 and NiO) have been investigated as promising sensing materials for various gases and vapours,[19,46] which is of great interest in industrial processes such as power generation, aviation/aerospace and numerous manufacturing procedures.[47] The incorporation of AuNPs into these metal oxide nanomaterials has been found to greatly enhance their sensing capabilities, by reducing the electrical resistance in conductometric sensors and by providing environmentally sensitive optical properties in optical sensors, although the precise mechanisms involved are still an active area of investigation.[19,47] The fabrication of these AuNP/metal oxide nanocomposites requires the metal oxide to be annealed at temperatures around 500 °C to attain optimal sensor responses, and many of their intended applications are in harsh environments (e.g. extreme temperatures, highly oxidising, reducing or corrosive conditions). The accompanying AuNPs must therefore be protected from these conditions to avoid any changes to their size or shape, which would impair the functioning of the sensor. Studies on conductometric sensors made by surface modification methods (i.e. where the AuNPs decorate the surface of the metal oxide) showed rapid particle coalescence that increased the particle sizes from ~3–5 nm to ~20–60 nm when annealed at ~300 °C, but for those made by sol-gel techniques, which result in AuNPs embedded within the metal oxide, the AuNPs remained at ~3–5 nm in diameter even after annealing at ~600 °C.[19] Multiple studies by Ohodnicki *et al.* on optical sensors for harsh environments have also demonstrated remarkably high thermal stability for AuNPs that are embedded in metal oxides.[47–51] This increase in thermal stability is attributed to the solid medium that is the metal oxide physically separating and trapping the AuNPs, which prevents their migration and consequent coalescence.[52]

In contrast to bulk gold, which is well known to be inert, nanoscale gold can be highly catalytically active,[12] with small AuNPs (<5 nm) being ~1000 times more active than platinum in the oxidation of CO into CO_2 when under basic, though not acidic, conditions (Figure 1.6).[53]

This gold-catalysed oxidation of CO has even been found to proceed at room temperature or lower, another great advantage over platinum catalysts, which must operate at much higher temperatures.[53] However, many other industrially important catalytic reactions that can be catalysed by AuNPs must still be performed at elevated temperatures.[54] The development of AuNP catalysts for such reactions has unfortunately been hampered by the susceptibility of AuNPs to sintering under such high-temperature operating conditions, thereby losing their catalytic properties as they grow larger than 5 nm in diameter.[55–57] As such, there is great ongoing scientific interest in creating AuNP catalyst systems with high thermal stability.[54]

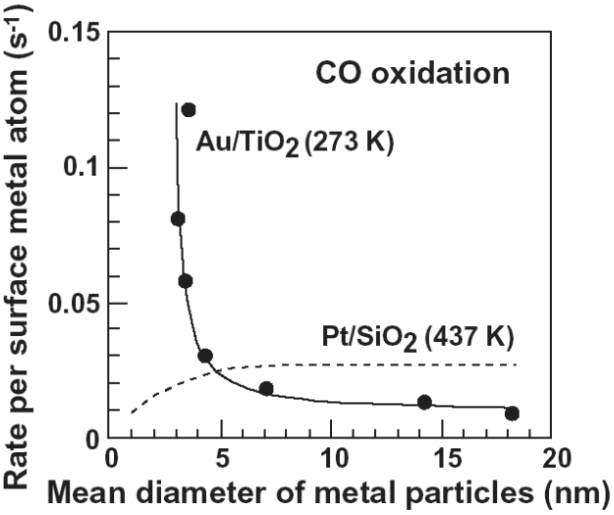

Figure 1.6. Turnover frequency of CO oxidation catalysed by Au/TiO_2 and Pt/SiO_2 as a function of metal particle size. Image reproduced from Haruta.[53]

Nanoparticles for gas-phase catalysis are typically supported on metal oxide substrates, rather than suspended in a colloid, and are not passivated by ligand molecules, so as to allow access to the active sites on the nanoparticle surface during catalysis. Additionally, supported nanoparticles are generally easier to recover than unsupported particles upon completion of the reaction.[58] For AuNPs, the most commonly used metal oxide support is TiO_2,[57] as it has a synergistic effect with gold for oxidation and photocatalytic reactions,[55] though other supports such as SiO_2 and Al_2O_3 have also been used.[54,59] These metal oxide supports provide some stabilisation for the AuNPs under mild conditions, but at elevated temperatures the particles readily sinter. A number of strategies to combat this poor thermal stability have been proposed in the literature to date. One approach is to create mesoporous supports with precisely controlled pore sizes to entrap small AuNPs.[26,52] These supports can be modified with a second metal oxide material to create bimodal mesoporous structures, which can provide crystalline or amorphous nanodomains that have been found to strongly anchor the AuNPs to the support.[54,60,61] A similar method has been proposed by Wang *et al.*,[59] where thin, porous, star-shaped sheets of Al_2O_3 were found to stabilise AuNPs against sintering up to temperatures of 700 °C. Their analysis showed this stability to be a result of strong interfacial interactions between the gold and the rough-textured surface of the thin (~15 nm) Al_2O_3 sheets, which effectively immobilised the AuNPs and prevented their aggregation. Another approach to prevent sintering under reaction conditions is to encapsulate AuNPs within a porous metal oxide shell.[55,62,63] Lee *et al.*[55] have developed a procedure to synthesise "yolk@shell" nanostructures, composed of AuNPs each surrounded by a large (~200 nm diameter) hollow shell of porous TiO_2 (Figure 1.7). They found that AuNPs within the shells displayed no changes in size after being heated to ~500 °C, unlike the control sample of AuNPs dispersed on TiO_2-P25 powder, which showed significant sintering of the AuNPs upon heating. In catalysis reactions, the porosity of the TiO_2 shells allowed the reactant gases to diffuse into the hollow shell to access the AuNPs, giving CO oxidation reaction rates comparable to the more traditional Au/TiO_2-P25 catalyst, despite the reduced packing efficiency from having one small AuNP per large TiO_2 shell. For many of these strategies, research is ongoing to determine the long-term thermal stability of the AuNP catalysts under reaction conditions.

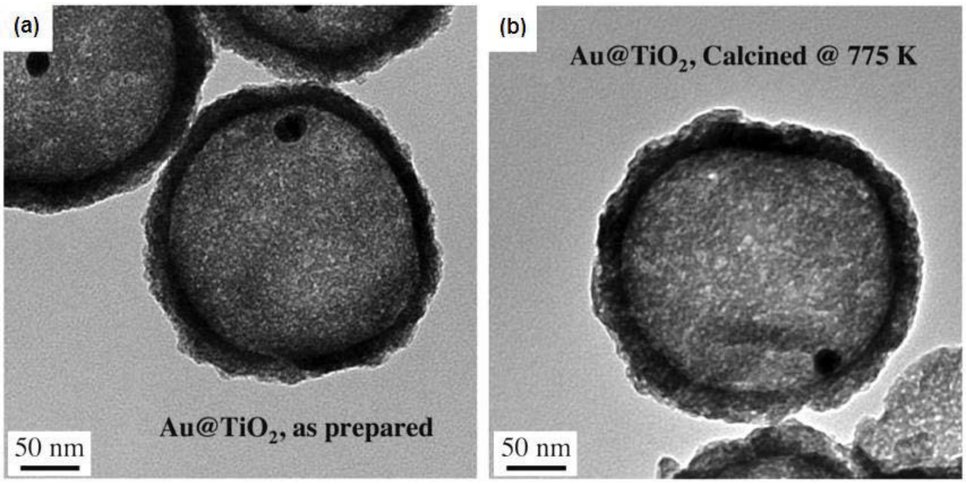

Figure 1.7. TEM images of Au@TiO_2 "yolk@shell" nanostructures (a) before heating and (b) after heating to 775 K (502 °C). Image reproduced from Lee *et al.*[55]

1.3. Optical Properties of Gold Nanoparticles

The useful and tunable optical properties of AuNPs are one of the key features that have attracted the interest of researchers towards their use in nanotechnology. The strongly size- and shape-dependent colour displayed by colloidal gold is due to the localised surface plasmon resonance (LSPR) absorption of the AuNPs. The LSPR arises from the free conduction electrons in a nanoparticle collectively resonating in response to an applied electromagnetic field,[64] as shown schematically in Figure 1.8. For many metals, such as Cd, In, Sn, Hg and Pb, the plasmon frequency lies in the UV region of the spectrum, so the nanoparticles do not show strong colour effects. However with noble metals such as Au, Ag and Cu, the LSPR frequency falls in the visible region, with AuNPs strongly absorbing incident green light of wavelength ~520 nm, imparting the colloid with a deep red colour.[65]

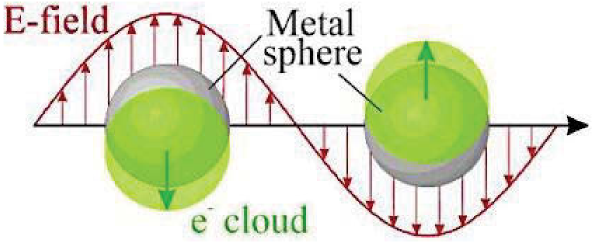

Figure 1.8. Schematic diagram showing the electron cloud displacement of a metal nanoparticle in an electric field, leading to localised surface plasmon resonance. Image reproduced from Kelly *et al*.[64]

The nature of the LSPR of metal nanoparticles can be described using the Mie solution to Maxwell's equations, which is a mathematical description of the attenuance spectra of spherical particles with a size comparable to the wavelength of the incident light. A comprehensive explanation of Mie theory regarding the LSPR of AuNPs has been given by Ghosh and Pal,[65] however the main characteristics described by the theory are: the position of the resonance band at ~520 nm for particles around 20 nm in diameter; a greater importance placed on the higher order resonance modes with increasing particles size, which are responsible for a red-shift in the LSPR absorption (Figure 1.9), and hence, the blue-shift observed in the colloidal colour with increasing particle size; and a sharp decrease in the resonance magnitude for particles below 3 nm due to the onset of quantum effects, as the LSPR damping is inversely proportional to the nanoparticle radius.[66] Different nanoparticle shapes display different plasmon resonance behaviours; for example nanorods have two plasmon peaks, one due to transverse resonance, which is at the same frequency as a sphere of the same diameter, and one due to longitudinal resonance.[8] Changes to the dielectric constant of the material surrounding metal nanoparticles, in the form of solvents, solid matrices or capping molecules, can also influence the LSPR frequency, since it affects the ability of the nanoparticle surface to accommodate electron charge density.[67]

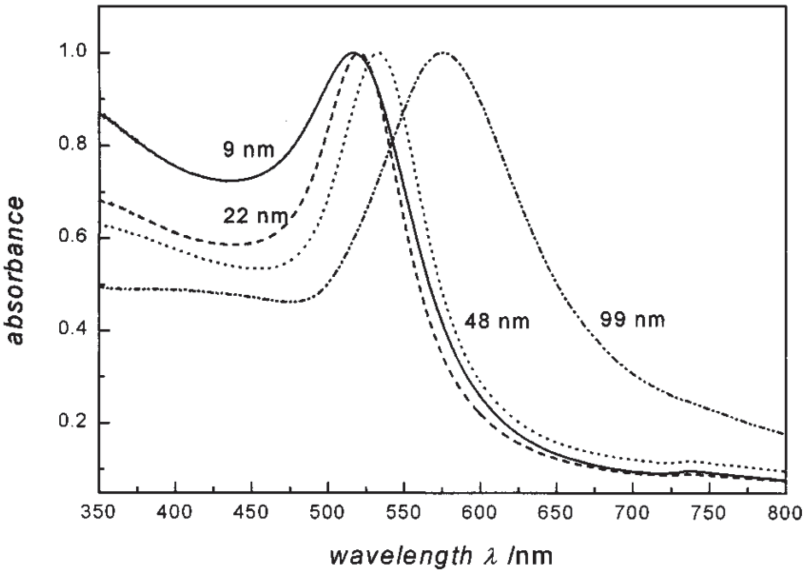

Figure 1.9. UV-visible absorption spectra for AuNPs in water, showing the red-shift in LSPR wavelength with increasing particle size. Image reproduced from Link & El-Sayed.[68]

The LSPR induced by an applied electromagnetic field generates a strong electric field confined to the AuNP surface, known as the plasmonic near-field.[69] At resonance, this near-field is greatly enhanced compared to the applied field, which can be used to significantly increase the electronic transitions of optically absorbing and emitting compounds that are adsorbed to the nanoparticle surface. This process is the basis of surface-enhanced Raman spectroscopy (SERS), a technique used to amplify the Raman signal of molecules that would otherwise have extremely small Raman scattering cross-sections.[70]

When two plasmonic nanoparticles are brought into close proximity with each other, where the separation is much smaller than the wavelength of light, the plasmonic near-field of each nanoparticle can coherently interfere with that of the other nanoparticle, known as plasmon coupling.[66,71] This coupling leads to an electromagnetic "hot spot" between the two particles, with its strength being highly dependent on the distance between them.[66,72] The longitudinal plasmon resonance for the coupled nanoparticles also becomes red-shifted compared to the individual nanoparticles, with a larger red-shift for closer particles, while the orthogonal plasmon resonance experiences a slight blue-shift.[73] The phenomenon of plasmon coupling can be further enhanced by assembling plasmonic particles into 3D core-satellite nanostructures (a 'core' particle surrounded by multiple ionically or covalently linked 'satellite' particles).[74–76] In core-satellite nanostructures, the red-shift seen for the two particle system is increased, as each of the numerous satellites becomes coupled to the core particle. The plasmon resonance also no longer depends on the polarisation of the incident light, since the structure is essentially isotropic.[77]

The LSPR of AuNPs is dependent on temperature, with a slight red-shift and significant broadening and decrease in intensity of the plasmon band when heated to very high temperatures (Figure 1.10).[78] This phenomenon is entirely reversible and repeatable,[78,79] and is more pronounced for larger nanoparticles.[80] Doremus first investigated the temperature dependence of plasmon resonance in 1964 for temperatures ranging from –196 to 540 °C.[80] The AuNPs were grown in a glass medium, since aqueous colloids can only be monitored over a relatively small temperature range and deposited films of AuNPs are prone to sintering. Later studies used SiO_2 instead of glass to stabilise the AuNPs, which enabled the use of even higher temperatures.[78] The red-shift observed with increasing temperature is a result of the thermal lattice expansion of the particles causing a decrease in the electron density, which directly determines the frequency of the LSPR.[68,78] Meanwhile, the broadening and decreased intensity of the plasmon peak at higher temperatures has been attributed to electron-phonon scattering, the rate of which increases linearly with increasing temperature.[78] The temperature dependence of AuNP plasmon resonance has potential applications in the optical sensing of temperature and gas composition simultaneously in the harsh conditions of certain industrial processes.[49,51] Since LSPR is highly dependent on particle size, any polydispersity within a sample of AuNPs would be problematic for optical temperature sensing. To overcome this issue, Maurya and Toutam have identified, through theoretical modelling, a temperature-dependent but size-independent parameter, the LSPR frequency to damping ratio, which can be used instead of the LSPR frequency for temperature sensing.[72]

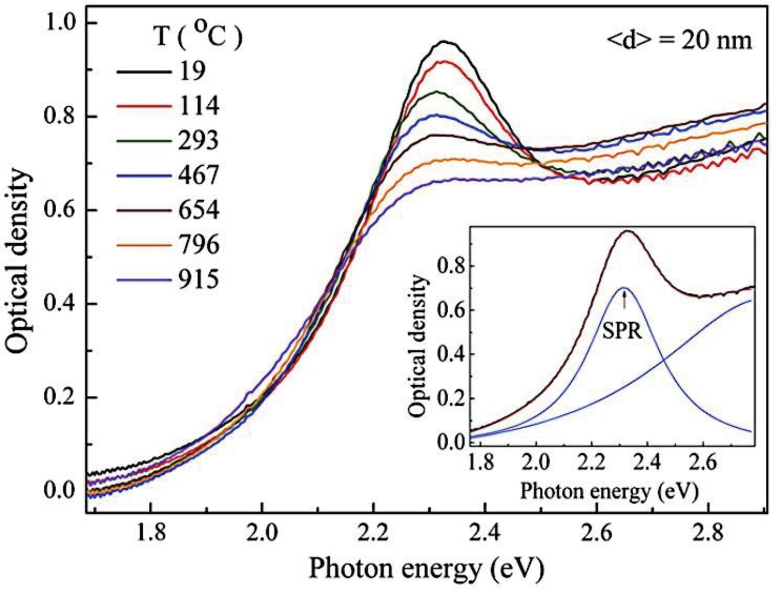

Figure 1.10. Absorption spectra collected during the heating of AuNPs with an average diameter of 20 nm embedded in a SiO_2 matrix. Inset shows the deconvolution of the total spectrum at 19 °C into the LSPR and interband transition components. Image reproduced from Yeshchenko *et al.*[78]

1.4. Project Aims

Aim 1. To explore the upper temperature limits for stabilising AuNPs using organic compounds.

It is apparent from the literature that a large proportion of the research investigating the thermal stability of ligand stabilised AuNPs has been performed with the aim of reducing the thermal stability to facilitate sintering (within the bounds of room temperature stability). A much smaller amount of research into *increasing* the thermal stability of AuNPs is evident and it does not address high stability using organic stabilisers.

Aim 2. To examine the effect of anchoring the ligand.

It is not yet known whether the stabilising compounds must be anchored directly to the particles in order to protect them from sintering, or if thermal stability can be conferred on the particles by the simple inclusion of thermally stable nonthiolated organic compounds.

Aim 3. To probe the changes in optical and microstructural properties of thermally stable films of AuNPs before and during the sintering process.

Since the ligand-stabilised AuNPs in existing thermal studies sinter at relatively low temperatures (~200 °C or lower), it is unknown how films of AuNPs of greater thermal stability would behave optically at higher temperatures, and whether the changes in microstructure during AuNP sintering differ between high and low temperature conditions. Knowledge of such optical and structural behaviour may be useful for optical sensing technologies in high temperature environments.

Aim 4. To develop a superior gold(III) chloride synthesis method.

The field of AuNP research is quite large and continues to grow, creating with it the need for high purity gold(III) chloride as a precursor for nanoparticle synthesis. There are issues with both commercial gold(III) chloride and existing synthesis methods, such as instability and difficulties in producing samples of sufficiently high purity (explained in detail in Chapter 3).

Chapter 2:
Experimental Methods

Chapter 2: Experimental Methods

This chapter provides details of the methods used for the synthesis of various chemical compounds and gold nanoparticles and heat treatment techniques. Some of these details have been published.[81–83] Also included in this chapter is a description of the characterisation techniques that were used to analyse the synthesised products and other materials.

2.1. Synthesis

The following chemicals were purchased commercially and used as received.

From Sigma-Aldrich: 1-butanethiol, chloroform-d, 1-dodecanethiol, hexaphenylbenzene, hydrobromic acid (69%), imidazole, oleylamine, 1-octadecene, 1-octanethiol, 3,4,9,10-perylenetetracarboxylic dianhydride, potassium thioacetate, 1-pyrenebutanol, sodium borohydride, 4-*tert*-butylpyridine, tetrahydrofuran, tetraoctylammonium bromide.

From Chem-Supply: chloroform, dichloromethane, hexane, potassium carbonate, sodium chloride, toluene.

From other suppliers: sodium hypochlorite, sodium thiosulfate pentahydrate, tri-sodium citrate (Ajax Finechem); 1-hexadecanethiol, *n*-octane (Fluka); hydrochloric acid (36%), nitric acid (70%) (RCI Labscan); gold pellets (99.99%, ~200–400 mg each) (AGS Metals); potassium permanganate (BDH); *n*-hexadecane (Hopkin & Williams); *n*-dodecane (Merck); anhydrous magnesium sulfate (Scharlau).

Penta(*tert*-butyl)-substituted hexa-*peri*-hexabenzocoronene-acetylene (HBC-acetylene) was a gift from Dr Nigel Lucas of the University of Otago (New Zealand).[84]

2.1.1. Synthesis of Tetrachloroauric Acid

Chlorine Gas Method[b]

A reaction apparatus was assembled as shown in Figure 2.1.

---

[b] The method described here has been published (see King, Massicot and McDonagh, *Metals*, 2015, *5*, 1454-1461).

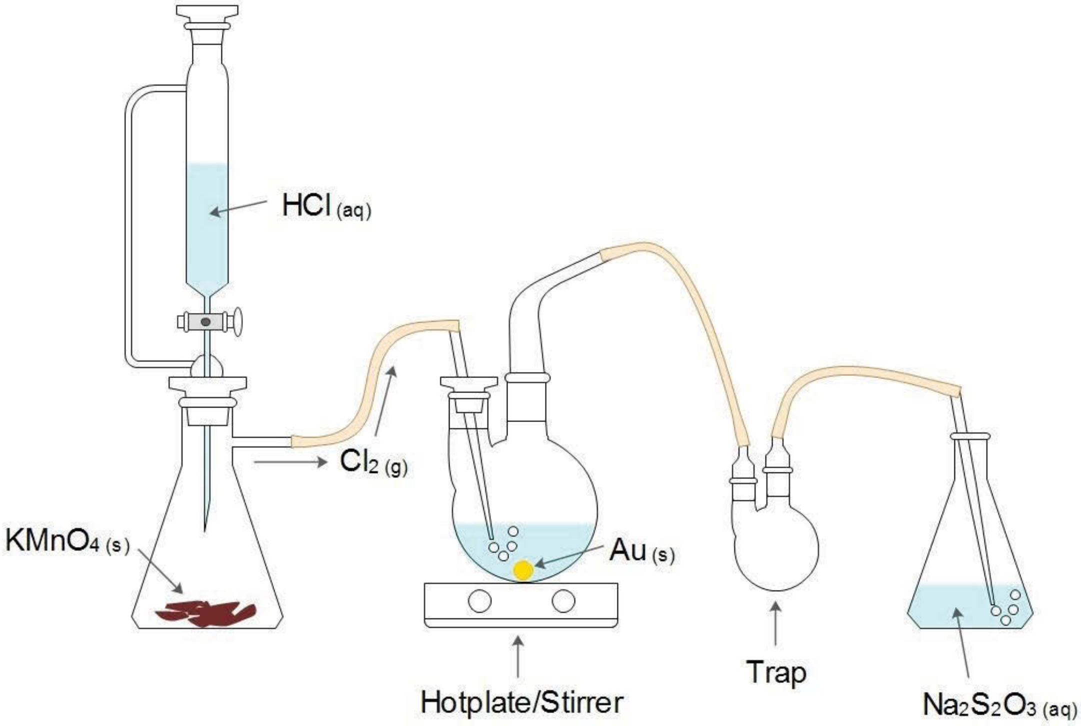

Figure 2.1. Apparatus for the synthesis of aqueous tetrachloroauric acid.

Concentrated HCl (14 mL, 36%, 0.16 mol) was placed in a pressure-equalising dropping funnel, and slowly added dropwise to a side-arm flask containing potassium permanganate ($KMnO_4$, 3.0 g, 19 mmol). The resulting chlorine gas (see Equation 2.1) was passed into a two-neck round-bottom flask (cleaned by *aqua regia*) containing a Teflon-coated magnetic stirrer bar, Milli-Q water (100 mL) and one or more pellets of gold (~250–360 mg each), depending on the desired final concentration. Undissolved/unreacted chlorine gas was bubbled through a solution of sodium thiosulfate ($Na_2S_2O_3$, 1.1 g, 7.0 mmol) in water (50 mL). The reaction mixture was stirred at the selected temperature (25–70 °C) until all of the gold dissolved. If using more than one pellet of gold and/or higher reaction temperatures, additional HCl and $KMnO_4$ can be added to the dropping funnel and conical flask, respectively, as required. The resulting solution of tetrachloroauric acid ($HAuCl_4$) can be used without further treatment. UV-visible (λ_{max}, nm [ε, 10^4 L mol^{-1} cm^{-1}]): 226 [3.5], 313 [0.54].

$$2KMnO_{4\,(s)} + 16HCl_{(aq)} \rightarrow 5Cl_{2\,(g)} + 2KCl_{(aq)} + 2MnCl_{2\,(aq)} + 8H_2O_{(l)} \qquad (2.1)$$

The rate at which gold dissolved was measured by weighing the gold pellet at regular intervals. The pellet was removed from the reaction vessel using a clean glass spoon, rinsed with acetone and allowed to completely dry, and then weighed before being returned to the reaction mixture. For experiments using flattened gold pellets, the pellets were placed between layers of cotton fabric or sheets of polycarbonate to avoid metallic contamination, and were mechanically pressed to a thickness of ~1 mm.

The concentration of chlorine in solution was measured using the iodometric titration method,[85] which follows the reactions shown in Equations 2.2 and 2.3. A solution of $Na_2S_2O_3.5H_2O$ (378.7 mg, 1.53 mmol) in Milli-Q water (100 mL) was prepared and then used to fill a 10 mL burette. A 1% w/w aqueous solution of Vitex (modified starch) was used as the indicator. A 10 mL aliquot of freshly diluted aqueous $HAuCl_4$ (1.025 mM) was transferred to a small conical flask containing a few grains of KI (~50 mg); upon swirling, the pale yellow solution turned light brown from I_2 formation. A few drops of the indicator were added, which turned the solution blue. The $I_2/HAuCl_4$ solution was then titrated against the $Na_2S_2O_3$ solution until a pale pink colour was reached, indicating the endpoint. Any further addition of $Na_2S_2O_3$ turned the solution colourless. The titration was performed 3 times.

$$Cl_2 + 2KI \rightarrow I_2 + 2KCl \tag{2.2}$$

$$I_2 + 2Na_2S_2O_3 \rightarrow 2NaI + Na_2S_4O_6 \tag{2.3}$$

Hypochlorite Method

The following procedure for synthesising $HAuCl_4$ follows a modified literature method for the industrial extraction of gold from ore.[86]

A pellet of gold (275 mg, 1.40 mmol) was placed in a 500 mL conical flask (cleaned by *aqua regia*) containing aqueous sodium hypochlorite (NaClO, 85 mL, 12.5%), sodium chloride (NaCl, 28.0 g, 0.48 mol) and a Teflon-coated stirrer bar. Aqueous HCl (~4 mL, 36%) was added dropwise with stirring, until a pH of ~4 was attained. The flask was then stoppered and the reaction (see Equation 2.4) was left to stir for 3 days until all the gold had dissolved, turning the solution a bright, clear yellow colour.

$$2Au_{(s)} + 3NaClO_{(aq)} + 3NaCl_{(aq)} + 6HCl_{(aq)} \rightarrow 2AuCl_{3\,(aq)} + 6NaCl_{(aq)} + 3H_2O_{(l)} \tag{2.4}$$

The gold chloride solution was decanted into a 500 mL separating funnel, and the excess undissolved NaCl in the conical flask was washed with diethyl ether (20 mL) to remove all of the gold chloride. The ether was transferred to the separating funnel, along with additional diethyl ether (130 mL) to extract the gold chloride. A further three extractions, each using 150 mL of diethyl ether, were required to remove most of the gold chloride from the aqueous phase. The solution in ether was then returned to the separating funnel and the gold chloride was extracted with 3 × 100 mL portions of Milli-Q water. HCl (10 mL, 1.0 M, 10 mmol) was added to stabilise the $HAuCl_4$ solution, however within 2 weeks metallic gold was observed to have precipitated from the solution. As such, $HAuCl_4$ prepared by this method was not used for any subsequent nanoparticle synthesis.

2.1.2. Synthesis of AuNPs

Oleylamine-Stabilised Gold Nanoparticles (~5 nm diameter)

Oleylamine-stabilised AuNPs (OA@AuNPs) were synthesised using a modified two-phase Brust-Schiffrin method, as used by Choi *et al*.[87] Aqueous $HAuCl_4$ (6.25 mL of a 0.08 M solution, 0.5 mmol) was added to a solution of tetraoctylammonium bromide (TOAB, 0.683 g, 1.3 mmol) in toluene (50 mL) and rapidly stirred for 2 h. Gold(III) ions phase transferred from the aqueous to the organic phase, changing the colour of the aqueous phase from yellow to colourless and that of the organic phase from colourless to dark orange. The aqueous layer was then separated and discarded. Oleylamine (1.65 mL, 5.0 mmol) was added to the Au/TOAB precursor solution with stirring. A freshly prepared solution of sodium borohydride ($NaBH_4$, 0.283 g, 7.5 mmol) in ice-cold Milli-Q water (15 mL) was quickly added dropwise with rapid stirring. The mixture became deep red in colour, indicating the formation of nanoparticles, and was stirred for a further 3 h. The resulting colloid was kept in a tightly stoppered flask at room temperature as a long-life stock solution, and small portions were extracted and washed as required.

The OA@AuNPs were washed by adding the colloid dropwise with vigorous swirling to at least 3 times the volume of methanol. The particles were allowed to precipitate over a period of several hours and were then collected by centrifugation, rinsed with additional methanol and air-dried, leaving a black powder that can be stored for up to a few weeks and resuspended in a suitable organic solvent (e.g. toluene, chlorobenzene, chloroform, dichloromethane (DCM), tetrahydrofuran (THF)).

1-Butanethiol-Stabilised Gold Nanoparticles (~3 nm diameter)

1-Butanethiol-stabilised AuNPs (BT@AuNPs) were synthesised using a modified two-phase Brust-Schiffrin method, similar to that of Wu *et al*.[39] Aqueous $HAuCl_4$ (50.0 mL of a 0.08 M solution, 4 mmol) was added to a solution of TOAB (8.75 g, 16 mmol) in toluene (300 mL) with rapid stirring. Gold(III) ions phase transferred from the aqueous to the organic phase, leaving the aqueous phase colourless and turning the organic phase dark orange. After 5 min, a solution of 1-butanethiol (0.36 g, 4 mmol) in toluene (50 mL) was added to the flask. The resulting solution was stirred vigorously for 10 min at room temperature and then cooled in an ice-water bath. A freshly prepared solution of $NaBH_4$ (1.51 g, 40 mmol) in ice-cold Milli-Q water (100 mL) was added over 30 s with rapid stirring. The solution turned dark brown/black in colour upon the formation of nanoparticles. The vigorous stirring was continued for 3 h, after which the organic phase was separated and washed three times with water, then dried with anhydrous $MgSO_4$ and filtered. The colloid was reduced in volume to ~50 mL using a rotary evaporator at 50 °C, and then slowly added to 200 mL of methanol with vigorous swirling, causing the particles to precipitate. The precipitate was collected by centrifugation, washed with additional methanol and air-dried, resulting in a stable black powder than can be stored for a few years and resuspended in a suitable organic solvent.

1-Octanethiol-Stabilised Gold Nanoparticles (~5 nm diameter)

1-Octanethiol-stabilised AuNPs (OT@AuNPs) were synthesised using a modified two-phase Brust-Schiffrin method as described by Yang *et al.*,[88] with minor variations. Aqueous $HAuCl_4$ (5.1 mL of a 12.4 mM solution, 0.063 mmol) was added to a solution of TOAB (86.4 mg, 0.16 mmol) in toluene (25 mL) with rapid stirring. After 30 min the aqueous phase was separated and discarded. A freshly prepared solution of $NaBH_4$ (10 mg, 0.26 mmol) in ice-cold Milli-Q water (0.25 mL) was added to the dark orange organic phase with rapid stirring. The colour gradually changed over 1 min to brownish orange, then brown, then suddenly to a dark burgundy red. After stirring for 2.5 h, 1-octanethiol (0.607 g, 4.1 mmol) was added dropwise, and the reaction was stirred for a further 2 h. The organic phase containing the OT@AuNPs was separated and the solvent was removed using a rotary evaporator at 50 °C. Ethanol (20 mL) was added to the flask, which was briefly sonicated to ensure complete dissolution of excess octanethiol and other impurities, and the precipitated particles were collected by centrifugation, washed three times with ethanol and then air-dried, leaving a stable black powder that can be resuspended in a suitable organic solvent.

Citrate-Stabilised Gold Nanoparticles (~12 nm diameter)

Aqueous citrate-stabilised AuNPs (citrate@AuNPs) were synthesised using the Turkevich method.[89] All glassware was thoroughly cleaned with *aqua regia*, then rinsed and steeped in Milli-Q water prior to use. Aqueous $HAuCl_4$ (6.85 mL of a 14.6 mM solution, 0.1 mmol) was added to a 100 mL volumetric flask and diluted with Milli-Q water to make a 1.00 mM solution. The contents of the volumetric flask were poured into a 250 mL conical flask containing a magnetic stirrer bar, and heated to 90 °C. While stirring vigorously, a freshly prepared solution of tri-sodium citrate (114 mg, 10.0 mL, 38.8 mM) in Milli-Q water was quickly added to the conical flask. The solution was heated for a further 15 min, during which time its colour changed from yellow to colourless, then to a dark bluish colour and finally to deep red with the formation of the nanoparticles. The colloid was allowed to cool to room temperature before stoppering the flask.

2.1.3. Synthesis of Stabilising Compounds

N,N′-Dioleyl-3,4,9,10-perylenedicarboximide

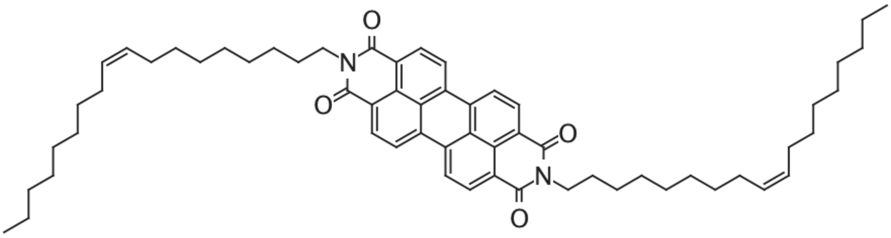

Figure 2.2. Structure of *N,N′*-dioleyl-3,4,9,10-perylenedicarboximide.

N,N′-Dioleyl-3,4,9,10-perylenedicarboximide (DPDI) was prepared using the method of Choi *et al.*[90] 3,4,9,10-Perylenetetracarboxylic dianhydride (500 mg, 1.27 mmol) and imidazole (6.0 g) were added to a single-neck round-bottom flask equipped with a stirrer bar, and heated at 160 °C. Once all the imidazole had melted, oleylamine (0.90 mL, 2.7 mmol) was added to the mixture. The reaction was stirred for 4 h at 160 °C, and then allowed to cool a little before adding ethanol (20 mL) to dissolve the remaining imidazole. Aqueous HCl (15 mL, 2 M) was added to the mixture, which was then allowed to stand for 1 h. The precipitate was collected by vacuum filtration and washed with distilled water. The crude product was purified using a silica plug (DCM/acetone 20:1) and the solvent was removed using a rotary evaporator, giving a dark red waxy product (81 mg, 7.1%).

^{1}H NMR (δ, 500 MHz, $CDCl_3$): 0.87 (broad *t*, 6H), 1.25–2.01 (*m*, 56H), 4.19 (*t*, $J = 15$, 4H), 5.34 (*m*, 4H), 8.56–8.66 (*m*, $J = 10$, 8H). **UV–Vis** (λ_{max}, nm): 459, 490, 526.

1-Pyrenebutanethiol

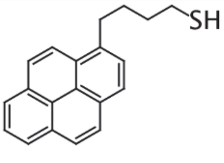

Figure 2.3. Structure of 1-pyrenebutanethiol.

1-Pyrenebutanethiol[91] was prepared with the help of Dr Susan Shimmon, using the method of Han and Balakumar.[92] First, 1-pyrenebutanol was converted to 1-pyrenebutylbromide as follows. 1-Pyrenebutanol (0.490 mg, 1.79 mmol) was added to a two-neck round bottom flask equipped with a stirrer bar and condenser. Aqueous hydrobromic acid (20 mL, 69%) was then added dropwise and the reaction mixture was heated at reflux for 4 h. After cooling to room temperature, the product was extracted with DCM (3 × 30 mL), and the combined organic layers were washed with water and dried over anhydrous $MgSO_4$. The solvent was then removed using a rotary evaporator to give a pale brown oil (541 mg, 90%).

The 1-pyrenebutylbromide was then converted to 1-pyrenebutanethiol as follows. To a two-neck round bottom flask was added 1-pyrenebutylbromide (330 mg, 0.986 mmol) and anhydrous THF (5 mL), followed by potassium thioacetate (162 mg, 1.17 mmol) and potassium carbonate (248 mg, 2.17 mmol). The reaction mixture was stirred at room temperature for 45 min under a nitrogen atmosphere. Methanol (5 mL) was then added and the reaction was stirred for a further 45 min, after which the pH was adjusted with dilute aqueous hydrochloric acid to pH ~6. The solvent was removed using a rotary evaporator, and the residue was dissolved in chloroform (20 mL) and washed with water (3 × 10 mL). The organic layer was dried over anhydrous $MgSO_4$ and the solvent was removed using a rotary evaporator. The crude product was purified by silica gel dry column vacuum chromatography with stepwise gradient elution using chloroform/hexane (30:70 to 80:20), which after removal of the solvent gave 243 mg (85%) of a pale yellow powder.

^{1}H NMR (δ, 500 MHz, $CDCl_3$): 8.26–8.23 (*d*, *J* = 9.0, 1H), 8.14–8.12 (*dd*, *J* = 7.5, 3.5, 2H), 8.09–8.07 (*d*, *J* = 9.0, 2H), 8.06–7.79 (*m*, 3H), 7.66–7.82 (*d*, *J* = 7.5, 1H), 3.49 (*d*, *J* = 7.5, 1H), 3.32 (*t*, *J* = 7.5, 2H), 2.56 (*t*, *J* = 7.5, 2H), 1.99–1.92 (*m*, 2H), 1.74–1.72 (*m*, 2H).

[RuPc(4-pyR)$_2$] (R = ^{t}Bu, CH$_2$SAc)

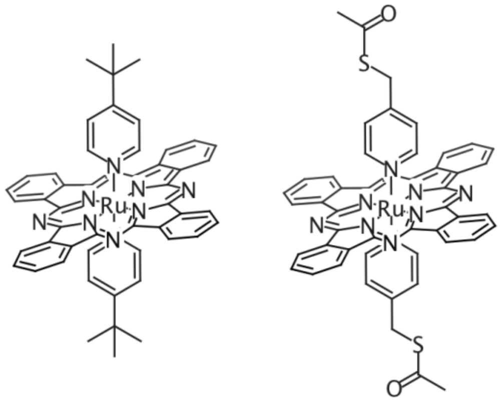

Figure 2.4. Structures of [RuPc(4-py^{t}Bu)$_2$] and [RuPc(4-pyCH$_2$SAc)$_2$].

The ruthenium phthalocyanine (RuPc) complexes [RuPc(4-pyR)$_2$] (R = ^{t}Bu, CH$_2$SAc) were prepared from [RuPc(PhCN)$_2$][93] using the method of Rawling *et al*[94] by Ms Melissa Birkett (R = ^{t}Bu) and Dr Susan Shimmon (R = CH$_2$SAc) of UTS. ^{1}H NMR and UV-visible spectra were consistent with previously reported data.[94,95]

[RuPc(4-py(CH$_2$)$_3$SAc)(4-py^{t}Bu)]

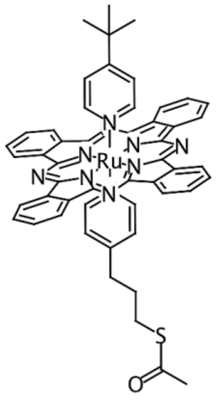

Figure 2.5. Structure of [RuPc(4-py(CH$_2$)$_3$SAc)(4-py^{t}Bu)].

The new RuPc complex [RuPc(4-py(CH$_2$)$_3$SAc)(4-py^{t}Bu)] along with its component ligand *S*-[3-(pyridin-4-yl)propyl]ethanethioate were synthesised by Dr Susan Shimmon, who also collected the characterisation data provided below.[82] To a two-neck round bottom flask containing deoxygenated DCM (40 mL) was added *S*-[3-(pyridin-4-yl)propyl]ethanethioate (76 mg, 0.39 mmol), 4-*tert*-butylpyridine (60 µL, 0.39 mmol) and [RuPc(PhCN)$_2$] (165 mg, 0.270 mmol). The resultant solution was heated at reflux for 3 h under a nitrogen atmosphere, after which the solvent was removed using a rotary evaporator. The crude product was purified by silica column chromatography eluting with DCM/hexane (3:1). The second band to elute was collected and the solvent removed to give a blue powder (40 mg, 26%).

MS (*m/z*) 945.2382 ([M + H]$^+$, 100%). **^{1}H NMR** (δ, 500 MHz, CDCl$_3$): 0.31 (*s*, 9H, *t*-Bu), 0.88 (*p*, J = 6.5 Hz, 2H, CH$_2$-CH$_2$-CH$_2$), 1.47 (*t*, J = 7.0 Hz, 4H, CH$_2$-Ph); 2.05 (*s*, 3H, CH$_3$CO), 2.17 (*t*, J = 6.5 Hz, 2H, CH$_2$S), 2.37 (*d*, J_{HH} = 6.0 Hz, 4H, py), 5.04 (*d*, J_{HH} = 6.5 Hz, 2H, py), 5.18 (*d*, J_{HH} = 7.2 Hz, 2H, py), 7.88 (*m*, 8H, Pc), 9.13 (*m*, 8H, Pc). **IR** (ν, cm^{-1}) 3434, 3052, 2923, 1689, 1652, 1615, 1578, 1489, 1473, 1414, 1366, 1324, 1288, 1168, 1125, 1065, 778, 754, 736, 667, 625, 573. **UV-visible** (λ_{max}, nm [ε, L mol^{-1} cm^{-1}]): 316 [112000], 377 [31900], 570 [29900], 625 [80600].

2.1.4. Functionalisation of AuNPs[c]

Alkanethiol-Stabilised AuNPs

To functionalise OA@AuNPs with alkanethiols, a gold:thiol mole ratio of 1:4 was used. The percentage of gold (w/w) in OA@AuNPs was measured by TGA. The alkanethiol was dissolved

---

[c] The methods described here have been published (see King *et al.*, *Nanotechnology*, 2016, *27*, 215702; and King *et al.*, *J. Phys. Chem. C*, 2017, *121*, 13944–13951).

in toluene (20 mL) and transferred to a single-neck round bottom flask equipped with a magnetic stirrer bar. The OA@AuNPs were suspended in toluene (10 mL) and then added to the alkanethiol solution and stirred for 30 min. The flask was left to stand overnight to allow any precipitate to settle. The colloid was collected by pipette, transferred to a clean round bottom flask and the solvent was removed using a rotary evaporator at 45 °C. To remove the displaced oleylamine and excess thiol, ethanol (30 mL) was added to the flask, which was briefly sonicated and the black precipitate was collected by centrifugation. The particles were washed twice more with ethanol and air-dried.

Alkanethiols used: 1-butanethiol, 1-octanethiol, 1-dodecanethiol and 1-hexadecanethiol.

1-Pyrenebutanethiol-Functionalised AuNPs

1-Pyrenebutanethiol (PyBuSH, 8.0 mg) was dissolved in toluene (20 mL) with sonication and the solution transferred to a two-neck round bottom flask equipped with a stirrer bar. OA@AuNPs (8.0 mg) were suspended in toluene (10 mL) and then added to the solution of PyBuSH. The solution was stirred under a nitrogen atmosphere for 1 h, and was then transferred to a single-neck round bottom flask and the volume of solvent was reduced on a rotary evaporator at 45 °C until ~3 mL remained. The concentrated solution was added dropwise to methanol (30 mL), which was centrifuged to collect the precipitate. The particles were washed twice more with methanol and air-dried.

Phthalocyanine-Functionalised AuNPs

[RuPc(4-py$(CH_2)_3$SAc)(4-py^{t}Bu)] (5.2 mg) was dissolved in toluene (20 mL) in a two-neck round bottom flask with a stirrer bar. OA@AuNPs (10.4 mg) were suspended in toluene (10 mL) and then added to the flask. The mixture was stirred overnight at room temperature under a nitrogen atmosphere. The functionalised AuNPs were precipitated by the addition of ethanol (90 mL) and collected by centrifugation. The particles were washed three times with ethanol to remove the displaced oleylamine and excess RuPc complex, and then air-dried to give a dark blue/black powder.

To a solution of [RuPc(4-pyCH_2SAc$)_2$] (9.2 mg) in toluene (30 mL) was added a suspension of OA@AuNPs (7.5 mg) in toluene (10 mL). The mixture was stirred overnight at room temperature under a nitrogen atmosphere, and the functionalised particles were washed with ethanol and air-dried, as described above.

2.1.5. Preparation of Mixtures of AuNPs and Stabilising Compounds[d]

Mixtures of AuNPs and stabilising compounds without anchoring groups were prepared at different ratios of molecules to nanoparticles. Using the density of bulk gold, a 3 nm spherical AuNP has a calculated mass of 2.73×10^{-19} g. The butanethiol in BT@AuNPs is 11% by weight, as measured by TGA, so on average a BT@AuNP has a mass of 3.07×10^{-19} g. The mass of a molecule was calculated by dividing its molar mass by Avogadro's number. For a desired ratio of x molecules per nanoparticle, Equation 2.5 was used to calculate the masses required:

$$g_{\text{stabiliser}}/g_{\text{BT@AuNPs}} = \frac{x}{m_{\text{BT@AuNP}}} \times m_{\text{stabilising molecule}} \qquad (2.5)$$

where $g_{\text{stabiliser}}/g_{\text{BT@AuNPs}}$ is the ratio of the masses of stabiliser and BT@AuNPs, $m_{\text{BT@AuNP}}$ is the average mass in grams of one BT@AuNP (in this case 3.07×10^{-19} g) and $m_{\text{stabilising molecule}}$ is the mass in grams of one molecule of stabiliser.

The amount of BT@AuNPs in each mixture was 0.5 mg, which is an amount found to provide adequate electrical conductivity upon sintering in the absence of additional stabilising compounds. Stock solutions of materials were prepared and measured volumes were placed into separate vials according to the required ratios. Each mixture was then sonicated to thoroughly combine the molecules and AuNPs, and the solvent was evaporated under a gentle stream of compressed air or nitrogen, leaving a dry powder that could be re-dissolved in an appropriate solvent.

Unanchored stabilising compounds used: dodecane, hexadecane, oleylamine, 1-octadecene, 1-pyrenebutanol, [RuPc(4-py^{t}Bu)$_2$], DPDI, hexaphenylbenzene (HPB), HBC-acetylene.

2.2. The Sintering of Gold Nanoparticles[e]

2.2.1. Preparation of Sample Substrates

To prepare sample substrates for electrical resistance measurements, a silicon wafer was first placed in a furnace and heated to 1200 °C for 20 min to grow a ~300–400 nm thick electrically insulating oxide layer on the surface. The wafer was then cut into rectangles approximately 1.5 cm × 2 cm in size. Gold was deposited onto the substrates, as illustrated in Figure 2.6. The

---

[d] The method described here has been published (see King *et al.*, *J. Phys. Chem. C*, 2017, *121*, 13944–13951).

[e] The method described here has been published (see King *et al.*, *Nanotechnology*, 2016, *27*, 215702).

edges of the substrates were masked with tape to avoid short-circuits across the exposed sides of the semi-conductive silicon. A length of copper wire 0.4 mm in diameter was placed over each substrate, and held in place by small (15 mm wide) fold-back clips. A pellet of gold was then thermally evaporated onto the surface to a thickness of ~100 nm (evaporator base pressure = 2×10^{-6} Torr). The masking was removed to reveal two gold electrodes separated by a gap of 0.4 mm (confirmed by measurement with SEM).

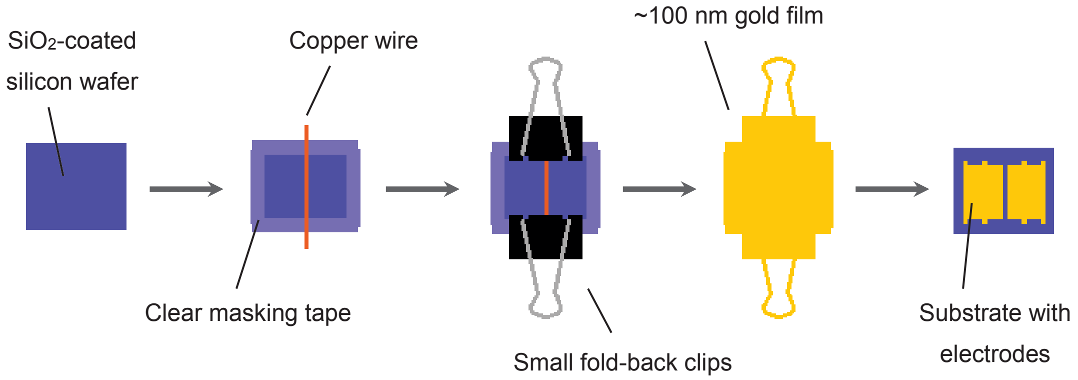

Figure 2.6. Schematic diagram of the substrate fabrication process.

2.2.2. Deposition of Samples onto Substrates

Fine-tipped glass pipettes were prepared by holding the thin section of long Pasteur pipettes over a Bunsen burner, rotating it to ensure even heating, and then quickly pulling on the ends of the pipette once the glass had softened enough to do so, creating a long capillary. After allowing the glass to cool, the start of the capillary near the main body of the pipette was gently snapped off, leaving a pipette with a very fine tip, which allows for greater control and smaller spot sizes when drop casting the samples than with a regular Pasteur pipette. Plastic micropipette tips were not considered suitable, due to the use of organic solvents. Dry samples were dispersed in a minimum amount of chloroform (concentration ~0.3 g/L) and drop cast using the fine-tipped pipette onto the substrates, such that the resulting film spanned the two gold electrodes and a continuous layer of AuNPs remained upon evaporation of the solvent.

2.2.3. Electrical Resistance Measurements

The setup used to measure electrical resistance as a function of temperature is shown in Figure 2.7. Samples were placed on an aluminium heating block with an attached thermocouple. Steel probes (held in place by a clamp magnetically anchored to a steel plate) provided ohmic electrical contact to each of the gold electrodes and resistance was measured using a Yokogawa 7562 digital multimeter (maximum reading of 200 MΩ). A LabVIEW programme (written by Dr Angus Gentle, UTS) was used to control the heating rate and record the temperature and electrical resistance. The temperature was increased at a rate of 10 °C min^{-1} from room temperature to 450 °C (or higher in the case of samples containing DPDI or PyBuSH, up to ~560 °C, which was the heating limit of the aluminium block in open air). The sintering event is characterised by a significant drop in resistance, which is usually accompanied by a colour change to lustrous gold.

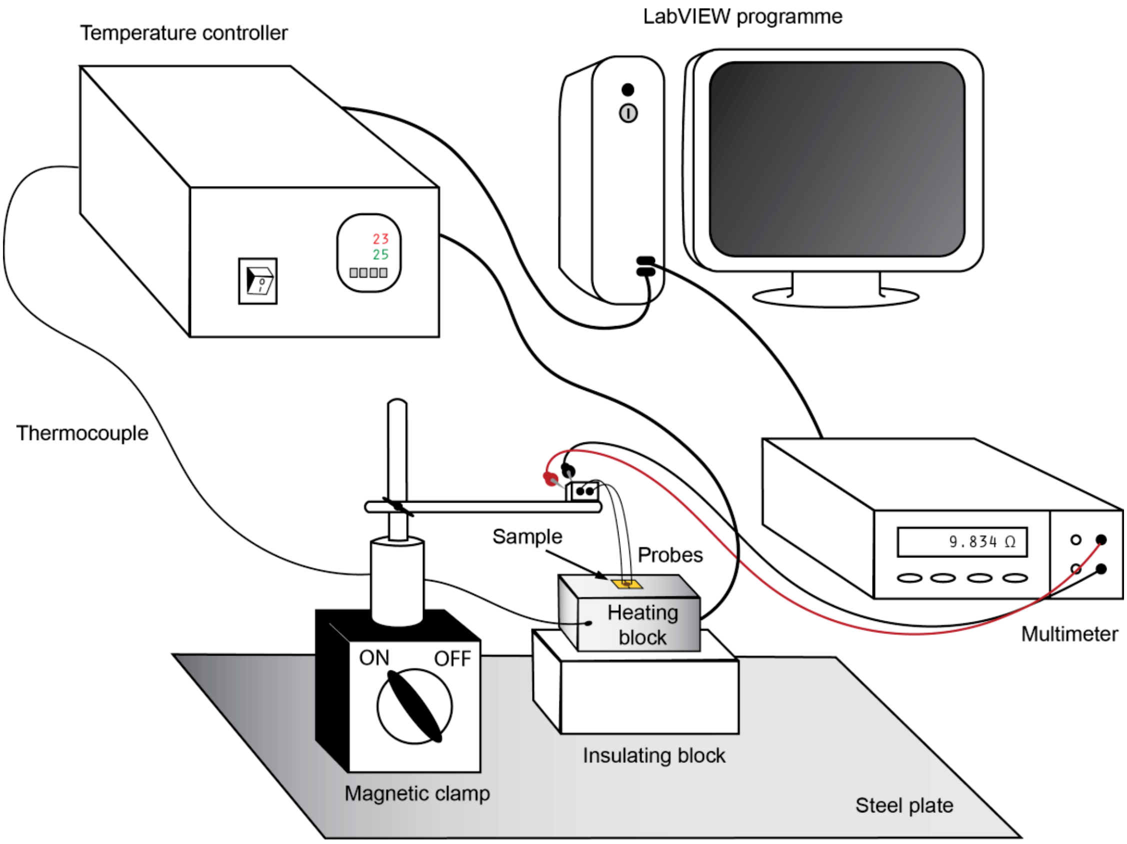

Figure 2.7. Diagram of the setup used for electrical resistance measurements.

2.3. Optical Reflectance Measurements

In situ reflectance spectroscopy was performed with the assistance of Dr Angus Gentle (UTS) whilst the temperature of the samples was increased. Suspensions of AuNPs in chloroform were drop cast onto clear white glass slides. The apparatus (Figure 2.8) consisted of an Ocean Optics LS-1 tungsten halogen light source, and a USB-2000 Si photodiode array spectrophotometer with 5 mm diameter collimating and 25 mm diameter collection lenses (Ocean Optics 84-UV-25), leading to a 10 mm diameter sampling area. The light source and detector are each positioned at 15° either side of normal incidence to the sample. A sputtered aluminium reference mirror was used for calibration of the spectrometer setup. The samples were placed on a computer controlled heating stage within the spectrometer, allowing reflectance spectra to be collected as the samples were heated. A LabVIEW programme (Dr Angus Gentle, UTS) synchronised the sample heating and the capturing of the reflectance data.

The reflectance spectra were measured at 6 s intervals throughout the heating process, and the samples were heated at a rate of 10 °C min^{-1}, up to a maximum of 450 °C. The data were then exported in a text format for post processing and analysis via Microsoft Excel.

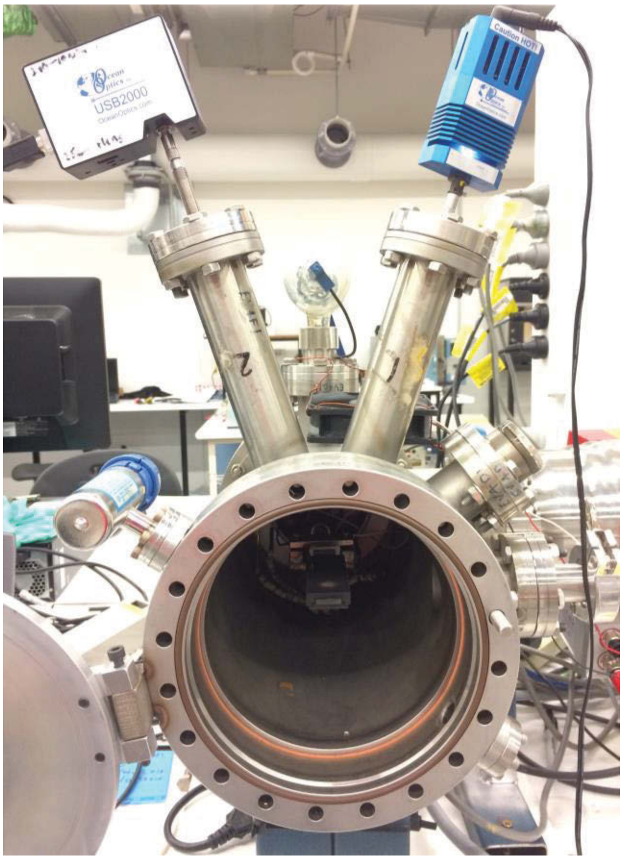

Figure 2.8. Photograph of the equipment used for optical reflectance measurements.

2.4. Characterisation Techniques

2.4.1. Thermal Analysis

Thermogravimetric analysis and differential scanning calorimetry (TGA/DSC) were conducted simultaneously, since the test conditions for both techniques are often the same and have been combined into a single instrument. Both techniques probe the behaviour of a sample as a function of temperature, and their simultaneous outputs can give an understanding of the physical processes occurring in the sample.

TGA/DSC was performed using a TA Instruments SDT Q600. Solid samples weighing ~5 mg and liquid samples weighing ~10 mg were loaded into alumina crucibles and heated from room temperature to 700 °C or higher (up to 1400 °C) at 10 °C min^{-1} either in air at a flow rate of 30 mL min^{-1}, or in nitrogen at a flow rate of 120 mL min^{-1}.

Thermogravimetric Analysis

This technique measures the change in mass of a sample either as a function of temperature or time. Subtle changes in mass can indicate a loss of volatile species or oxidation/combustion of the sample specimen, however a nitrogen atmosphere is typically used to avoid oxidation. The results obtained from TGA were compared to data from sintering experiments, which were performed in air; as such, the majority of TGA/DSC measurements were conducted in an atmosphere of air.

Differential Scanning Calorimetry

DSC provides information about the amount of heat required for a change of state, or the amount of heat produced during decomposition/combustion. In a typical setup, an empty reference crucible is heated at a linear rate along with the crucible containing the sample to be analysed, such that the two are always at the same temperature as each other. The amount of heat flow required to maintain these identical temperatures is then monitored. When a phase transition or decomposition event occurs, the sample will require more (endothermic) or less (exothermic) heat to raise its temperature relative to the reference crucible. The information gained by this technique can be used both qualitatively and quantitatively.

2.4.2. Ultraviolet-Visible Spectroscopy

UV-visible spectroscopy is a routine laboratory characterisation technique used to determine the concentration of a compound in solution or, if the concentration is known, to calculate the compound's molar attenuation coefficient, ε, at particular wavelengths. It can also be used to glean information about the average size and shape of colloidal nanoparticles, since these properties influence the shape and position of the LSPR peak in a UV-visible spectrum.

To collect a spectrum, photons with wavelengths typically between 200–800 nm are shone through a sample solution, and the intensity of the transmitted light for each wavelength is recorded and compared to the intensity of the incident light. The amount of absorption of the initial intensity of light is proportional to the concentration of the solute, the relation for which (as derived from the Beer-Lambert law) can be expressed as $A = \varepsilon cl$, where A is a unitless measure of absorbance (often reported in "arbitrary units" or AU), ε is the molar attenuation coefficient in L mol^{-1} cm^{-1}, c is the solution concentration in mol L^{-1}, and l is the path length in cm.

Within this study, UV-visible spectra were recorded using an Agilent Technologies Cary 60 UV-visible spectrophotometer, with quartz cuvettes with a path length of 1 cm. Solvent baselines were recorded before each set of measurements, with 0.1 M aqueous HCl as the solvent for $HAuCl_4$ samples and toluene as the solvent for all other samples.

2.4.3. Scanning Electron Microscopy

Scanning electron microscopy (SEM) is typically used to examine the morphology, chemical distribution and composition of a sample at the micro- and nano-scales. Since electrons have shorter wavelengths than photons of visible light, as determined by quantum mechanics, it is possible to "see" (with the aid of a computer) features of a sample that are smaller than allowed by the diffraction limit of optical microscopes (~200–250 nm).

Within the microscope, an electron beam typically 0.2–40 keV in energy is emitted from an electron gun fitted with a tungsten filament cathode, and is scanned over a sample. A series of magnetic lenses are used to focus the electron beam, and the sample stage can be moved to explore x,y space. The sample must either be inherently electrically conductive or be coated with a conductive material to combat charging effects, and the chamber must be under vacuum (for conventional SEM). The interaction of the electron beam and the sample produces multiple emissions, namely backscattered electrons, X-rays and secondary electrons. Various detectors receive these signals, which are subsequently interpreted by a computer. The position of the beam on the sample and the number of counts of each signal are represented as a brightness intensity, which is used to produce a 2D image of the sample.

Chemical information can be acquired through energy dispersive spectroscopy (EDS), where the electrons from higher energy orbitals drop to lower energies (as a result of inelastic scattering from the electron beam), producing an X-ray that has a characteristic energy and wavelength to the particular element and electron shell. These X-rays can be quantified and mapped to the locations they were collected, for elemental analysis. There are a number of inaccuracies that can arise for quantitative analysis, which can be corrected for using various techniques.[96]

Within this thesis, SEM was performed using a Zeiss Supra 55VP SEM operating at 20 keV, with samples drop cast onto silicon wafer. EDS was performed using a Zeiss Evo LS15 SEM equipped with a Bruker SDD XFlash 5030 detector, using an accelerating voltage of 8 keV, and semi-quantitative analysis results were obtained using the ZAF correction technique.[97] All images were taken using an in-lens secondary electron detector.

2.4.4. Transmission Electron Microscopy

Transmission electron microscopy is a powerful analysis technique for determining the structure and morphology of very thin samples (<100 nm thick), with image resolutions of <1 nm attainable. In contrast to SEM, which detects the electrons scattered or emitted from the sample, TEM detects the electrons that pass through the sample, which get deflected according to the atomic structure/mass of the specimen. Typically, a beam of electrons 100−400 keV in energy is transmitted first through a condenser aperture, then through the sample, the objective and intermediate apertures, and finally through multiple lenses, all under vacuum. The resulting signal is then detected using a fluorescent screen, or in more modern machines, a CCD detector. Depending on how the lenses are adjusted, either the back focal or the image plane can be coincident with the detector, resulting in a diffraction pattern or a bright field image, respectively. Imaging the back focal plane will record a selected area electron diffraction (SAED) using the same theory as XRD (see Section 2.4.6). For ordered structures, the diffraction pattern is a series of bright points, in reciprocal space, that represent columns of atoms. Structures that do not have any long-range order display as diffuse rings in the diffraction pattern instead of discrete points. When the image plane is incident on the detector, the TEM is in 'bright field' mode and TEM micrographs of sample morphologies can be recorded. Bright and dark regions correspond to the number of electrons transmitted through the specimen, i.e. thick, denser areas or regions of atoms with high atomic numbers will produce darker areas due to a larger proportion of scattered electrons.

In this project, TEM was performed using three instruments across three universities, due to varying requirements: at the University of Sydney, the University of Wollongong (UOW) and the University of Technology Sydney (UTS). TEM at the University of Sydney was performed by Dr Annette Dowd (of UTS) using a JEOL 2200FS TEM operating at 200 keV. TEM at UOW was performed by Dr David Mitchell using a JEOL ARM200F aberration (probe) corrected instrument operating at 200 keV. TEM at UTS was performed by Mr Daniel Totonjian using an FEI Tecnai T20 TWIN microscope (LaB_6) operating at 200 keV and fitted with a Gatan 894 2k × 2k camera. All samples were drop cast from toluene onto lacy carbon grids.

2.4.5. Inductively Coupled Plasma Mass Spectrometry

ICP-MS is a mass spectrometry technique that can measure the concentration of elemental species within a sample, with resolutions as low as 1 part in 10^{15} (parts per quadrillion, ppq) possible, though for the present study the instrument was calibrated for concentrations between 1 and 1000 ppb. This measurement is performed by converting the sample into an ionised state and identifying the species based on their atomic mass and charge. To ionise the sample, a gas (typically argon) is inductively heated by an electromagnetic coil supplied with a radio-frequency current. An electric spark is used to introduce free electrons to the gas, which oscillate in the magnetic field and collide with the atoms of the gas. Some of these collisions result in the atoms becoming ionised, thus generating a plasma that can reach temperatures as high as 10 000 K. The sample, generally in solution, can then be introduced to the plasma by various methods, where it too undergoes ionisation. The plasma is then analysed using a mass spectrometer, which separates the ions based on their mass-to-charge ratio and sends a signal to a detector that is proportional to the concentration of the ions.

Laser ablation ICP-MS (LA-ICP-MS) can be used to map the location and abundance of particular elements in a sample deposited on a (usually glass) substrate. A laser beam is scanned over the sample to remove, or ablate, the sample material, which is then carried to the ICP-MS portion of the instrument for analysis as above.

For the results within this thesis, Dr David Bishop performed ICP-MS using an Agilent Technologies 7500cx series ICP-MS with sample introduction via a micromist concentric nebuliser (Glass expansion) and a Scott type double pass spray chamber cooled to 2 °C. The sample solution and the spray chamber waste were carried using a peristaltic pump. ICP-MS extraction lens conditions were selected to maximise the sensitivity of a 1% HNO_3:HCl solution containing 1 ng/mL of Li, Co, Y, Ce and Tl. Stock solutions were purchased from Choice Analytical and baseline HNO_3 from Seastar Chemicals Inc. Calibration standards were prepared in 1% HNO_3.

LA-ICP-MS was performed by Mr Mika Westerhausen using a New Wave UP213 laser ablation unit (Kenelec Technologies) connected to an Agilent Technologies 7500ce ICP-MS. The UP213 unit used an Nd:YAG emission source emitting a nanosecond laser pulse in the fifth harmonic at 213 nm. A standard New Wave ablation cell was used. The carrier gas was argon, flowing through the chamber at 1.15 L min^{-1}. The 7500ce ICP-MS was fitted with a ‘cs’ lens system for enhanced sensitivity, and forward RF power was reduced to 1250 W for dry plasma conditions. For LA-ICP-MS experiments, a laser beam of 30 μm diameter was used, with a scan speed of 30 μm s^{-1} and a frequency of 20 Hz. The distance between each scan line was 30 μm to ensure total ablation of the sample sections. An area of 1 mm × 300 μm was ablated on AuNP samples and blank control substrates before and after sintering. Operational parameters for the LA-ICP-MS system are summarised in Table 2.1. Each line of ablation generated a single data file for all the elements selected. Interactive Spectral Imaging Data Analysis Software (ISIDAS), an in-house developed suite written in the programming language Python 2.7, was used to combine all data files into a single image. The images were exported from ISIDAS in the format Visualization Toolkit (.vtk) to ParaView 4.3.1 (Kitware Inc.). Relative intensity was then determined using ParaView to normalise all elemental maps to the ^{197}Au map.

Table 2.1. Summary of the operational parameters used for LA-ICP-MS.

Agilent 7500ce ICP-MS		New Wave UP213 Laser Ablation	
RF power	1250 W	Wavelength	213 nm
Cooling gas flow rate	15 L min^{-1}	Repetition frequency	20 Hz
Carrier gas flow rate	1.15 L min^{-1}	Laser energy density	0.3 J cm^{-2}
Sample depth	4.0 mm	Spot size	30 µm
QP Bias	–16 V	Scan rate	30 µm s^{-1}
OctP Bias	–18 V	Line spacing	30 µm
Scan mode	Peak hopping	Carrier gas	Ar
Dwell time	0.25 s per m/z		
Measured m/z	33, 34, 101, 197		
Extracts 1,2	5.7, –102.5 V		

2.4.6. X-ray Diffraction

X-ray diffraction is a technique that is typically used to determine the crystal structure of a sample. This is achieved by detecting X-rays diffracted off the periodic electron density in a crystal. Scattered X-rays that satisfy the Bragg condition ($n\lambda = 2d \sin\theta$, where n is an integer, λ is the wavelength of the incident X-rays, d is the interplanar spacing and θ is the reflected angle) constructively interfere and are detected as a diffraction pattern. In an ordered structure, the interatomic distances that occur the most frequently in the sample appear as higher intensities with the same 2θ value (corresponding to a d-spacing through the above relation). The obtained XRD pattern can then be compared to patterns for known structures to determine what structures are present in the sample. For powdered or microcrystalline samples, powder diffraction can be performed, which uses the assumption that the sample is isotropic and therefore that a sufficient number of each crystal plane within the structure will be properly orientated to diffract the X-rays and contribute to the detected signal.

Most of the XRD data reported here was collected at the Australian Synchrotron using the Powder Diffraction beamline, with the help of Prof. Michael Cortie (UTS). Since the samples were to be heated to high temperatures (~800 °C) while collecting diffraction patterns at 60 s intervals, the extreme intensity and high quality of synchrotron radiation were required to generate well-resolved patterns within such a short time for each scan. Powder XRD was also performed using a diffractometer at UTS for a sample of $[\mathrm{RuPc}(4\text{-py}^t\mathrm{Bu})_2]$ at room temperature, since an XRD pattern for this substance was missing from the databases of XRD patterns for known compounds.

Powder XRD at the Australian Synchrotron was performed for angles between 1.47° and 80° 2θ. An X-ray wavelength of 0.8248 Å was used, calibrated using a mixed LaB_6/Al_2O_3 standard. The powdered samples were carefully tipped into SiO_2 capillaries with attached funnels, which are later snapped off before mounting the capillaries into the sample holders. The samples are then spun in a Eurotherm hot air blower. Heating rates between 2 and 25 °C min^{-1} were used, and the patterns were collected in 60 s segments.

Powder XRD at UTS was performed by Mr Mark Berkahn using a Bruker D8 Discover diffractometer with the following parameters; radiation: Cu $K_{\alpha 1}$ (λ = 1.5046 Å), mode: locked coupled from 1 to 69°, beam power: 40 kV and 40 mA, step size: 0.02° 2θ, scan time: 30 min. Data were collected at room temperature.

Chapter 3:

Preparation of Tetrachloroauric Acid Suitable for Nanoparticle Synthesis

Chapter 3: Preparation of Tetrachloroauric Acid Suitable for Nanoparticle Synthesis[f]

3.1. Introduction

Over the last two decades, interest in AuNPs has increased significantly within the scientific community; as such, a demand for high purity aqueous $HAuCl_4$ exists. A method that has been used for centuries to dissolve gold uses *aqua regia* (Latin for 'royal water'), which is a mixture of concentrated hydrochloric and nitric acids in a molar ratio of ~3:1. This combination dissolves solid gold to produce $HAuCl_4$ via two main reactions:

$$Au_{(s)} + 3HNO_{3\,(aq)} + 4HCl_{(aq)} \rightarrow AuCl_4^-{}_{(aq)} + 3NO_2 + H_3O^+{}_{(l)} + 2H_2O \tag{3.1}$$

$$Au_{(s)} + HNO_{3\,(aq)} + 4HCl_{(aq)} \rightarrow AuCl_4^-{}_{(aq)} + 3NO + H_3O^+{}_{(l)} + H_2O \tag{3.2}$$

Two reasons for the *aqua regia* method's popularity are the ease of attaining such common chemicals and the relatively simple apparatus required. However, a major drawback of this method is that it is very time-consuming. The reaction itself can take up to a few days, which is then followed by a cumbersome workup procedure with repeated cycles of boiling down the solution and diluting with concentrated HCl to remove any remnants of HNO_3 and its by-products, which could inhibit nanoparticle synthesis. Research groups generally address this issue by purchasing $HAuCl_4$ from commercial suppliers, however this can increase laboratory costs significantly, especially when larger quantities of nanoparticles are being prepared. Commercial tetrachloroauric acid as a dry powder ($HAuCl_4.3H_2O$), which is 50% Au by mass, costs up to 18 times more than the same amount of Au in pure metallic form.[g] Furthermore, $HAuCl_4$ powder is extremely hygroscopic, making it difficult to weigh out accurately and requiring it to be stored under strictly anhydrous conditions. In addition, solutions of $HAuCl_4$ can be quite unstable, rapidly returning to metallic gold unless kept under appropriate conditions (e.g. pH < 4 with excess chloride ions).[98] Therefore, due to the time-consuming nature of the *aqua regia* method (particularly if a high-purity product is required) and the cost and instability

---

[f] A significant part of the work presented in this chapter has been published (see King, Massicot and McDonagh, *Metals*, 2015, *5*, 1454-1461). Portions of the experimental work and data processing for the chlorine gas method were performed by Miss Juliette Massicot of l'Université du Maine (France) during her 3-month internship at UTS.

[g] At the time of writing (June 2017), the price of gold was $40 per gram, while 0.5 g of $HAuCl_4.xH_2O$ (x = ~3) from Sigma-Aldrich cost $186, and 5 g cost $965 (AUD).

issues of commercial $HAuCl_4$ powder, a different method of synthesising $HAuCl_4$ for nanoparticle synthesis was sought in this project.

Gold is a highly inert metal and one of the few chemicals that are reactive enough to oxidise gold is chlorine. The reaction of gold with chlorine gas to produce $HAuCl_4$ is shown in Equation 3.3.

$$2Au^0{}_{(s)} + 3Cl_{2\,(g)} + 2HCl_{(aq)} \rightarrow 2HAu^{III}Cl_{4\,(aq)} \tag{3.3}$$

Industrial processes adopted this chemistry as early as the 19th century to dissolve gold from gold-bearing ores.[99–101] This process was quickly replaced by cyanidation in the gold mining industry, however research into the use of halogens, namely chlorine, bromine and iodine, has made a resurgence in recent decades due to environmental concerns associated with cyanide use.[102,103] A number of industrial procedures for ore extraction use chlorine gas injected into the reaction chamber or alternatively water that contains dissolved chlorine gas,[104] or employ the reaction between sodium hypochlorite, hydrochloric acid and sodium chloride (Equation 3.4) to generate chlorine gas *in situ*, which then dissolves the gold as per Equation 3.3.[86,98,105,106]

$$NaClO_{(aq)} + NaCl_{(aq)} + 2HCl_{(aq)} \rightarrow 2NaCl_{(aq)} + Cl_{2\,(g)} + H_2O_{(l)} \tag{3.4}$$

In this chapter, a straightforward method to produce highly stable aqueous solutions of $HAuCl_4$, using the reaction of gold metal and chlorine gas, is presented. Two methods, the chlorine gas and the hypochlorite methods, were examined and due to the instability of the product formed using the latter method, the majority of the study focussed on the chlorine gas method. The purity, the influence of reaction conditions on the reaction rate, and the synthesis of nanoparticles have been investigated.

3.2. Summary of Methods

A comprehensive explanation of both the chlorine gas and hypochlorite methods is given in Chapter 2.1.1. The following is a brief summary of the processes.

Chlorine Gas Method

1. Assemble the reaction apparatus shown in Figure 2.1.
2. Generate $Cl_{2\,(g)}$ by adding concentrated HCl dropwise to $KMnO_{4\,(s)}$, which is a strong oxidant. Bubble the $Cl_{2\,(g)}$ into a flask containing pure water and a pellet (or pellets) of gold.
3. Stir the reaction at the selected temperature (see Section 3.6) until the gold has dissolved. The resulting $HAuCl_4$ solution can then be used without further treatment.

Hypochlorite Method

1. Place a pellet of gold in a flask containing NaClO, NaCl and a stirrer bar.
2. Add concentrated HCl dropwise with stirring until a pH of ~4 is reached.
3. Stopper the flask and stir until all the gold has dissolved.
4. Decant the $HAuCl_4$ solution into a separating funnel and extract the gold chloride ($AuCl_3$) into diethyl ether.
5. Extract the $AuCl_3$ from the ether solution into Milli-Q water and add HCl to convert it to $HAuCl_4$.

Notes and Observations

In the chlorine gas method, care must be taken to ensure all the attachment points in the reaction apparatus are gastight, which may require Parafilm to be wrapped around them. Even though the reaction requires HCl as one of the reactants (Equation 3.3), the addition of HCl to the reaction flask was found to be unnecessary, since sufficient HCl is formed when Cl_2 dissolves in the water. There was no difference in reaction times for solutions with or without added HCl. The flask labelled ‘trap’ in Figure 2.1, between the main reaction flask and the flask containing $Na_2S_2O_{3\,(aq)}$, is included to prevent any of the $Na_2S_2O_{3\,(aq)}$ from contaminating the $HAuCl_{4\,(aq)}$, in the unlikely event that a difference in pressure causes the $Na_2S_2O_{3\,(aq)}$ to be drawn back. The $Na_2S_2O_3$ solution is included to reduce unreacted Cl_2 to Cl^-.

The extraction of $AuCl_3$ into diethyl ether in the hypochlorite method was found to be more effective for concentrated $HAuCl_4$ aqueous solutions than for more dilute ones, but still required at least three extractions with 150 mL portions of ether to remove most of the $AuCl_3$. $AuCl_3$ can move from an aqueous solution saturated with NaCl into diethyl ether,[107] and can move from diethyl ether into pure water.

3.3. Stability of $HAuCl_4$ Solutions

Considering the preparation, setup and reaction times required to synthesise chemical substances, an extended shelf life is a desirable property. This is especially so for commercial or industrial scales where solutions are transported or stockpiled. In this section, the stability of $HAuCl_4$ solutions made by the *chlorine gas method* is directly compared to the stability of solutions produced using the *hypochlorite method*.

Solutions produced by both techniques were tightly stoppered and stored in ambient conditions; observations were made on a daily, and then weekly, basis. For solutions prepared by the hypochlorite method, varying amounts (1, 2 or 10 mL) of 1 M HCl were added in an attempt to stabilise the $HAuCl_4$.[98] However, the solutions with 1 or 2 mL of added HCl were observed to begin precipitating metallic gold within 24 h, and after 2 weeks all of the gold had precipitated, leaving the solution colourless (Figure 3.1 b). The solution with 10 mL of added HCl began precipitating gold within 2–3 days, but then reached an equilibrium, with some of the $HAuCl_4$ remaining in solution. These results suggest that additional HCl is required to stabilise the $HAuCl_4$ solutions. Furthermore, several drawbacks of this method were identified including:

- The reaction time (~3 days, not including workup procedures) and resources required (several litres of diethyl ether) were excessive;
- The uncertainty of final solution concentrations, since not all of the gold could be recovered during extraction;
- The likelihood of NaCl contamination in the final solutions, which would make them unsuitable for nanoparticle synthesis due to the extreme sensitivity of many AuNPs to ionic impurities.[108]

In contrast to solutions made by the hypochlorite method, those made by the chlorine gas method were found to be highly stable, with no precipitation of gold evident in any of the prepared solutions after 12 months (Figure 3.1 a), and still no precipitation in one of the solutions after 3 years (other solutions were used for nanoparticle synthesis). UV-visible spectra were collected for two solutions of different age, one 3 months old and the other 12 months old. The two solutions showed almost identical absorption spectra (Figure 3.2), further confirming the stability of the solutions prepared by this method.

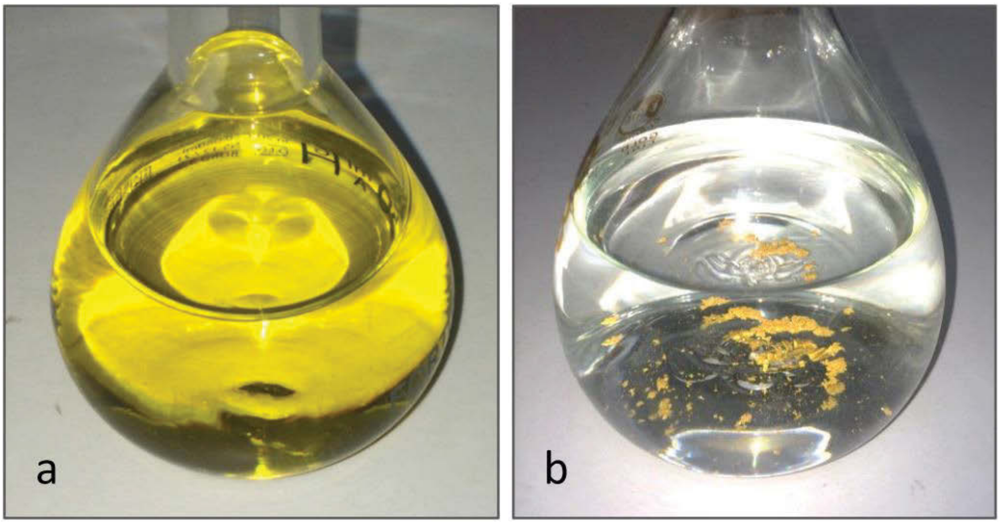

Figure 3.1. Photographs of $HAuCl_4$ solutions prepared by: (a) chlorine gas method and (b) hypochlorite method (where precipitation occurred within ~2 weeks post-synthesis).

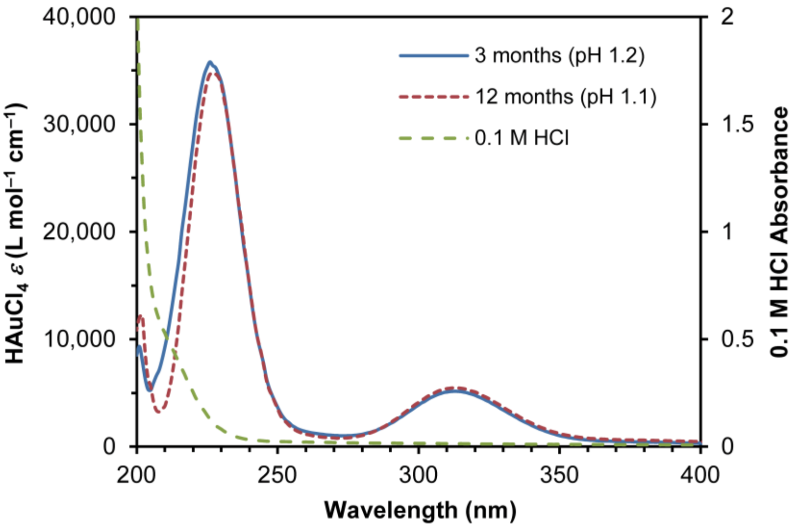

Figure 3.2. UV-visible spectra of 3-month and 12-month-old $HAuCl_4$ solutions in 0.1 M aqueous HCl, synthesised using the chlorine gas method (the spectrum of the HCl background is included for comparison).

The UV-visible spectra of $HAuCl_4$ made by the chlorine gas method (Figure 3.2) are characteristic of $HAuCl_4$ solutions with pH of ~1.[109] The absorption bands at 313 and 226 nm have both been assigned to ligand-to-metal charge transfer (LMCT) from the chloride *p* to the gold *d* orbitals.[110,111] The slight differences in the two spectra in Figure 3.2 can be attributed to the slight difference in pH.

The stability of the $HAuCl_4$ solutions made by the chlorine gas method is attributed to the presence of residual dissolved chlorine and low pH. The concentration of dissolved chlorine in a tightly stoppered 3-month-old solution ($[HAuCl_4] = 0.01025$ M) was measured by iodometric titration to be 8.9×10^{-3} M. This concentration is similar to previous reports of $HAuCl_4$

solutions with dissolved chlorine,[112–114] and is below the chlorine saturation concentration of 0.08 M at 20 °C.[115] The solution pH was measured to be 1.6–1.8, which is well below the maximum pH of 4 required for maintaining stability,[98] and which is in the range where Cl_2 is expected to be the predominant species (rather than HClO or ClO^-).[114] There are two possible sources for the high H^+ ion concentration indicated by the low pH: the dissociation of $HAuCl_4$ into H^+ and $AuCl_4^-$ ($HAuCl_4$ is a strong acid and therefore dissociates almost completely in solution),[116] and the hydrolysis of Cl_2 as shown in Equation 3.5 ($K_{h\,(298)}$ is the hydrolysis equilibrium constant at 298 K).[114] The hydrolysis of Cl_2 also provides the excess chloride ions needed to stabilise the $HAuCl_4$,[98] which is helpful since the addition of stabilising chloride ions in the form of NaCl would make the $HAuCl_4$ unusable for nanoparticle synthesis.[108] One batch of $HAuCl_4$ made by the hypochlorite method was left as synthesised in saturated NaCl solution, without performing the ether extraction procedure, and was found to be stable for over 3 years, but could not be used further within this project.

$$Cl_2 + H_2O \leftrightharpoons H^+ + Cl^- + HClO \qquad K_{h\,(298)} = 3.94 \times 10^{-4} \tag{3.5}$$

Finally, as-prepared $HAuCl_4$ solutions synthesised by the chlorine gas method can be freeze-dried to produce solid gold chloride.

Due to the instability and other issues with solutions prepared by the hypochlorite method, the chlorine gas method is the focus of the remaining sections within this chapter.

3.4. Impurity Analysis of $HAuCl_4$

In order to be suitable for widespread use as a nanoparticle precursor, solutions of $HAuCl_4$ must be free from impurities. The chlorine gas method was designed to minimise the risk of contamination during $HAuCl_4$ synthesis. The reaction vessel contains only 99.99% pure gold, ultrapure water and a stirrer bar that, along with the glassware, has been thoroughly cleaned in *aqua regia* and then ultrapure water to remove all ionic impurities. The absence of a workup procedure removes the risk of contamination post-synthesis. The solid $KMnO_4$ and its reduction by-products are isolated from the main reaction, with a hose used to transport the generated Cl_2 gas to the reaction vessel, however to confirm that no manganese by-products entered the $HAuCl_4$ solution via the hose, ICP-MS was performed by Dr David Bishop (UTS) on two of the synthesised $HAuCl_4$ solutions. The levels of gold detected closely matched the known concentrations of the diluted solutions, and no manganese was detected (Table 3.1), confirming the purity of the synthesised solutions.

Table 3.1. ICP-MS data for diluted aqueous $HAuCl_4$.

Sample	$[HAuCl_4]$ (mol L^{-1})	$[^{197}Au]$ (ppb)*	$[^{55}Mn]$ (ppb)
1	4.0×10^{-6}	929.6	0.000
2	3.7×10^{-6}	686.8	0.000

* ppb (parts per billion) = μg L^{-1}.

3.5. Spectral Dependence on pH

As mentioned previously, the absorption spectrum of $HAuCl_4$ is dependent on the pH of the solution. This dependence is due to the hydrolysis of $AuCl_4^-$ to form a range of species with increasing pH,[116–120] as depicted in Figure 3.3. As the pH increases, chloride ligands on the square planar $AuCl_4^-$ complex are replaced with hydroxide ligands, which reduces the number of electrons available for the LMCT transition, resulting in a blue-shift and decrease in intensity of the absorption band at ~315 nm.[117]

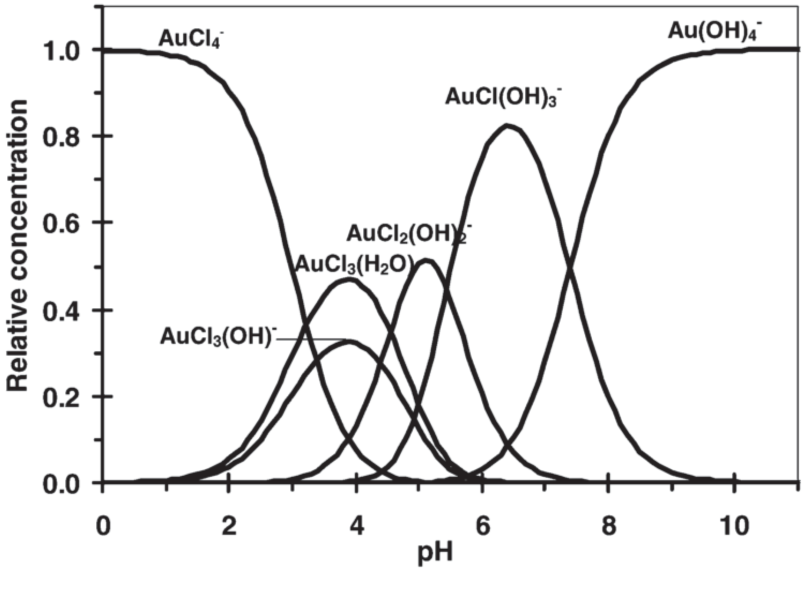

Figure 3.3. Relative equilibrium concentration of gold complexes as a function of pH. Image reproduced from Moreau *et al.*[118]

An as-synthesised solution of $HAuCl_4$ with a concentration of 0.026 M and pH of 1.5 was diluted with Milli-Q water by a factor of two (to 0.013 M) and then divided into three portions. Each of the three samples was acidified with concentrated HCl to pH 1.0, 1.5 and 1.9, as measured by a pH meter. The UV-visible spectra were then collected, and are shown in Figure 3.4. The spectra demonstrate a blue-shift and decreased peak intensity with increasing pH, which is consistent with literature reports.[116,117]

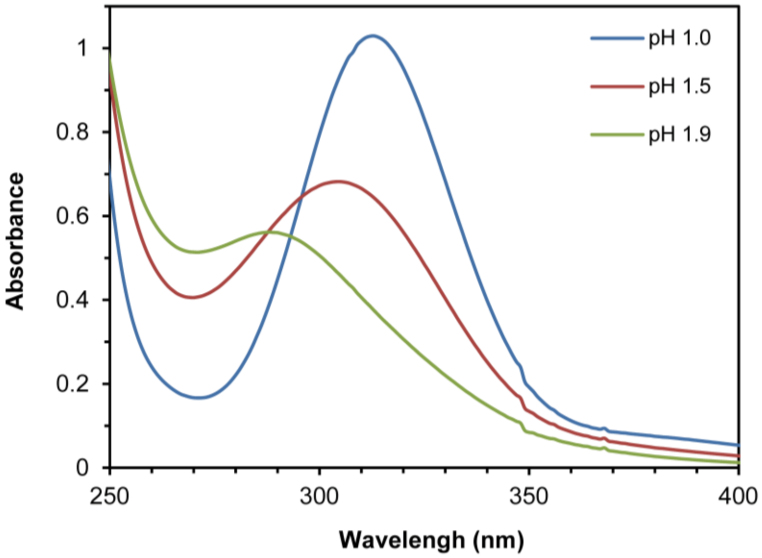

Figure 3.4. UV-visible spectra of $HAuCl_{4\,(aq)}$ solutions at different pH levels.

When diluting the as-synthesised solutions of gold chloride to obtain UV-visible spectra, aqueous HCl should be used to avoid hydrolysis of the $AuCl_4^-$. Figure 3.5 shows the absorption spectra of two 3.2×10^{-5} M solutions of $HAuCl_4$, where one was diluted with 0.1 M HCl and the other with Milli-Q water. For the solution diluted with water, both of the absorption bands have disappeared and been replaced by absorption at wavelengths shorter than 250 nm, indicating that hydrolysis has taken place.

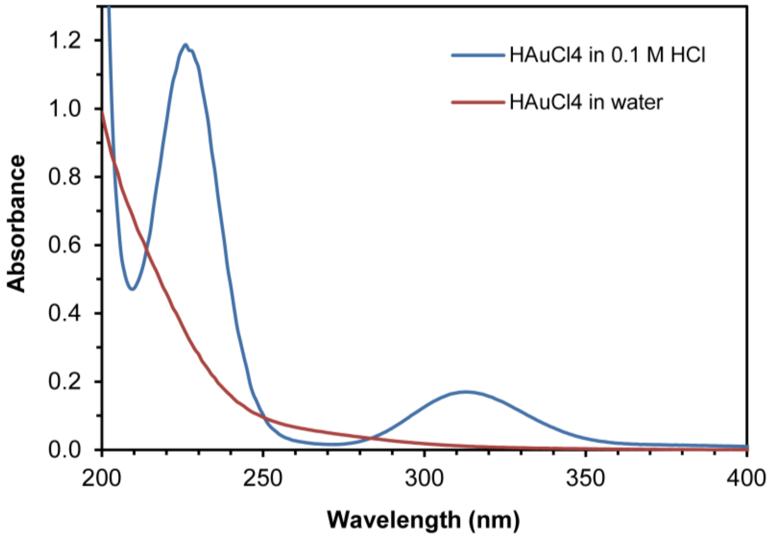

Figure 3.5. UV-visible spectra of 3.2×10^{-5} M $HAuCl_4$ in 0.1 M HCl and in water.

3.6. Reaction Rate

The reaction rate of any synthesis method is intrinsically linked to its feasibility. In most circumstances an increase in reaction rate is desired, as larger quantities of the product can be synthesised in a shorter period of time. A common method to increase the rate of a reaction is to raise the temperature. In this section, the effects of the reaction temperature and the surface area of the gold pellet are explored.

Qualitatively, the reaction rate of the chlorine gas method at room temperature is quite slow, and is comparable to the rates of the hypochlorite and *aqua regia* methods, with 200–300 mg of gold taking 3–5 days to dissolve completely in all three methods. However, it was found that a small increase in temperature (by ~25 °C) significantly increased the reaction rate of the chlorine gas method, with a pellet of gold dissolving in 35 h at 50 °C, compared to ~120 h at room temperature (Figure 3.6). Increasing the temperature up to 70 °C increased the reaction rate, however the effect was only marginal, with complete dissolution occurring in 31 h at 70 °C (Figure 3.6). The observed relationship between the reaction rate and temperature suggests that a process in addition to reaction kinetics is involved. Alkan *et al.* reported that the solubility of chlorine gas in water significantly diminishes with increasing temperature, from 0.082 M at 20 °C to 0.025 M at 70 °C.[115] This reduction in chlorine solubility would therefore negate the effect of increased reaction kinetics with higher temperatures, as there is less chlorine available for the reaction to proceed.

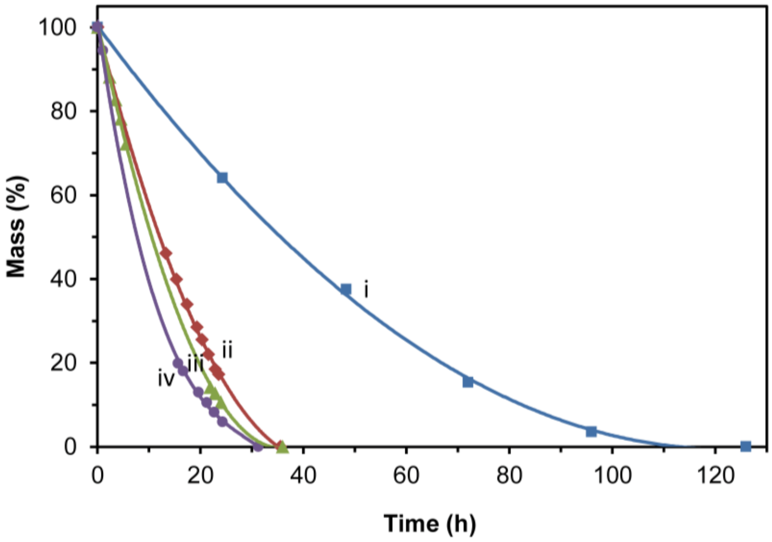

Figure 3.6. Reaction times at different temperatures, expressed as the percentage remaining of the initial mass of gold as a function of time: (i) 281 mg pellet at room temperature; (ii) 268 mg pellet at 50 °C; (iii) 319 mg pellet at 60 °C; (iv) 357 mg pellet at 70 °C. Note: pellets were used as-received from the supplier, hence the range of masses used.

Another method to increase the rate of reaction involves expanding the surface area of the gold. The gold pellets as purchased are roughly spherical in shape, with diameters typically around 2–3 mm. An expansion in surface area was achieved by mechanically flattening the pellets to thicknesses less than 1 mm (Figure 3.7). In flattening the gold pellets, an almost three-fold increase in reaction rate was achieved, where complete dissolution occurred within ~12 h at 50 °C, compared to 35 h for the spherical pellets.

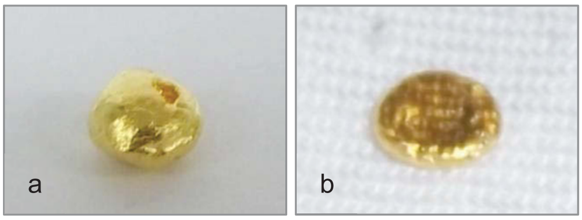

Figure 3.7. Photographs of a gold pellet (a) as purchased and (b) after mechanical flattening.

The approximate surface areas of the spherical pellets and cylindrical flattened pellets were calculated using the equations for the surface area and volume of spheres and cylinders. Spherical pellets 2–3 mm in diameter have volumes in the range 4–14 mm^3, and surface areas of 13–28 mm^2. Cylinders of the same volume with a height of 0.5 mm have diameters of 3.2–6.0 mm. The surface area of these cylinders is therefore 21–66 mm^2, which is roughly twice the area of the spheres. The three-fold increase in reaction rate with a calculated two-fold increase in surface area may be explained by the presence of surface roughness, which was ignored in the calculations. Past research has also shown that the surface orientation and topology of a material can have a significant effect on its adsorption and etching rate.[121,122] It is possible that the mechanical flattening has introduced strain and non-equilibrium surface topologies that lower the activation energy required for chlorine to react with the gold, thereby increasing the reaction rate. It should be noted that the flattening process could introduce metallic contamination; this was prevented by placing the gold between layers of cotton fabric or sheets of polycarbonate prior to flattening.

3.7. Scalability and Concentration Determination

The chlorine gas method for producing $HAuCl_4$ can be scaled from the millilitre to the litre scale by adjusting the quantities of the starting materials. This scalability, combined with a shelf life on the order of a few years, allows large quantities of aqueous $HAuCl_4$ to be produced in one batch, which can save significant amounts of time in the laboratory by not requiring fresh batches of $HAuCl_4$ to be synthesised every time it is needed. The concentration of the prepared solutions can also be controlled and accurately determined. Since the reaction is quantitative with a 1:1 ratio between Au and $HAuCl_4$, the moles of $HAuCl_4$ in the final solution can be calculated from the initial mass of gold used. The final concentration can then be controlled and/or measured by the volume of water used. The most concentrated solution prepared in this study used 2.353 g of gold pellets and 150 mL of water, giving a 0.080 M $HAuCl_4$ solution.

This method of determining concentration is more accurate and straightforward than using UV-visible spectroscopy, as the latter requires accurate dilutions with HCl and accurate pH measurements to be performed, along with knowledge of the molar attenuance coefficient at that particular pH.

3.8. Nanoparticle Synthesis

3.8.1. Aqueous AuNPs

As a test of the suitability of the $HAuCl_4$ solutions prepared by the chlorine gas method for nanoparticle synthesis, citrate-stabilised aqueous AuNPs (citrate@AuNPs) were synthesised from an as-prepared $HAuCl_4$ solution. The citrate anions stabilise the AuNPs by electrostatic repulsion and any ionic impurities can disrupt that repulsion, causing the nanoparticles to irreversibly aggregate and “crash” out of the suspension.[108]

The synthesis of citrate@AuNPs proceeded as described in the literature[123] (see Chapter 2.1.2). The UV-visible spectrum of the colloid (shown in the following section, Figure 3.9) shows the plasmon resonance peak to be at 519 nm, which is characteristic of small AuNPs,[68] and analysis by SEM shows the particles to be fairly monodisperse with an average diameter of ~12 nm (Figure 3.10 a). The AuNPs were observed to remain in a stable colloidal suspension for at least one month, demonstrating the high purity of the $HAuCl_4$ solution, after which time they were given to a collaborating research group for their experiments.

3.8.2. Organic AuNPs

The primary focus of this thesis is on the thermal stability of ligand-stabilised AuNPs. All of the chosen ligands to be tested are soluble in organic solvents; as such the AuNPs were synthesised to also be soluble in organic solvents. Three varieties of AuNPs were made, OA@AuNPs, BT@AuNPs and OT@AuNPs, and several batches were produced throughout the project as required. The $HAuCl_4$ solutions produced by the chlorine gas method were found to be suitable for all of the AuNPs synthesised.

The general procedure for synthesising organic-soluble AuNPs using the two-phase Brust-Schiffrin method[124] is illustrated in Figure 3.8. First, the $HAuCl_4$ is transferred from water into the organic solvent toluene using the phase transfer agent tetraoctylammonium bromide (TOAB). The solution is stirred vigorously until the aqueous phase has become colourless. The aqueous phase is usually then separated from the organic phase and discarded, with the exception of the method for BT@AuNPs, where the aqueous phase isn’t separated until after the AuNPs have formed. The desired stabilising compound, in this case oleylamine, 1-butanethiol or 1-octanethiol, is added to the organic phase, followed by an aqueous solution of the reducing agent $NaBH_4$, which reduces the gold(III) chloride to gold(0), observed as a rapid colour change from dark orange to deep burgundy. The $NaBH_4$ is dissolved in a small amount of ice-cold water in order to slow down its decomposition reaction with water, which produces hydrogen gas. Therefore the $NaBH_4$ solution must be prepared immediately before using it. The reduced gold atoms cluster together into nanoparticles, and the stabilising molecules attach themselves to the surface of the particles via the sulfur or nitrogen atoms, preventing any further aggregation of the gold. Researchers have developed multiple variations of this procedure in order to create AuNPs with different sizes, shapes and stabilising ligands.

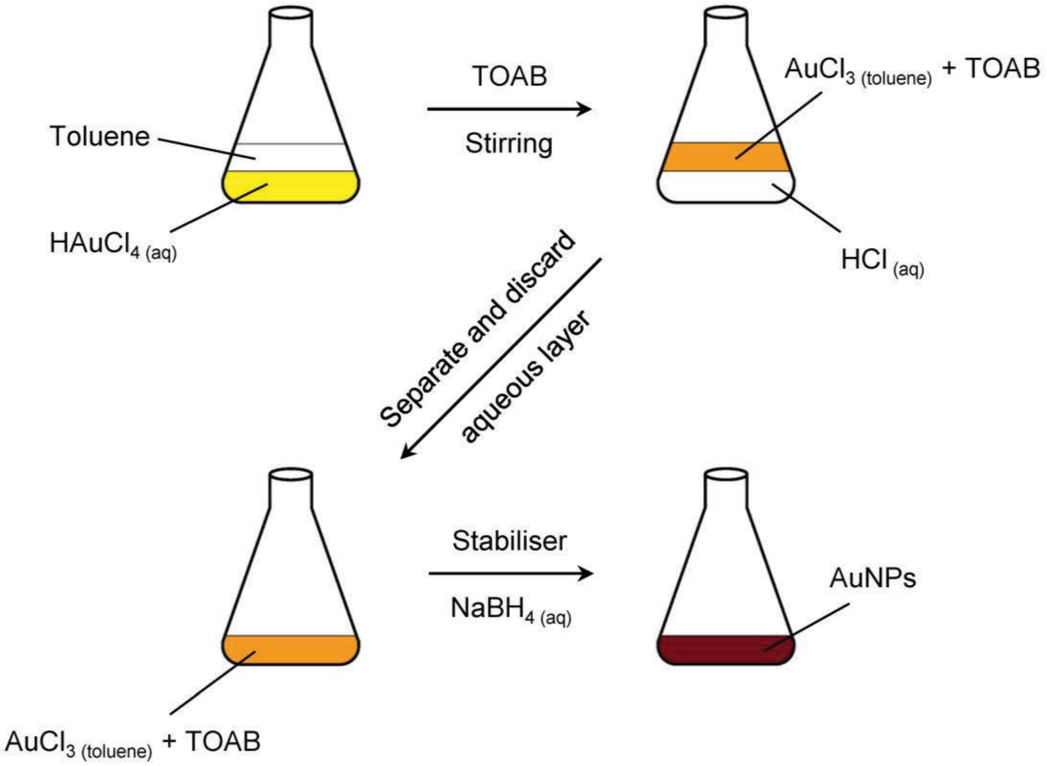

Figure 3.8. Schematic illustration of the general synthesis procedure for organic AuNPs.

The AuNPs synthesised for this project were washed to remove the TOAB, $NaBH_4$ by-products and excess unbound stabilising molecules. The washing process uses a difference in solubility to separate the stabilised AuNPs from the crude solution. The AuNPs are insoluble in methanol and ethanol; therefore slowly adding the crude colloid to a much larger volume (at least 3 times more) of either methanol or ethanol caused the AuNPs to clump together and precipitate while the unwanted by-products remain dissolved, allowing the AuNPs to be collected by centrifugation and rinsed with additional alcohol. The AuNPs can then be stored as a powder and resuspended as required. AuNPs stabilised with thiols can be stored in powder form for long periods of time (months to years), however the AuNPs stabilised with oleylamine were found to become insoluble after a few weeks of storage in powder form. This short shelf-life is likely due to the fact that amines bind more weakly to gold than thiols do,[125,126] which may allow the amine ligands to be more easily disrupted, causing the AuNPs to aggregate in a shorter period of time than with thiol ligands. Fortunately, the OA@AuNPs were found to be highly stable (> 2 years) when kept in the as-synthesised crude suspension, likely due to the presence of excess oleylamine as well as TOAB, which can also act as a stabiliser. As a result, the crude colloid was kept as a stock solution, and small portions of OA@AuNPs were removed and washed when needed. It was also observed that washing the OA@AuNPs more than 3 times would lead to them becoming insoluble, suggesting the oleylamine ligands can be at least partially removed from the AuNPs during the washing process.

The UV-visible spectra of OA@AuNPs, BT@AuNPs and OT@AuNPs, along with the aqueous citrate@AuNPs, are shown in Figure 3.9. The OA@AuNPs and OT@AuNPs have plasmon resonance peaks at 524 and 517 nm, respectively. The BT@AuNPs are smaller than the other AuNPs produced, and are on the size threshold for the emergence of the LSPR phenomenon in AuNPs.[127] As a result, only a weak plasmon resonance peak is evident in the UV-visible spectrum, and the colloid appears dark brown in colour.

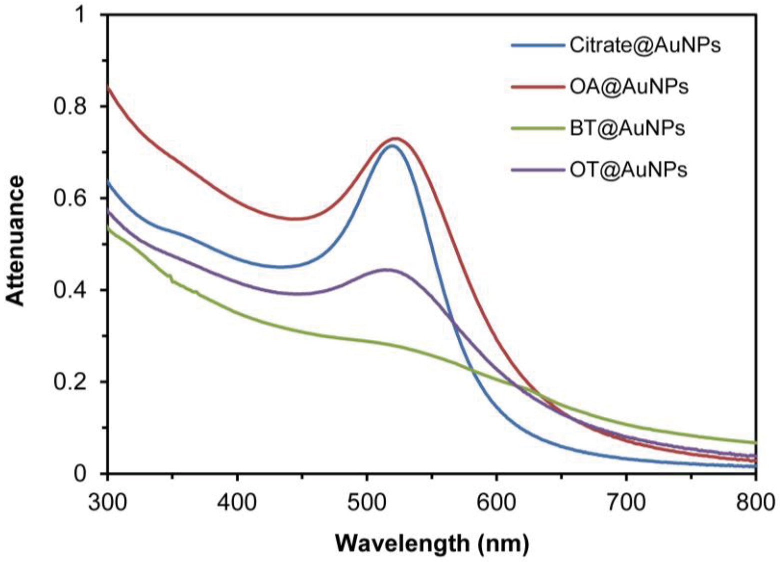

Figure 3.9. UV-visible spectra of aqueous and organic AuNPs.

Figure 3.10 shows SEM images of different types of AuNPs synthesised for this project. The particles can be seen to be spherical in shape, and are reasonably monodisperse with average diameters of 5 nm for OA@AuNPs, 3 nm for BT@AuNPs and 5 nm for OT@AuNPs. These results confirm the suitability of the synthesised $HAuCl_4$ solutions as nanoparticle precursors.

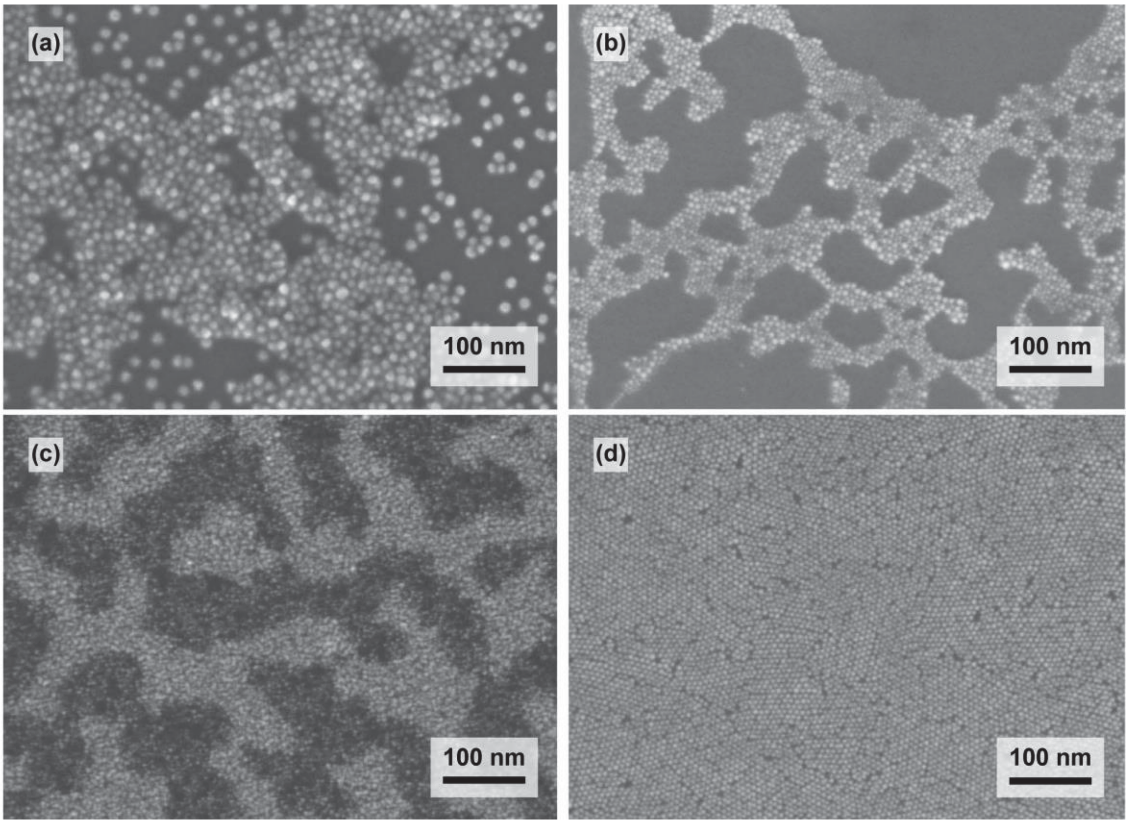

Figure 3.10. SEM images of (a) citrate@AuNPs, (b) OA@AuNPs, (c) BT@AuNPs and (d) OT@AuNPs.

3.9. Summary

A new method for tetrachloroauric acid ($HAuCl_4$) synthesis, labelled the “chlorine gas method,” is presented in this chapter. The method has several advantages over the commonly used *aqua regia* method, as well as the less common hypochlorite method. The chlorine gas method uses a known reaction of gold with chlorine and is adapted from past ore-processing techniques into a straightforward, laboratory-scale procedure. It was not feasible to replicate the *aqua regia* method within this study, however the hypochlorite method (also adapted from ore-processing techniques) was performed for direct comparison.

After a long-term study of the stability of the $HAuCl_4$ solutions produced by the chlorine gas and hypochlorite methods, it was determined that the chlorine gas method is far superior. Solutions synthesised by the hypochlorite method started to precipitate gold as early as 24 h post-synthesis, whereas those prepared by the chlorine gas method remained stable until the completion of the study. The latter observation was confirmed using UV-visible spectroscopy, and the high stability was attributed to the low pH and the presence of dissolved chlorine. The hypochlorite method was then excluded from the remainder of the study.

It was determined by ICP-MS and through the synthesis of a stable aqueous colloid of AuNPs that the $HAuCl_4$ solutions prepared using the chlorine gas method do not contain any interfering impurities. The $HAuCl_4$ spectral dependence on pH was explored and found to be consistent with the literature.

An investigation into the reaction rate found that a four-fold increase could be achieved by increasing the reaction temperature from room temperature to ~50 °C and increasing the surface area of the gold. Heating the reaction to higher temperatures did not lead to any significant increase in reaction rate as the solubility of chlorine in water is greatly reduced at elevated temperatures. Increasing the surface area of the gold was found to be particularly effective for decreasing the reaction time, though care should be taken to avoid a risk of contamination of the gold.

The chlorine gas method can be scaled up to produce larger quantities of $HAuCl_4$, and the concentration of the prepared solutions can be accurately determined from the quantities of gold and water used. These properties, along with the high purity, long shelf life, straightforward procedure and significant reduction in expense, make the chlorine gas method ideal for nanoparticle synthesis. This has been demonstrated by the preparation of large quantities of stable, monodisperse colloids of AuNPs in both aqueous and organic solvents. The organic AuNPs were then used for the thermal stability studies for this project, as presented in the following chapters.

Chapter 4:

Influence of Stabilising Molecules on the Thermal Stability of Gold Nanoparticles

Chapter 4: Influence of Stabilising Molecules on the Thermal Stability of Gold Nanoparticles[h]

4.1. Introduction

The ability of nanoparticles to be functionalised with a wide range of molecules allows for significant alterations in their behaviour and characteristics, and is vital to their practical application.[7,11,128,129] This ability stems from the strong affinity of gold for sulfur,[126,130] and to a lesser extent nitrogen,[125,131] along with the large variety of chemical reactions available for synthesising molecules with sulfur or nitrogen functional groups in the form of thiols or amines. A thorough understanding of the thermal stability of AuNPs is essential for the improved development of nanomaterials, for applications such as printed electronics, catalysis and sensing. Most of the studies on the sintering of AuNPs focus on lowering the temperature at which sintering occurs in order to create plastic-compatible sinter inks for flexible electronics.[17,31] In contrast, relatively little is known about ligand-stabilised AuNPs with a much higher degree of thermal stability. Generally in the field of catalysis, the AuNPs must be free of organic ligands so that the surface is available to catalyse reactions. Therefore the research into preventing the thermal sintering of AuNPs in catalytic systems has focussed on immobilising the AuNPs on a substrate or encapsulating within a mesoporous inorganic oxide matrix (see Chapter 1.2.3). As such, little to no research has been done to explore the potential for stabilising AuNPs against sintering using organic molecules. Increasing the thermal stability of AuNPs through the use of organic ligands may facilitate studies in probing their optical properties at elevated temperatures, and may enable their use as optical sensors in high temperature environments.

The photochemical and photophysical behaviour of AuNPs functionalised with phthalocyanine (Pc) molecules has been recently investigated.[132,133] Pc complexes are a class of dye with very strong optical absorption bands and, in addition to their long-time use in textile dyeing,[134] have applications as organic conductors, catalysts, gas sensing thin films, and as photosensitisers in both photovoltaic devices and photodynamic therapy for cancer treatment.[135,136] Importantly for this work, Pcs are highly thermally stable.[137] We therefore hypothesised that Pcs would impart high thermal stability to AuNPs and delay the onset of sintering.

---

[h] A significant part of the work presented in this chapter has been published (see King *et al.*, *Nanotechnology*, 2016, *27*, 215702; and King *et al.*, *J. Phys. Chem. C*, 2017, *121*, 13944–13951).

The chemical properties of Pcs can be altered through the attachment of ligands and by changing the central metal atom, making them remarkably versatile.[136] Of particular interest to this study is the use of ruthenium as the central metal (Figure 4.1), which has an octahedral geometry, allowing it to bind to six other atoms. This then facilitates the binding of functional ligands along the axis perpendicular to the plane of the macrocycle, whereas other commonly used transition metals, such as zinc and copper,[138,139] restrict the functionalisation of the complex to the periphery of the macrocycle. The RuPc complex [RuPc(4-py(CH_2)$_3$SAc)(4-py^{t}Bu)], which is a new compound synthesised and characterised by Dr Susan Shimmon (UTS), was chosen as the starting point for this study. The complex has two different axial ligands, 4-*tert*-butylpyridine (4-py^{t}Bu) and *S*-[3-(pyridin-4-yl)propyl]thioacetate (4-py(CH_2)$_3$SAc). The *tert*-butyl group on the 4-py^{t}Bu ligand greatly enhances the solubility of the Pc complex in organic solvents, and the 4-py(CH_2)$_3$SAc ligand is capable of binding to gold via the sulfur atom, resulting in the cleavage of the protective acetyl group.[94]

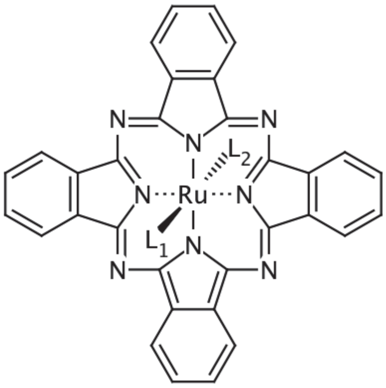

Figure 4.1. Structure of ruthenium phthalocyanine, with ligands L_1 and L_2 bound along the perpendicular axis of the macrocycle, through the ruthenium atom.

In the first part of this study, AuNPs were functionalised with the chosen RuPc complex, and the resulting RuPc-AuNP nanocomposite was characterised by UV-visible spectroscopy, SEM, TEM, EDS, TGA/DSC and LA-ICP-MS. The thermal stability of the nanocomposite was then tested by measuring its resistance as it was heated to determine the temperature of the sintering event (T_{SE}), defined here as the temperature of the maximum rate of change in resistance. The thermal stability of a film of BT@AuNPs was measured as a comparison, since these have been well characterised and are known to have relatively low thermal stability.[15,16,31] The sintered films of the nanocomposite were then analysed by SEM, EDS and LA-ICP-MS. The results, as detailed in this chapter, showed the RuPc-AuNP nanocomposite to be resistant to sintering at temperatures up to 320 °C, which is significantly higher than the T_{SE} of ~150 °C obtained for the BT@AuNPs.

A recent study that investigated the stability of the Au–S bond in thiolate-stabilised gold nanoclusters found that the Au–S bond was vulnerable to decomposition at temperatures as low as 150 °C, and that the aryl- or alkylthiolate stabilisers were almost completely removed by 250 °C.[58] It was therefore hypothesised for the second part of this study that stabilising molecules of high thermal stability need not be anchored to the AuNPs by Au–S bonds in order to protect them from sintering, as these bonds will be broken well before the T_{SE}. In other words, AuNPs could be stabilised to higher temperatures by the simple inclusion of thermally stable non-thiolated compounds. To test this, a range of compounds with and without functional groups to anchor them to the AuNP surface were compared for their effect on the thermal stability of AuNPs. The compounds were chosen based on their thermal stability, as determined by TGA, as well as their solubility, to ensure they could be dissolved in the same solvent as the AuNPs.

4.2. Ruthenium Phthalocyanine-Stabilised Gold Nanoparticles

The RuPc-AuNP nanocomposite was synthesised by introducing the complex [RuPc(4-py(CH$_2$)$_3$SAc)(4-py^{t}Bu)] to OA@AuNPs (Figure 4.2), which displaced the weakly bound oleylamine ligands on the AuNPs. The displaced oleylamine was removed by adding ethanol to the crude solution, collecting the precipitated particles by centrifugation and washing them with repeated cycles of suspension in ethanol and centrifugation. It was found that the RuPc complex is only sparingly soluble in ethanol, so very little of the excess RuPc could be removed. As such, the product is here referred to as a RuPc-AuNP nanocomposite, rather than RuPc@AuNPs. The AuNPs within the nanocomposite remained stable throughout the washing process; they could still be readily resuspended in DCM, chloroform or toluene after being subjected to at least ten ethanol suspension/centrifugation cycles.

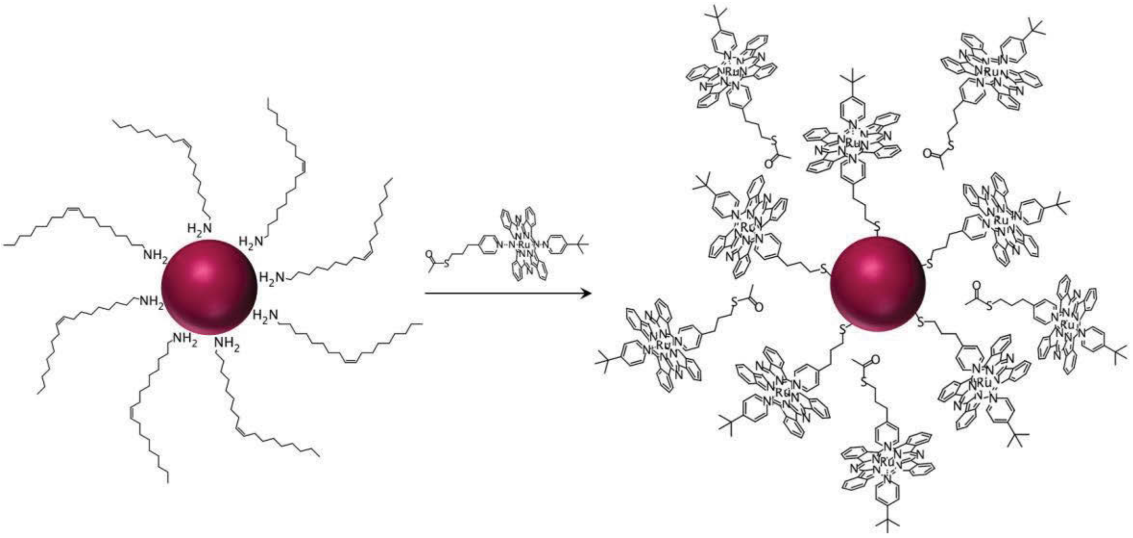

Figure 4.2. Schematic illustration of the functionalisation of OA@AuNPs with the RuPc complex.

4.2.1 Characterisation of RuPc-AuNPs

Solutions of RuPc-AuNPs were intense blue in colour, in contrast to the deep red of the OA@AuNPs. The blue colour arises from the strong optical absorption of the RuPc complex at 625 nm, rather than from aggregation of the AuNPs (which can cause a red-shift of the LSPR wavelength and therefore a blue-shift in the colloidal colour).[108] The UV-visible spectra of the nanocomposite, OA@AuNPs and the [RuPc(4-py(CH$_2$)$_3$SAc)(4-py^{t}Bu)] complex are shown in Figure 4.3. The spectrum of the RuPc-AuNPs shows very similar features to that of the pure, unbound RuPc complex. An additional absorbance band around 520 nm that is assigned to the AuNPs is apparent upon subtracting the spectrum of RuPc from that of the RuPc-AuNPs. The spectrum of [RuPc(4-py(CH$_2$)$_3$SAc)(4-py^{t}Bu)] is consistent with the spectra reported for other RuPc complexes.[135] A strong Q-band absorption is observed at 625 nm ($\varepsilon = 80\ 600$ L mol^{-1} cm^{-}

^{1}), and an intense Soret band (B-band) is found at 316 nm (ε = 112 000 L mol^{-1} cm^{-1}), both of which have been assigned to $\pi \rightarrow \pi^*$ transitions within the Pc macrocycle. Both bands are accompanied by weaker peaks at 570 and 377 nm, respectively. These absorption bands have been ascribed to charge transfer transitions, though their exact nature is uncertain.[140]

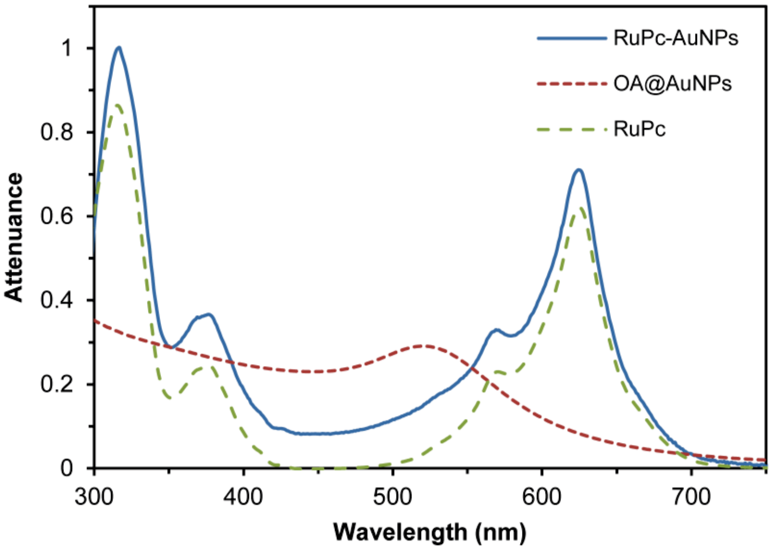

Figure 4.3. UV-visible spectra of RuPc-AuNPs compared to [RuPc(4-py(CH$_2$)$_3$SAc)(4-py^{t}Bu)] and OA@AuNPs (arbitrary scaling).

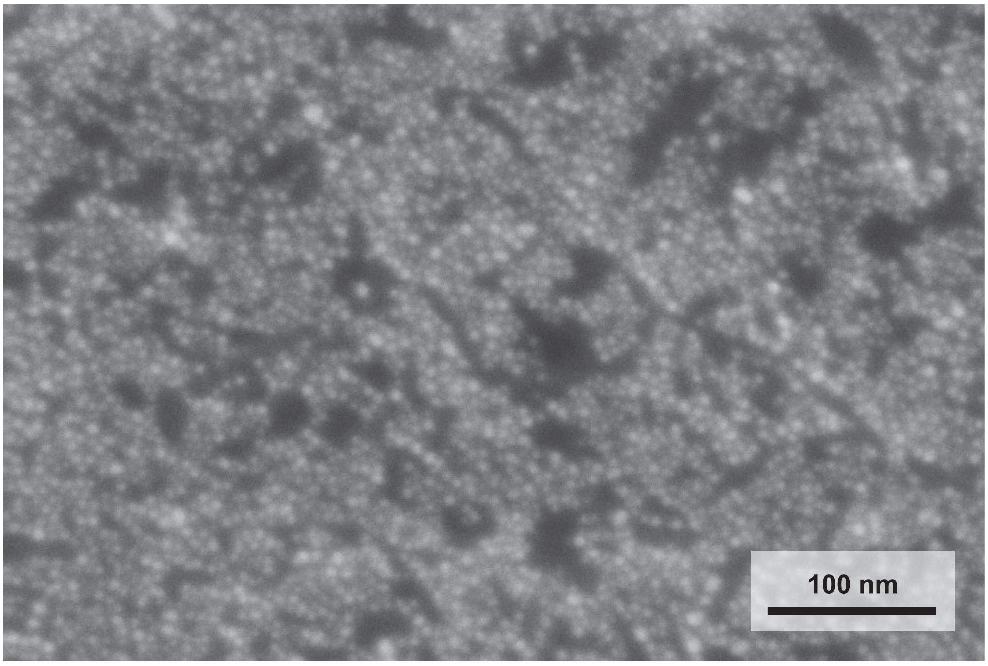

Figure 4.4. SEM image of RuPc-AuNPs.

The RuPc-AuNPs were analysed by SEM (Figure 4.4) and TEM (Figure 4.5). Figure 4.4 shows AuNPs that closely resemble the original OA@AuNPs (Figure 3.10 b), confirming that the AuNPs resisted aggregation upon introduction of the RuPc complex. TEM analysis performed by Dr Annette Dowd (UTS) reveals the AuNPs to have an average diameter of

5.3 nm with a standard deviation of 1.0 nm (Figure 4.5 a). High resolution TEM shows the AuNPs to be crystalline, and sometimes twinned. Figure 4.5 b shows a 6 nm nanocrystal with the face-centred cubic (fcc) structure of gold, where the 2.35 Å {111} planes and 1.44 Å {220} planes are visible. These planes can also be seen in the selected area electron diffraction (SAED) pattern (Figure 4.5 b inset).

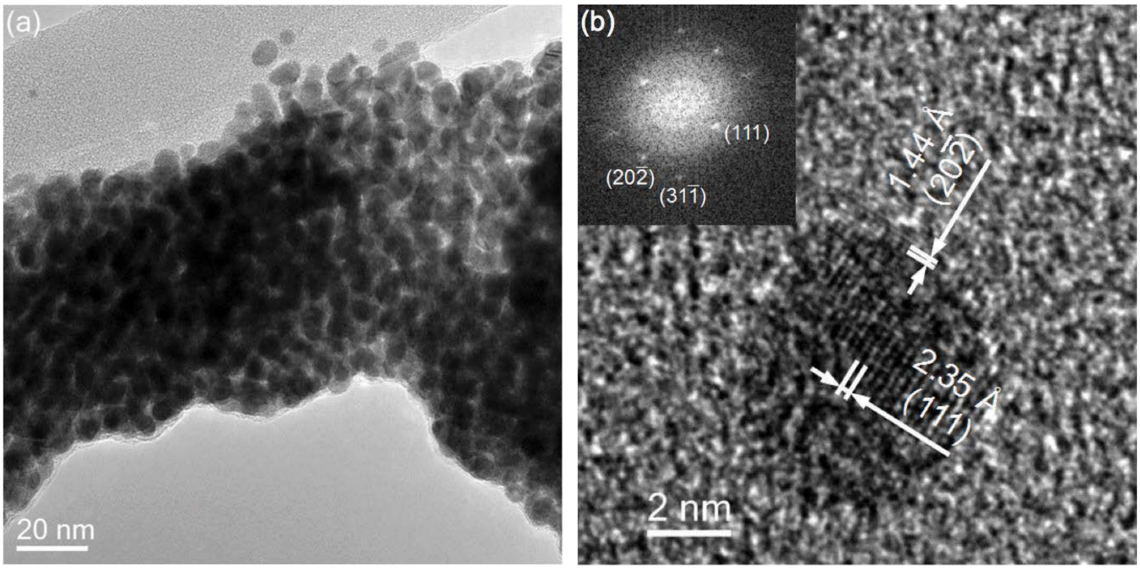

Figure 4.5. TEM images taken by Dr Annette Dowd (UTS) of (a) nanocomposite containing 5 nm diameter AuNPs functionalised with [RuPc(4-py(CH$_2$)$_3$SAc)(4-py^{t}Bu)] and (b) a twinned fcc AuNP oriented close to [1$\bar{2}$1] (inset shows the SAED pattern).

Table 4.1. Atomic ratio of elements in various regions of a drop cast sample of RuPc-AuNPs.

Spectrum	Au : Ru	S : Ru	O : Ru	C : Au
1	2.8	0.82	2.5	38
2	3.0	0.87	3.2	47
3	9.9	1.1	17	57
4	15	1.3	3.8	11
5	0.81	0.86	1.1	56
6	5.3	1.0	11	71
7	0.84	0.84	1.0	61
Average	5.4	0.97	5.7	49

Elemental analysis of the RuPc-AuNPs nanocomposite was obtained by EDS during SEM experiments, and the calculated ratios of selected elements are displayed in Table 4.1. The ratio of gold to ruthenium varied across different regions of the sample, suggesting a somewhat uneven distribution of the excess RuPc complex in the drop cast sample, which likely occurred as the solvent dried. Sulfur and ruthenium were present in the sample in an approximately 1:1

atomic ratio, as expected from the stoichiometry of the RuPc complex, along with a high concentration of carbon. The presence of oxygen in the unheated sample, despite there being no oxygen in the RuPc complex or in the AuNPs, suggests the measured oxygen content is from other sources such as the surface of the silicon substrate, which likely accounts for the large variations in the ratio of oxygen to ruthenium.

4.2.2 Sintering and Thermal Analysis of RuPc-AuNPs

The thermal stability of RuPc-AuNP films was examined by heating them at a constant rate while measuring the electrical resistance. The sintering event is characterised by a significant drop in resistance, as the nanocomposite rapidly transitions from discrete nanoparticles to a relatively continuous film of gold. As discussed in Chapter 1.2.2, the rate of heating affects the temperature at which AuNPs sinter; therefore the heating rate was kept consistent at 10 °C min^{-1} throughout this project to allow for direct comparisons between samples to be made.

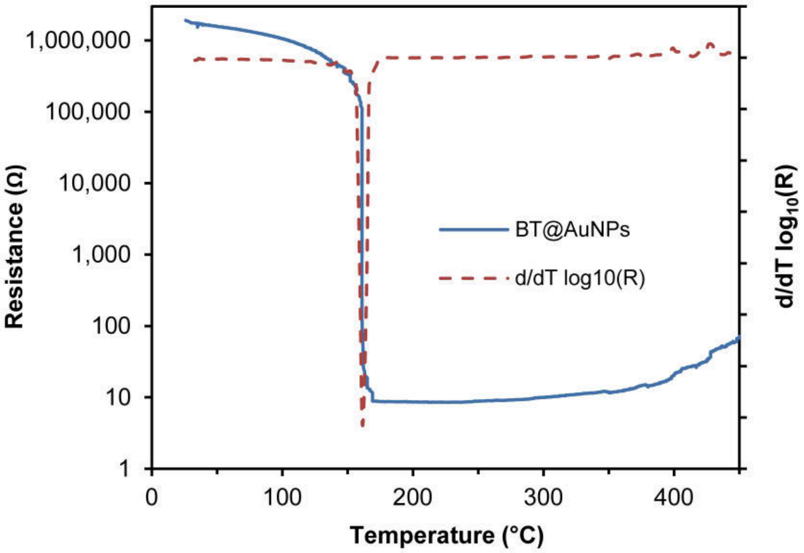

Figure 4.6. Graph of the raw resistance data as a function of temperature (solid line) and the calculated derivative (dashed line) for a film of BT@AuNPs, heated at 10 °C min^{-1} in air.

The validity and reliability of the experimental apparatus was first confirmed by measuring the T_{SE} of films of BT@AuNPs, which are known to sinter at ~150 °C.[20] Five iterations of the experiment gave temperatures for the sintering event in the range 145–160 °C. The data from one of these experiments are shown in Figure 4.6. The maximum rate of change in resistance, which is used to define the T_{SE}, was determined by calculating the first derivative of the log of the resistance, and is also plotted in Figure 4.6. The graphs for each experiment with BT@AuNPs displayed the same general features: a gradual decline in resistance over the first ~100 °C, a very sharp drop in resistance of 4–5 orders of magnitude during the sintering event (which was accompanied by an observable colour change from dark brown to yellow), a stable low resistance for the next ~150 °C, and finally a gradual increase in resistance above 350 °C. This final increase in resistance is likely caused by the gold film breaking apart again to form islands,[141] which will be discussed in more detail in Chapter 5.

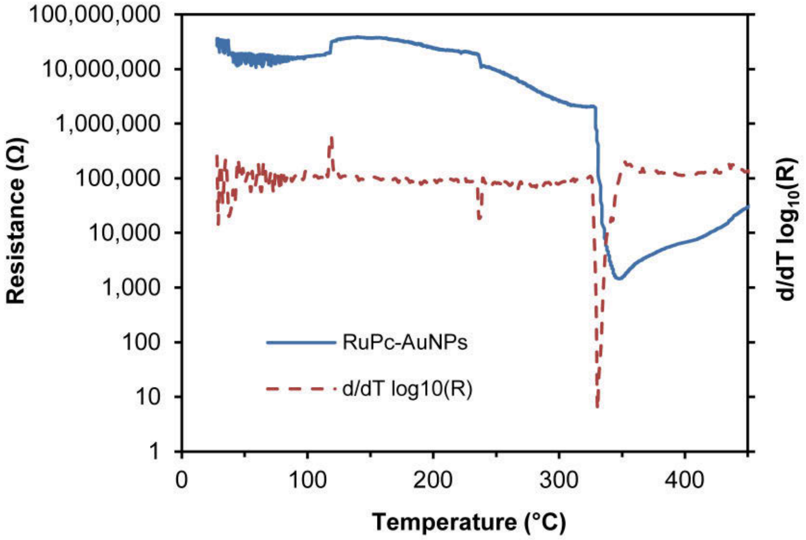

Figure 4.7. Graph of the raw resistance data as a function of temperature (solid line) and the calculated derivative (dashed line) for a film of RuPc-AuNPs, heated at 10 °C min^{-1} in air.

The data from a sintering experiment using the RuPc-AuNP nanocomposite are shown in Figure 4.7. The nanocomposite displayed a remarkably high thermal stability, with a T_{SE} of 320–330 °C, which is ~170 °C higher than that of BT@AuNPs. The T_{SE} of RuPc-AuNPs is also much higher than those reported for AuNPs stabilised with longer chain alkanethiols, such as 1-tetradecanethiol ($T_{SE} = 220$ °C).[15,29] Another interesting feature is the difference in the magnitude of the resistance for BT@AuNPs and RuPc-AuNPs, both before and after the sintering event. The initial resistance of RuPc-AuNP films is an order of magnitude greater than that of BT@AuNP films, which can be attributed to a greater separation of the AuNPs in the former, due to the larger size and greater abundance (as determined by TGA, below) of the stabilising RuPc complex compared to the 1-butanethiol stabiliser. The lowest resistance upon sintering is also higher in films of RuPc-AuNPs than of BT@AuNPs (~1.5 kΩ versus ~10 Ω). This increased resistance in the sintered gold film may occur if some residual material remained after the decomposition of the RuPc complex, leading to a less continuous film than if only the gold remained.

Simultaneous TGA/DSC was utilised to probe the changes occurring upon heating for both the RuPc complex and the RuPc-AuNP nanocomposite. The TGA/DSC data for the RuPc complex are displayed in Figure 4.8. A relatively small exothermic event can be seen at 337 °C with a mass loss of ~35%, which corresponds to the removal of the two axial pyridyl ligands, a technique used by synthetic chemists to prepare four-coordinate RuPc.[135] This event was followed by a larger exothermic reaction at 365 °C, and a total of 85% of the original mass was lost by 400 °C. This mass loss is assigned to the combustion of the remaining organic component of the complex, the Pc macrocycle. The remaining mass (~15%) corresponds to the mass of RuO_2, formed during the combustion of the macrocycle, with the oxygen atoms scavenged from the TGA atmosphere of air. The TGA data for temperatures between 500 °C and 1300 °C are consistent with the reported data for RuO_2 at these temperatures,[142,143] with a gradual mass loss around 1200 °C with <2% mass remaining by 1300 °C.

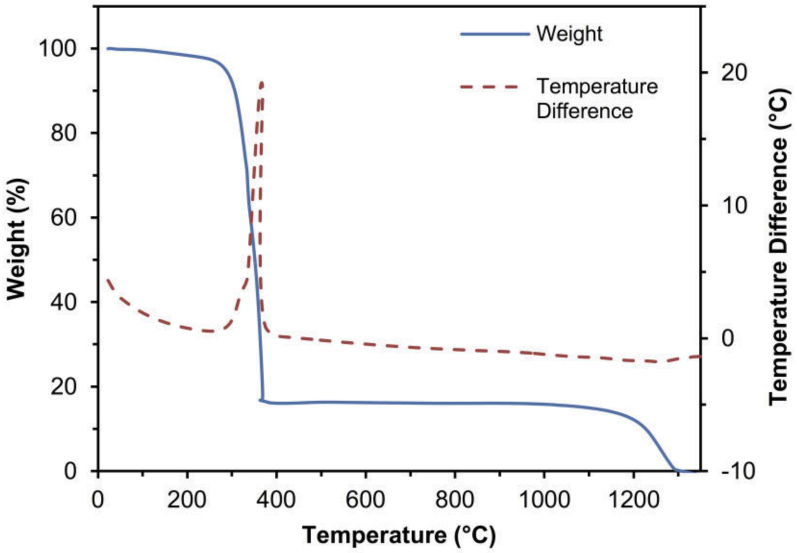

Figure 4.8. TGA/DSC data for [RuPc(4-py(CH_2)$_3$SAc)(4-py^{t}Bu)], heated at 10 °C min^{-1} in air.

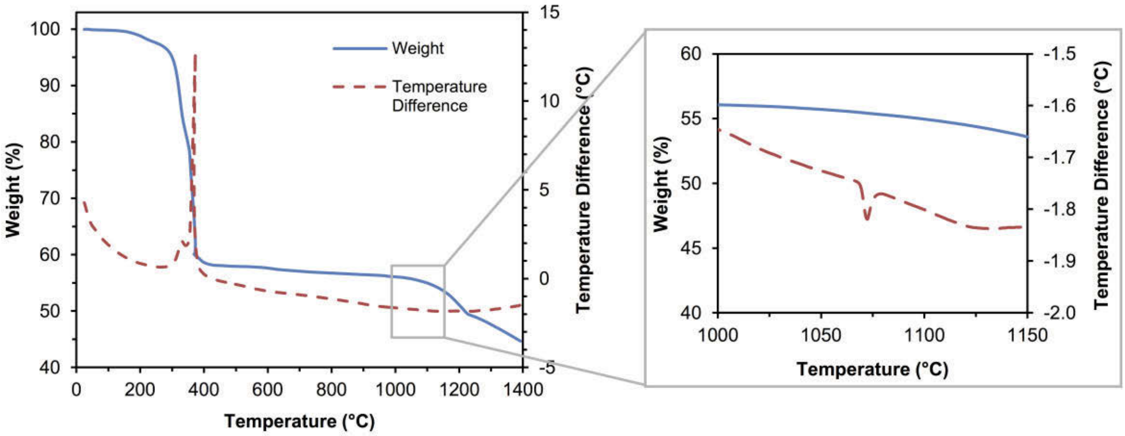

Figure 4.9. TGA/DSC data for RuPc-AuNPs, heated at 10 °C min^{-1} in air, and the endotherm corresponding to the melting point of gold (inset).

The TGA/DSC data for the RuPc-AuNP nanocomposite (Figure 4.9) display a very similar trend to that of the pure RuPc complex. Exothermic peaks are observed at 330 °C and 373 °C, accompanied by the main mass loss events. These temperatures correlate closely with the T_{SE} of the nanocomposite observed in Figure 4.7. The total mass loss up to 1300 °C is 53%, as the gold from the AuNPs is left behind. The small endothermic event in the DSC data at ~1070 °C corresponds to the melting point of gold (1064 °C). From the data in Figures 4.8 and 4.9, it is concluded that the thermal stability of the RuPc complex is directly responsible for the high stability of the RuPc-AuNP nanocomposite. The presence of RuO_2 after the decomposition of the RuPc also explains the higher resistance measured for the sintered nanocomposite films, compared to the sintered BT@AuNP films.

The ratio of RuPc molecules per AuNP can also be determined from the TGA data. Assuming the nanoparticles are spherical and on average 5 nm in diameter, each AuNP is calculated (using the density of bulk gold) to have a mass of 1.26×10^{-18} g. The RuPc complex [RuPc(4-py(CH_2)$_3$SAc)(4-py^{t}Bu)] has a molecular mass of 1.57×10^{-21} g/molecule. The 53% mass loss measured by TGA (and assigned to the RuPc complex) therefore corresponds to 1.42×10^{-18} g of RuPc complex per AuNP, or an average of ~900 RuPc molecules per nanoparticle (molecules/NP). This value is significantly greater than the number of RuPc molecules that could form a surface-bound monolayer based on geometric considerations (~70, based on an area of ~2.25 nm^2/molecule with no overlap of Pc rings), although this is not unexpected given the propensity of Pc molecules to form aggregates.[144] Importantly though, this abundance of RuPc molecules indicates that prior to heating, the AuNPs within the nanocomposite are well separated by an effective barrier of thermally stable molecules. In comparison, the TGA data for BT@AuNPs (Figure 4.10) show a mass loss of ~11%, corresponding to the loss of the 1-butanethiol molecules, which indicates a coverage of ~230 molecules/NP, assuming spherical 3 nm AuNPs with a mass of 2.73×10^{-19} g/NP.

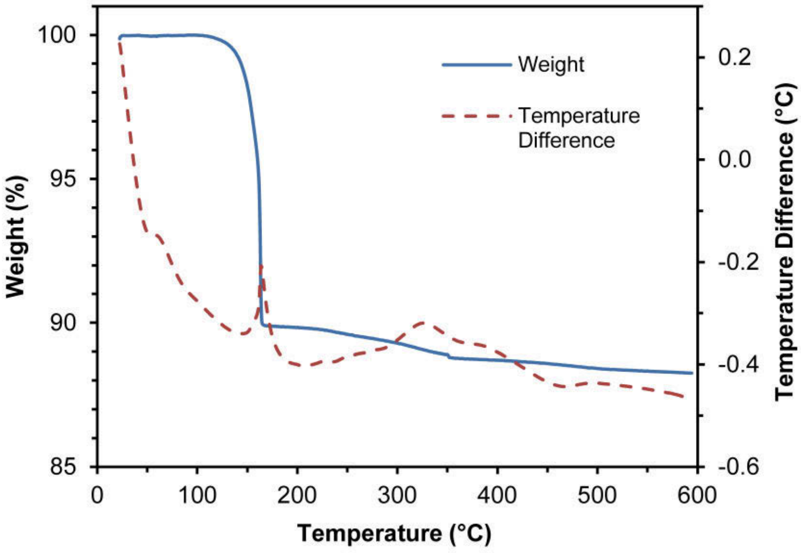

Figure 4.10. TGA/DSC data for BT@AuNPs, heated at 10 °C min^{-1} in air.

4.2.3. Characterisation of Sintered Films

The structure of a sintered film of RuPc-AuNPs was analysed by SEM (Figure 4.11). As expected, the AuNPs have aggregated, however the presence of the residual oxidised ruthenium has prevented the gold from forming a more continuous (and thus conductive) film, such as those of sintered BT@AuNPs (Figure 4.12). The residual material can be seen in Figure 4.11 b as a darker grey matrix surrounding the light grey aggregates of gold (the much darker regions are the bare silicon substrate).

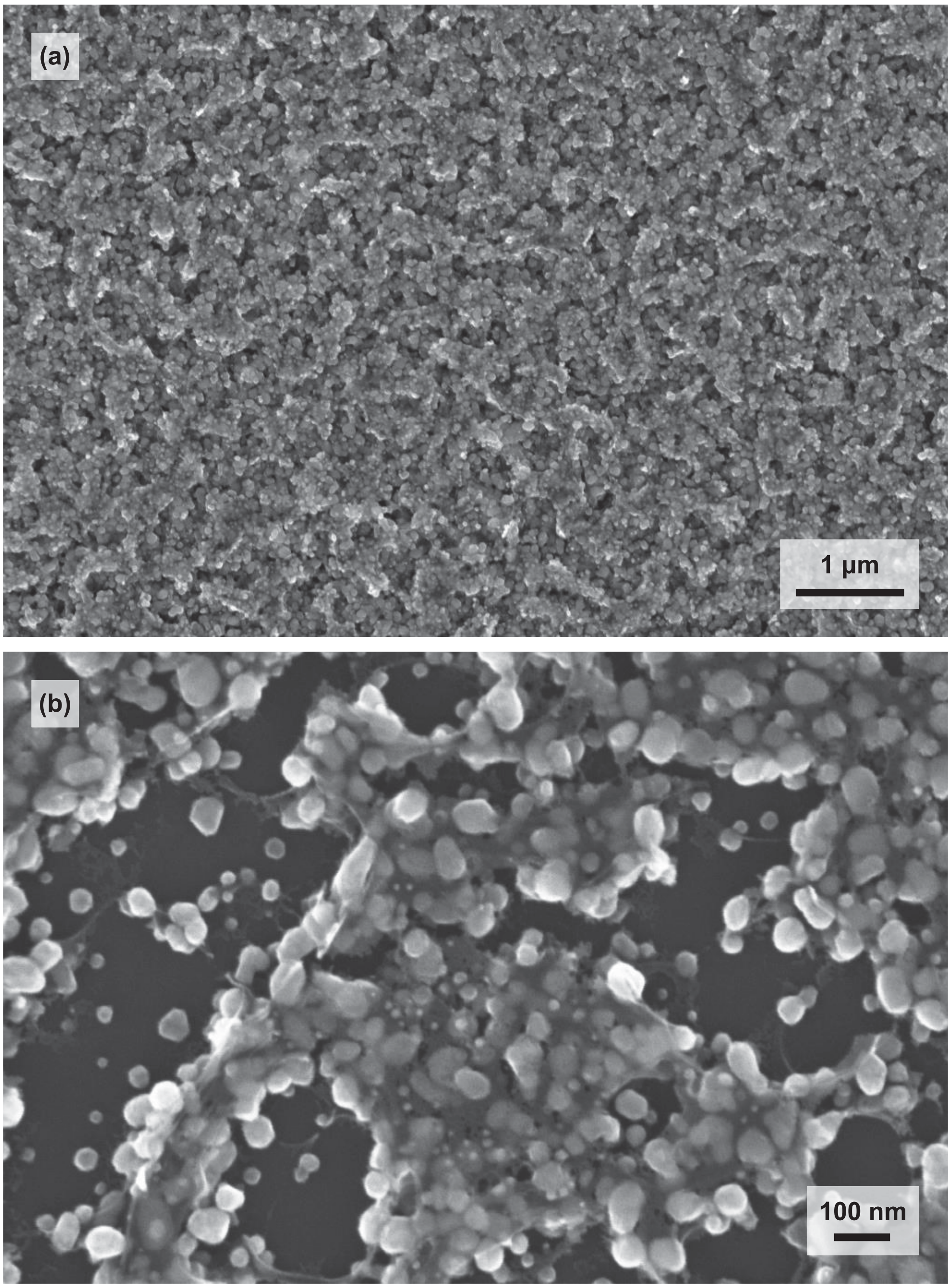

Figure 4.11. SEM images of a sintered film of RuPc-AuNPs, after being heated to 350 °C.

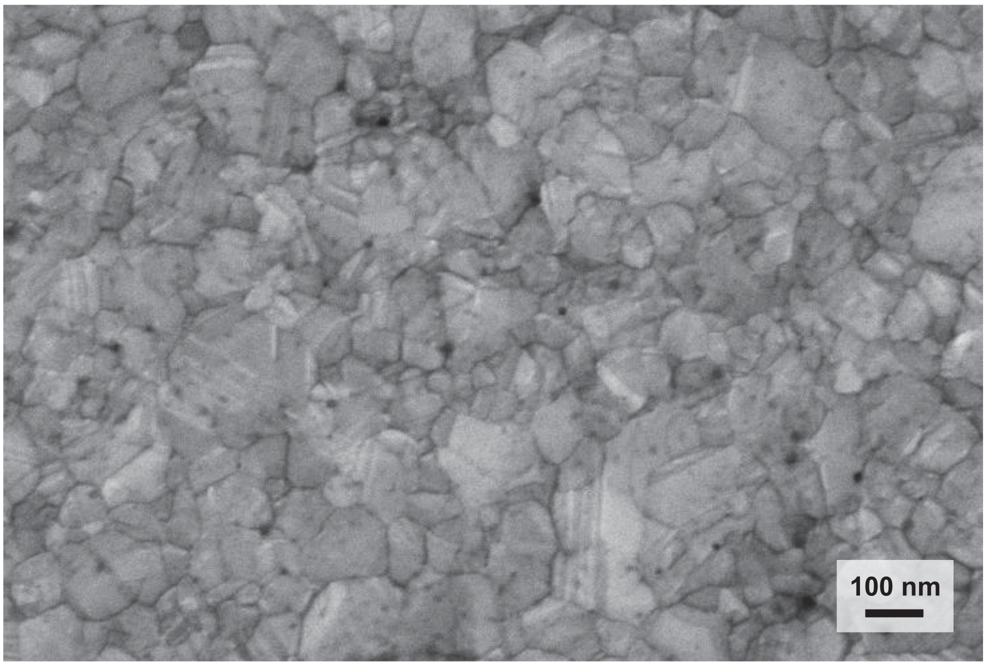

Figure 4.12. SEM image of a sintered film of gold, formed by heating BT@AuNPs to 200 °C.

Table 4.2. Atomic ratio of elements in various regions of a sintered film of RuPc-AuNPs.

Spectrum	Au : Ru	S : Ru	O : Ru	C : Au
1	3.3	0.0	12	5.5
2	4.5	0.0	11	3.9
3	2.3	0.031	2.3	0.38
4	2.2	0.0	6.5	2.9
5	8.8	0.0	3.5	0.42
6	4.6	0.0	5.1	1.1
7	3.6	0.016	3.8	0.84
8	3.6	0.0	7.5	2.6
9	2.8	0.038	3.1	0.54
10	10.7	0.0	7.9	1.3
11	1.9	0.029	3.2	0.88
Average	4.4	0.010	6.0	1.9

Elemental analysis by EDS was performed on a sintered film of RuPc-AuNP (Table 4.2). The average ratio of gold to ruthenium was virtually unchanged after heating, supporting the interpretations of the TGA and SEM data. The average ratio of oxygen to ruthenium also remained the same after heating, although little can be said from this result about the oxidation of the ruthenium due to the presence of oxygen in the sample from other sources, as seen in the EDS measurements of the unheated sample (Table 4.1). Meanwhile, the amounts of sulfur, carbon and nitrogen decreased dramatically after heating, with most of the sampled areas showing no detectable levels of sulfur at all, as expected from the combustion of the RuPc complex.

LA-ICP-MS, performed by Mr Mika Westerhausen (UTS), was used as a second technique for quantifying and mapping selected elements in the RuPc-AuNP films before and after sintering. Prior to sintering, the elemental maps show colocalisation of ruthenium and sulfur (Figure 4.13 a). After sintering, the ablated region of the sample contained no detectable sulfur, while significant quantities of gold and ruthenium remained (Figure 4.13 b), findings that are consistent with the EDS results.

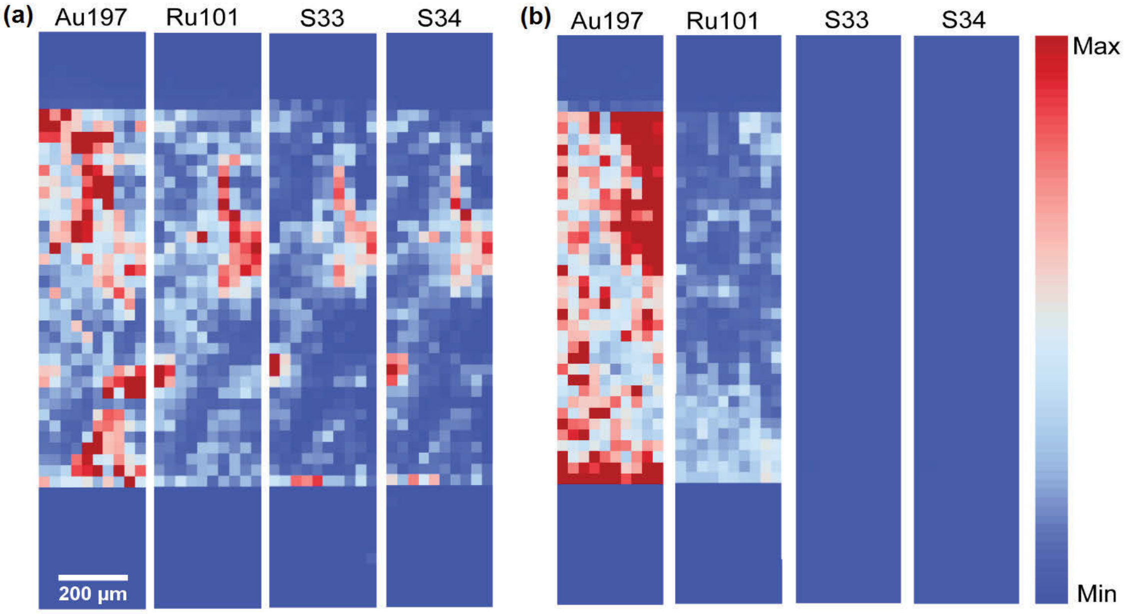

Figure 4.13. LA-ICP-MS maps of RuPc-AuNPs (a) before, and (b) after sintering, with the intensities normalised to Au197.

In summary, the results presented in this section show that a nanocomposite composed of AuNPs and a RuPc complex possesses high thermal stability, wherein the AuNPs are resistant to sintering at temperatures up to 330 °C. The RuPc complex acts as a robust physical barrier between the AuNPs, such that sintering only occurs upon the decomposition of the stabilising complex. However, the ruthenium from the RuPc complex remains after the combustion of the organic components of the complex, with the result that the gold can only form a moderately conductive film when sintered.

4.3. Gold Nanoparticles Functionalised with [RuPc(4-pyCH$_2$SAc)$_2$]

The RuPc complex [RuPc(4-pyCH$_2$SAc)$_2$], which has thioacetate groups on both axial ligands, was tested as a stabiliser for AuNPs. A large excess of [RuPc(4-pyCH$_2$SAc)$_2$] was used as a strategy to minimise aggregation of the AuNPs; however even with a large excess of the complex, significant aggregation of the AuNPs occurred. A precipitate formed after functionalising AuNPs with the RuPc complex, which SEM imaging showed to be composed of both irregular, micron-sized agglomerates of AuNPs and smaller (~60 nm) quasi-spherical agglomerates, resembling clusters of snowballs (Figure 4.14).

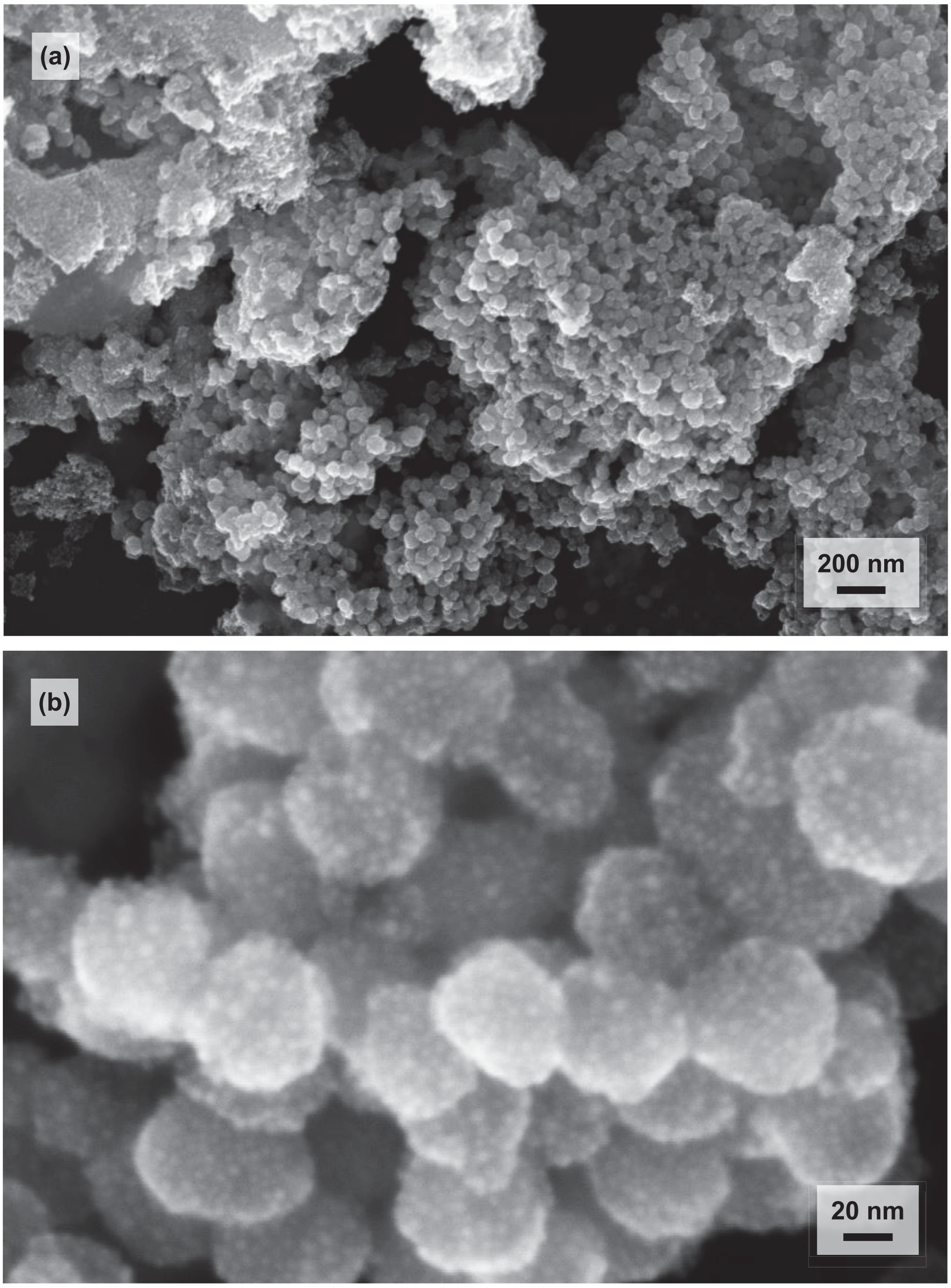

Figure 4.14. SEM images of "snowballs" of AuNPs functionalised with [RuPc(4-pyCH_2SAc)$_2$].

The complex [RuPc(4-pyCH_2SAc)$_2$] has sulfur groups on both ends of the molecule and so it is able to bind to two different AuNPs at once (Figure 4.15), which can cause the AuNPs to aggregate into an interconnected network of particles. It was hypothesised that using a large excess of RuPc molecules to functionalise the particles would prevent this aggregation by completely coating each particle with its own molecules, such that there would be no space remaining for a molecule from a neighbouring particle to also attach. However, the results showed this technique to be insufficient for preventing such aggregation.

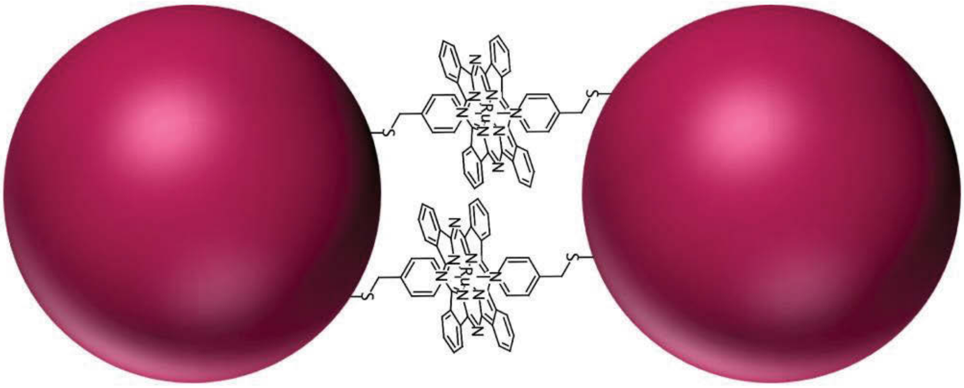

Figure 4.15. Schematic diagram of [RuPc(4-pyCH$_2$SAc)$_2$] molecules binding two AuNPs together.

Since the AuNPs functionalised with [RuPc(4-pyCH$_2$SAc)$_2$] formed an insoluble precipitate, they were not used in further sintering experiments.

4.4 Influence of Bound versus Non-Bound Stabilising Molecules on the Thermal Stability of Gold Nanoparticles

Having determined in the first part of this study that [RuPc(4-py(CH$_2$)$_3$SAc)(4-py^{t}Bu)] can stabilise AuNPs against sintering due to the complex's own high thermal stability, a range of other compounds were tested for their ability to increase the thermal stability of AuNPs. Furthermore, as explained in the introduction to this chapter, several compounds with and without functional groups to anchor the molecules to the gold surface were compared to test the necessity of binding the stabilising compounds to the AuNPs.

In addition to their thermal stability, an important consideration when choosing stabilising compounds is their solubility, ensuring the compounds and the AuNPs can be dissolved in the same solvents. The stabilisers with anchoring groups were attached to AuNPs via ligand exchange reactions with OA@AuNPs. The stabilisers without anchoring groups were mixed with BT@AuNPs, which have low thermal stability and are of a similar size to the OA@AuNPs. Since both OA@AuNPs and BT@AuNPs are soluble in organic solvents such as toluene, chloroform, DCM and THF, potential stabilising compounds were chosen that are also soluble in these solvents. The selected stabilisers are listed in Table 4.3, and the structures of some of these are shown in Figure 4.16.

Table 4.3. List of thiolated and non-thiolated stabilising compounds used in this study.

Thiol-containing stabilising ligands	Stabilisers without thiol groups
1-Octanethiol (OT)	
1-Dodecanethiol (DDT)	Dodecane (DD)
1-Hexadecanethiol (HDT)	Hexadecane (HD)
[RuPc(4-py(CH$_2$)$_3$SAc)(4-py^{t}Bu)]	[RuPc(4-py^{t}Bu)$_2$]
1-Pyrenebutanethiol (PyBuSH)	1-Pyrenebutanol (PyBuOH)
	Oleylamine (OA)
	Hexaphenylbenzene (HPB)
	Hexabenzocoronene derivative (HBC-acetylene)
	N,N′-Dioleyl-3,4,9,10-perylenedicarboximide (DPDI)

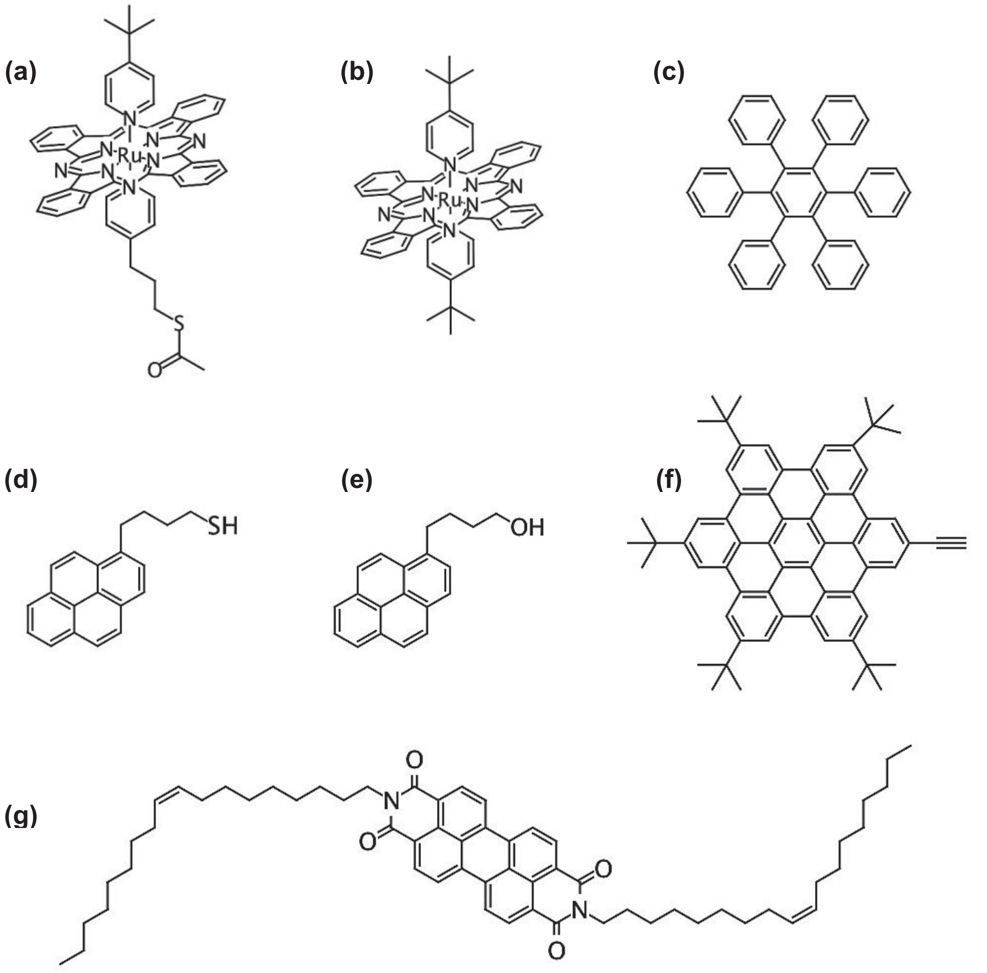

Figure 4.16. Structures of (a) [RuPc(4-py(CH$_2$)$_3$SAc)(4-py^{t}Bu)], (b) [RuPc(4-py^{t}Bu)$_2$], (c) HPB, (d) PyBuSH, (e) PyBuOH, (f) HBC-acetylene, and (g) DPDI.

4.4.1. Thermal Behaviour of Potential Stabilising Compounds

The thermal behaviour of the selected compounds was characterised using TGA/DSC. All of the alkanes and alkanethiols (Figure 4.17) evaporated (evidenced by sharp endotherms in the DSC data) at temperatures 35–75 °C below their reported boiling points, which can be attributed to their volatility and the small volumes used (~12 µL). Octane evaporated at a temperature ~70 °C below the T_{SE} of BT@AuNPs, so it was eliminated as a potential stabiliser.

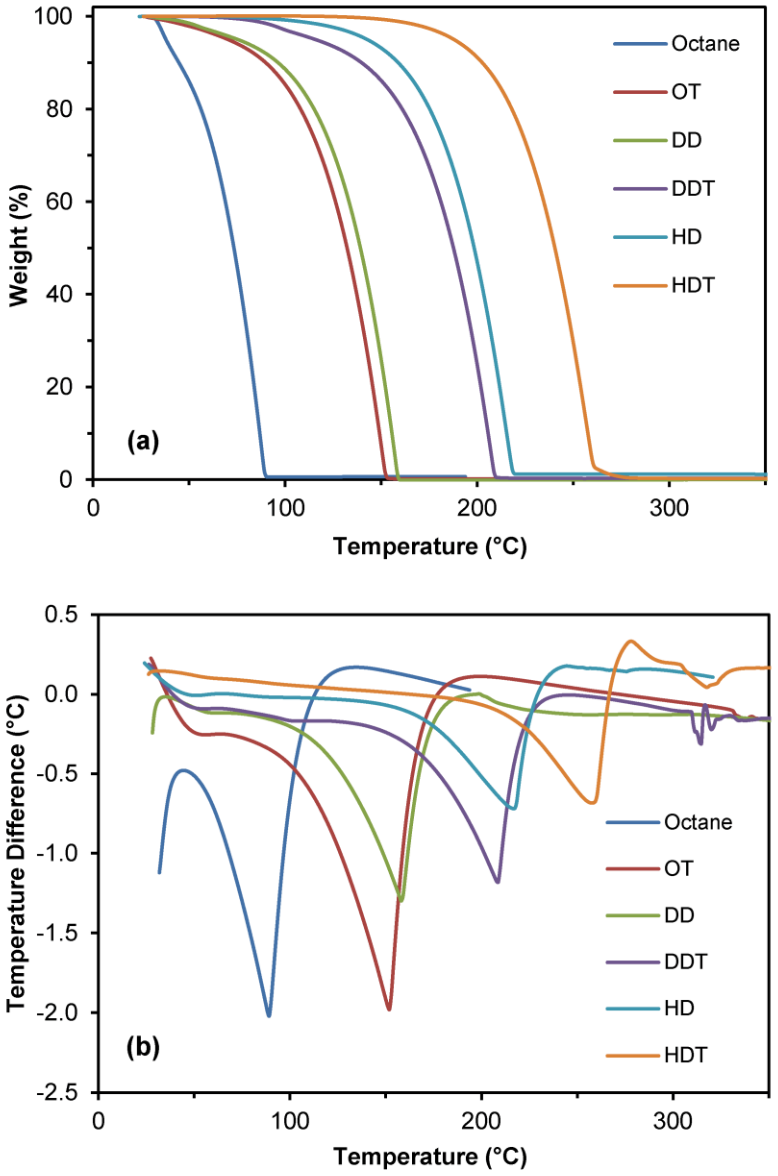

Figure 4.17. Graphs of (a) TGA and (b) DSC data collected simultaneously for alkanes and alkanethiols, heated in air at 10 °C min^{-1}.

The TGA/DSC results for the other selected stabilisers, with the exceptions of [RuPc(4-py(CH$_2$)$_3$SAc)(4-py^{t}Bu)] (Figure 4.8) and oleylamine (Figure 4.19), are shown in Figure 4.18. The TGA data reveal two or more mass loss events for each of these compounds, apart from

HPB (Figure 4.18 e), with accompanying exothermic peaks in the DSC data, indicating that most of these compounds undergo combustion in stages. The thermal behaviour of [RuPc(4-py^{t}Bu)$_2$] (Figure 4.18 c) is very similar to that of [RuPc(4-py(CH$_2$)$_3$SAc)(4-py^{t}Bu)] (Figure 4.8), with a combustion product of RuO$_2$ remaining until >1200 °C.

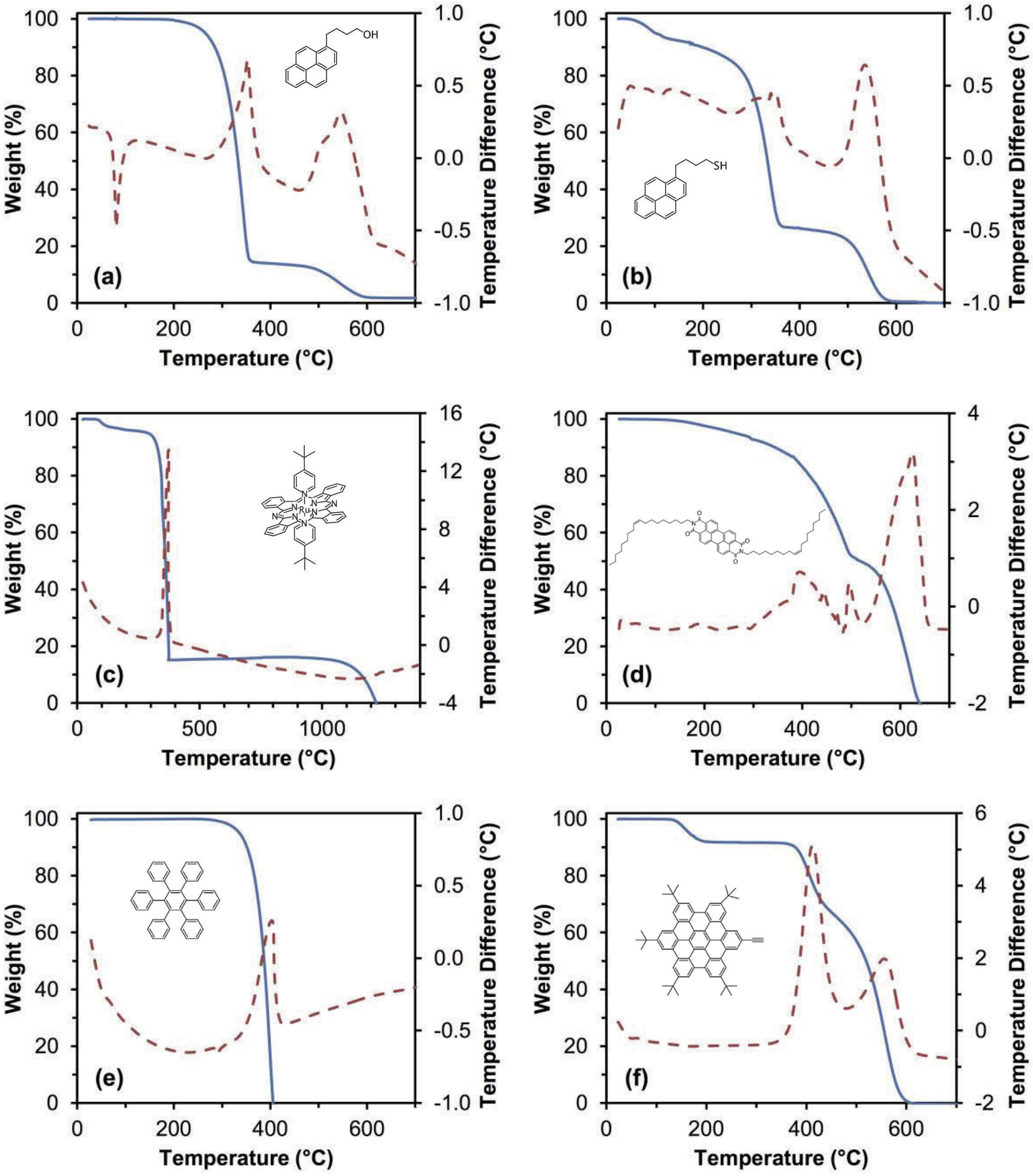

Figure 4.18. TGA/DSC data for (a) PyBuOH, (b) PyBuSH, (c) [RuPc(4-py^{t}Bu)$_2$], (d) DPDI, (e) HPB and (f) HBC-acetylene, heated at 10 °C min^{-1} in air. The solid blue curves show the weight (TGA) and the dashed red curves show the temperature difference (DSC).

The thermal behaviour of oleylamine was examined in more detail: performing TGA/DSC in atmospheres of air and nitrogen (Figure 4.19), and comparing the results to TGA/DSC data for octadecylamine, which only differs from oleylamine by a single instead of a double bond between the 9th and 10th carbon atoms. Under nitrogen, the thermal behaviour of oleylamine resembles that of the alkanes and alkanethiols (Figure 4.17), evaporating entirely by 258 °C. However, when the TGA/DSC is performed in air, the mass is lost in several stages, with material remaining up to ~600 °C, and exotherms accompanying the mass loss events. The results of the TGA/DSC, performed in air, for octadecylamine (data not shown) were almost identical to those of oleylamine in air, with the addition of a melting endotherm at 56.5 °C (oleylamine is a liquid at room temperature, while octadecylamine is solid). This similarity in results eliminates the double bond present in oleylamine as the site of any reaction (such as polymerisation) responsible for the continued presence of material above 258 °C.

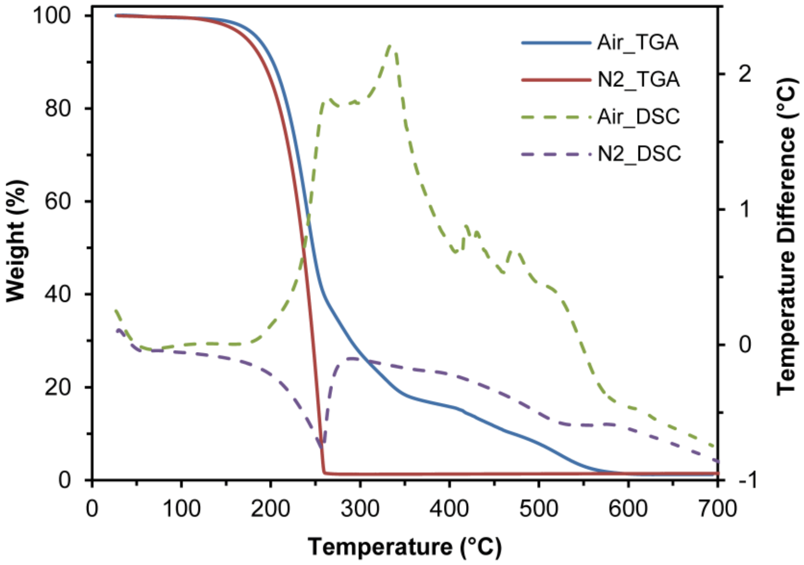

Figure 4.19. TGA/DSC data for oleylamine heated at 10 °C min^{-1}, in air (blue and green curves) and in nitrogen (red and purple curves).

Descriptions of the thermal decomposition products of oleylamine in air could not be found in the literature, however some studies have been done on the decomposition of a somewhat similar compound, cetyltrimethylammonium bromide (CTAB, $CH_3(CH_2)_{15}N(Br)(CH_3)_3$) within mesoporous silica materials.[145–147] These studies suggest the ammonium head-group is first removed in a Hofmann degradation process, followed by exothermic fragmentation or cracking of the remaining hydrocarbon chain. One of the studies showed material remaining up to 600 °C,[146] with an overall TGA curve resembling the one obtained for oleylamine in air (Figure 4.19).

4.4.2. Effects of Stabilising Compounds on the Thermal Stability of AuNPs

The T_{SE} data for AuNPs stabilised with alkanethiols of various chain lengths, presented in Figure 4.20, demonstrate the effect of increasing T_{SE} with increasing chain length, which is in agreement with previous reports.[20,29,31]

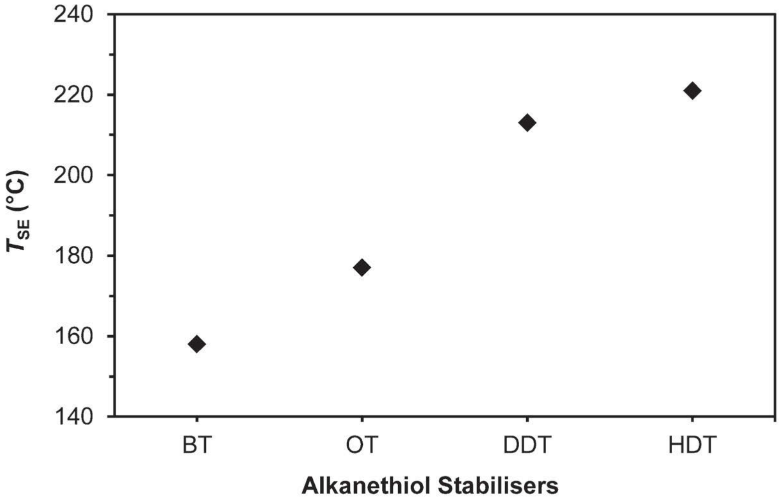

Figure 4.20. Graph of T_{SE} data for alkanethiol-stabilised AuNPs.

TGA for PyBuSH (Figure 4.18 b) shows one mass loss event at ~340 °C, leaving 26% of the original mass until a second mass loss event at ~540 °C. The AuNPs functionalised with PyBuSH (Py@AuNPs) were found to be even more resistant to sintering than RuPc-AuNPs, with a T_{SE} of 390 °C, compared to 323 °C for RuPc-AuNPs, despite both stabilisers showing decomposition around 350 °C in the TGA (Figure 4.18). This difference in T_{SE} may be due to the extremely exothermic nature of the RuPc decomposition, seen in the DSC data in Figure 4.18 c, which could cause sufficient localised heating within the film to sinter the AuNPs at a lower recorded temperature than the Py@AuNPs.

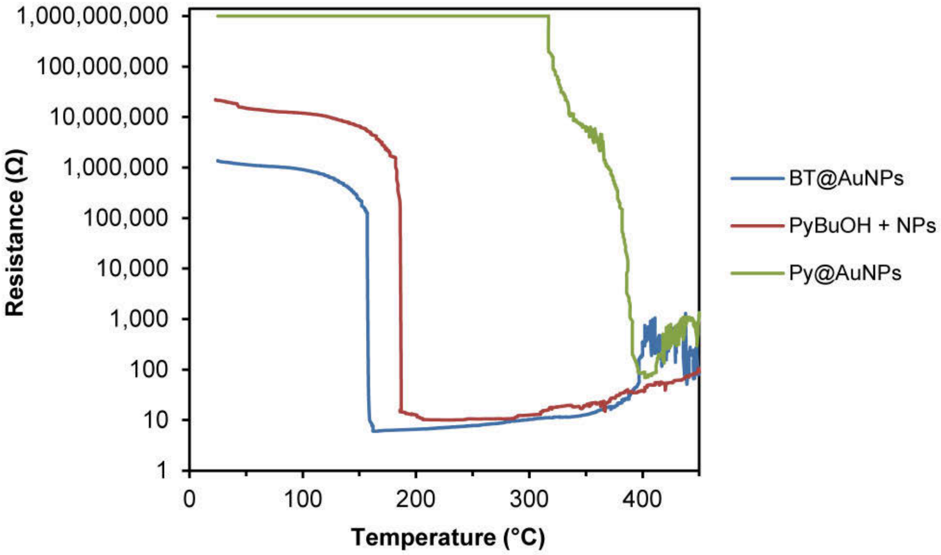

Figure 4.21. Raw data for measurements of resistance as a function of temperature for BT@AuNPs, BT@AuNPs + PyBuOH at 1000 molecules/NP, and Py@AuNPs, heated at 10 °C min^{-1} in air.

To test the effectiveness of the pyrene stabiliser when it is not bound to the AuNPs, the analogous compound PyBuOH, which has no gold binding groups but displays very similar thermal behaviour to PyBuSH (Figure 4.18 a), was mixed with BT@AuNPs at varying ratios of molecules to nanoparticles, and the mixtures were sintered. The ratios tested (500, 1000, 2000 and 5000 molecules/NP) all produced T_{SE} values in the range 178–197 °C, which is a 20–40 °C increase over the BT@AuNPs without added PyBuOH, but is far lower than the 390 °C T_{SE} obtained with the bound stabiliser. The resistance versus temperature data for BT@AuNPs, BT@AuNPs + PyBuOH (1000 molecules/NP) and Py@AuNPs are shown in Figure 4.21. In addition to increasing the thermal stability of the AuNPs, the PyBuOH and PyBuSH stabilisers also increased the initial electrical resistance of the films. The mixtures of AuNPs and PyBuOH displayed a trend of increased initial resistance with increasing ratio of molecules to particles, while the initial film resistance of Py@AuNPs was above the instrument's maximum reading of 200 MΩ until the initial stages of sintering began at ~320 °C.[i]

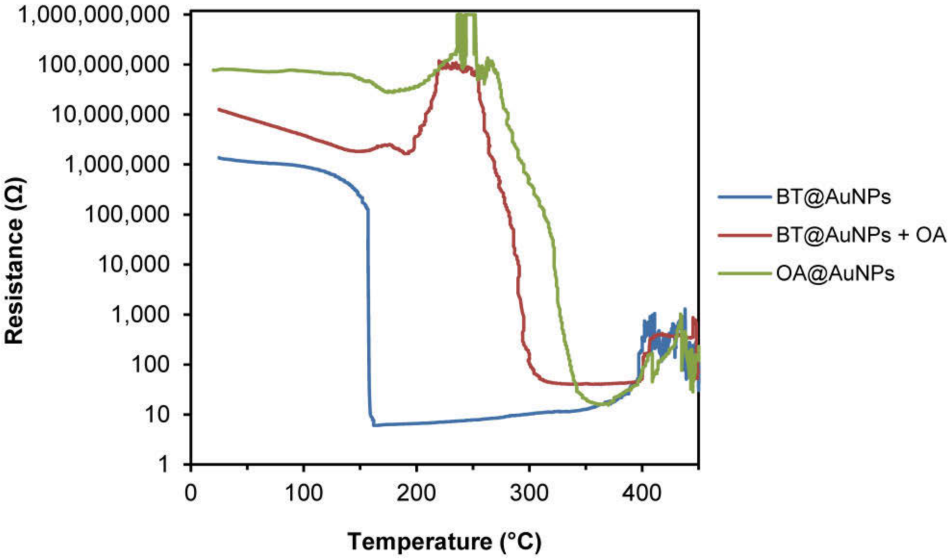

Figure 4.22. Raw data for measurements of resistance as a function of temperature for BT@AuNPs, BT@AuNPs + OA at 50 molecules/NP, and OA@AuNPs, heated at 10 °C min^{-1} in air.

Oleylamine was initially utilised as a stabiliser for synthetic purposes (to be exchanged for various thiols) but the thermal stability of OA@AuNPs was found to be surprisingly high (T_{SE} = 323 °C). Unlike the thiol-stabilised AuNPs, which sinter very rapidly, the resistance of the OA@AuNP film decreased more gradually, over a temperature range of ~80 °C (Figure 4.22). Oleylamine was also tested as an unbound stabiliser by mixing it with BT@AuNPs. It is reasoned that the amine group would not bind to the AuNPs since the particles were already functionalised with 1-butanethiol, which forms a much stronger bond with the gold (although it cannot be discounted that some nitrogen-gold attraction could take place). The addition of as

---

[i] The LabVIEW software recorded any off-the-scale resistance measurement as the next highest power of 10, in this case 1 GΩ.

little as 50 molecules/NP of oleylamine raised the T_{SE} of BT@AuNPs to 290 °C, an increase of over 130 °C (Figure 4.22). The data also showed a significant increase in resistance between 200 and 250 °C for each of the BT@AuNPs + OA mixtures tested, as well as for OA@AuNPs, before falling to 'conductive' levels upon sintering. The cause of this increase is unknown, though it may be related to the residual combustion products observed in the TGA data (Figure 4.19).

Table 4.4 lists the T_{SE} values for all the pairs of bound and analogous unbound stabilisers tested, where the unbound stabilisers are mixed with BT@AuNPs in a ratio of 500 molecules/NP. The additions of DD and HD produced no increase in thermal stability compared to BT@AuNPs alone. Moderate increases were observed for particles mixed with PyBuOH or [RuPc(4-py^{t}Bu)$_2$], while their bound counterparts were far more effective in stabilising the AuNPs. Oleylamine was the only stabiliser found to greatly increase the thermal stability in both bound and unbound forms, though the bound form was still more effective by ~40 °C.

Table 4.4. T_{SE} data for AuNPs with bound and unbound stabilising compounds. All unbound stabilisers are mixed with BT@AuNPs (T_{SE} = 158 °C) at a ratio of ~500 molecules/NP. RuPcSAc = [RuPc(4-py(CH$_2$)$_3$SAc)(4-py^{t}Bu)] and RuPc = [RuPc(4-py^{t}Bu)$_2$].

Bound Stabiliser	T_{SE} (°C)	Unbound Stabiliser	T_{SE} (°C)
DDT	213	DD	145
HDT	221	HD	154
OA*	323	OA*	279
PyBuSH	390	PyBuOH	197
RuPcSAc	323	RuPc	175

* Bound OA = OA@AuNPs, while unbound OA is mixed with BT@AuNPs.

To determine if the T_{SE} for the mixtures of unbound stabilisers and BT@AuNPs is dependent on the ratio of molecules/NP, particularly since the molecules vary widely in their molecular masses, a range of ratios was tested for each of the unbound stabilisers. The results are plotted in Figure 4.23. For most of the compounds, it was found that the T_{SE} was almost entirely independent of the amount of stabiliser added. With the compound PyBuOH, as mentioned previously, ratios as high as 2000 and 5000 molecules/NP yielded effectively the same T_{SE} as with lower ratios. DPDI displayed by far the greatest increase in thermal stability of all the stabilisers tested, including those that were bound to the AuNPs, with sintering not occurring until ~540 °C in some samples, which is unprecedented for ligand-stabilised AuNPs. This stabiliser also showed some dependence on the ratio of molecules to particles with a threshold ratio of ~300 molecules/NP, below which the samples sintered at temperatures similar to the T_{SE}

of BT@AuNPs. It was observed during experimentation that the samples containing 100 and 250 molecules/NP did not change colour from dark red to gold until ~450 °C, despite becoming electrically conductive at 150 and 180 °C, respectively. Generally during sintering, AuNP samples become conductive and change colour to lustrous gold simultaneously. It was also observed that use of the waxy DPDI stabiliser resulted in very thick films when deposited on the substrates, particularly in the samples containing >250 molecules/NP. Heating these samples led to cracks forming throughout the deposited film, reducing contact between the two electrodes and resulting in a measured final resistance in the low kΩ range (Figure 4.24), in contrast to sintered gold resistances on the order of 10 Ω for the other stabilisers used. This issue may have been resolved if the DPDI stabiliser had a thiol functional group at one end to anchor it to the gold, possibly allowing the AuNPs to be stabilised to high temperatures using fewer molecules per particle and thereby reducing the thickness of the deposited films; however synthesising such a compound was unfortunately beyond the scope of this project.[148]

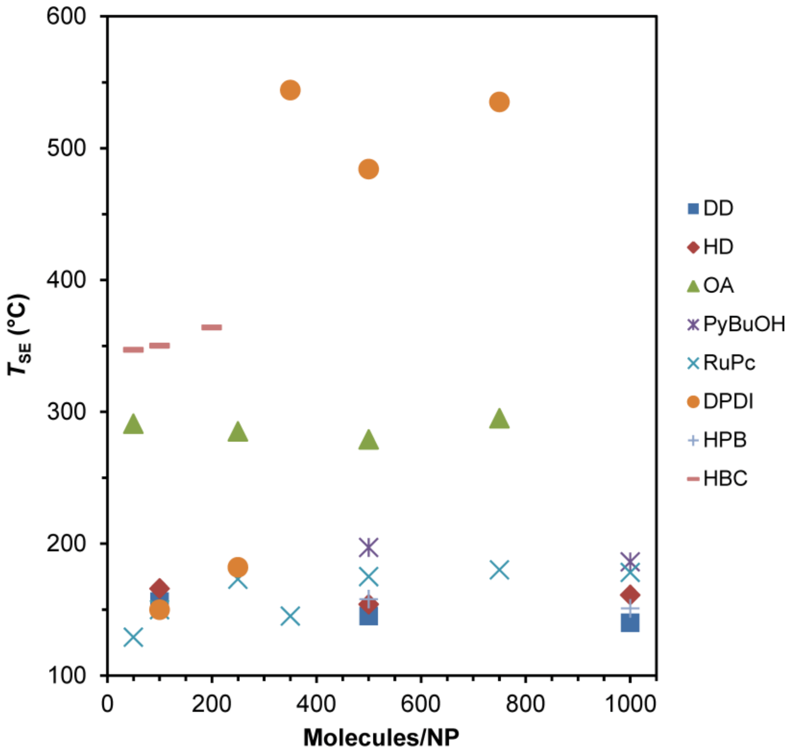

Figure 4.23. Graph of T_{SE} data for BT@AuNPs mixed with non-thiolated stabilisers for a range of ratios of molecules/NP. RuPc = [RuPc(4-py^{t}Bu)$_2$] and HBC = HBC-acetylene.

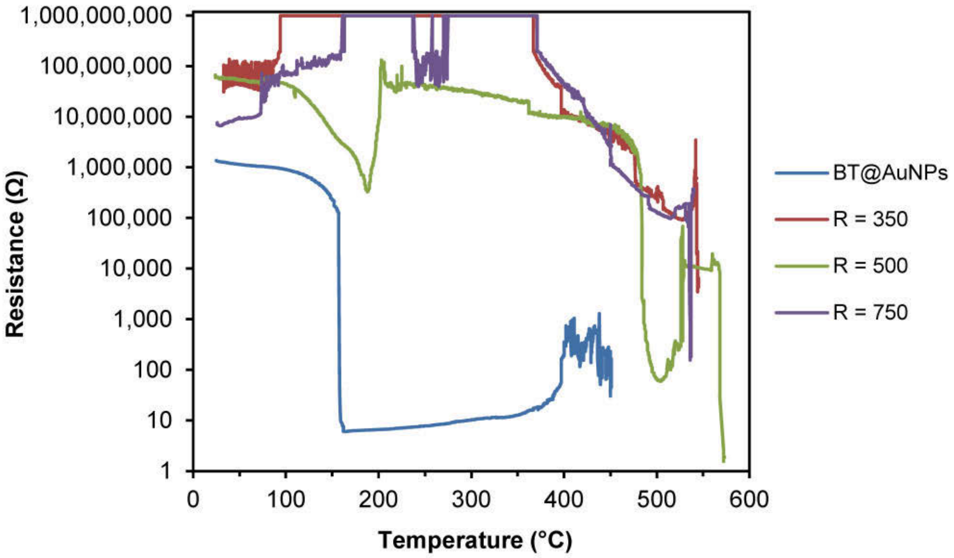

Figure 4.24. Raw data for measurements of resistance as a function of temperature for BT@AuNPs and BT@AuNPs + DPDI at ratios of 350, 500 and 750 molecules/NP, heated at 10 °C min^{-1} in air.

The HBC-acetylene stabiliser was the second most effective unbound stabiliser, with T_{SE} values in the range 345–365 °C for ratios between 50 and 200 molecules/NP (Figure 4.23). A sample at 500 molecules/NP never became electrically conductive, possibly because the AuNPs within the mixture were too far apart to be able to form an electrically percolating film after the stabiliser had decomposed. As such, the T_{SE} for that sample could not be determined, and samples with lower ratios of molecules/NP were prepared. The T_{SE} values obtained using HBC-acetylene as stabiliser, while notably high, were not as high as anticipated based on the TGA results for the stabiliser (Figure 4.18 f), which showed material remaining until 600 °C, similar to DPDI. It was also observed that solutions of HBC-acetylene in THF changed colour from yellow to orange when left overnight (the compound is only sparingly soluble in chloroform and toluene, but dissolves well in THF). The spectra from UV-visible analysis of a freshly prepared HBC-acetylene solution and an older solution that had turned orange are shown in Figure 4.25. The spectrum of the older solution shows increases in absorption in the ranges 250–340 nm and 420–580 nm compared to that of the fresh solution, as well as decreases in the intensity of the three peaks at 345, 362 and 392 nm. Due to these changes, which indicate reaction and/or aggregation of the HBC material, and the reasonably complex synthetic processes involved in preparing analogues, this class of material was not pursued further in these studies.

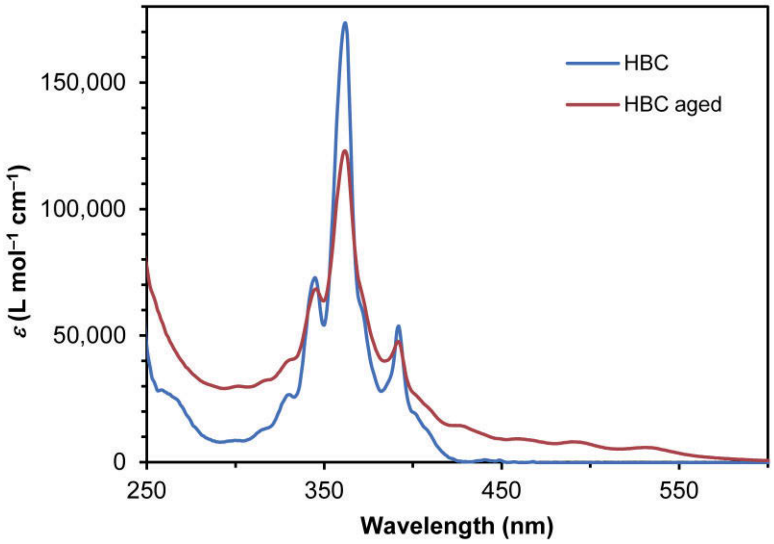

Figure 4.25. UV-visible spectra of HBC-acetylene solutions in THF freshly prepared and after being left overnight.

The compound HPB is similar to HBC-acetylene in structure (Figure 4.16 c and f) and is stable up to 400 °C (Figure 4.18 e). Although HPB is soluble in THF, the powder required sonication for a few minutes for it to fully dissolve in THF, unlike BT@AuNPs, which dissolve almost instantly (HPB is insoluble in chloroform and DCM). Mixtures of HPB and BT@AuNPs sintered at 150–160 °C (Figure 4.23), the same as BT@AuNPs without any added compounds. This may be explained considering the much lower solubility of HPB compared to BT@AuNPs in THF, which can lead to phase separation of the particles and molecules as the deposited mixture dries on the substrate, such that the molecules are not dispersed between the particles and thus cannot act as a barrier towards sintering.

The electrical resistance of the unbound stabilisers (excluding those that are liquid at room temperature) were measured during heating (Figure 4.26) to assess their contribution to the measured conductivity of the AuNP mixtures. The resistance of a blank substrate (with gold electrodes) was also measured. Most of the compounds had recorded resistances of 10–100 MΩ throughout the heating experiments, as did the blank substrate. This measureable resistance of the blank substrate suggests there may be some small leakage of current from the gold electrodes through the silicon oxide layer, though with the resistance being above 10 MΩ this would still be considered to be insulating. The RuPc complex [RuPc(4-py^{t}Bu)$_2$] displayed a drop in resistance to ~25 kΩ at 300 °C, which slowly increased to ~1.7 MΩ by 335 °C before sharply returning to its initial resistance range of ~50–100 MΩ. This decrease in resistance occurred around the onset of decomposition of the RuPc complex (Figure 4.18 c), suggesting the compound temporarily forms somewhat conductive by-products as it breaks down. The compound PyBuOH displayed a consistent off-the-scale resistance reading through the entire heating range, similar to the Py@AuNPs prior to sintering (Figure 4.21). It is unknown how the compound can have a recorded resistance that is higher than the blank substrate. Above 550 °C, near the upper temperature limit of the heating block, the blank substrate experienced a decrease in resistance to ~100 kΩ, before sharply rising to >100 MΩ. This behaviour implies the experimental setup is unable to give reliable measurements above ~500 °C, though fortunately most of the AuNP mixtures sintered below this temperature. The resistance of the blank substrate was also recorded as it cooled to <100 °C, and the measurements were consistently above the instrument's limit of 200 MΩ (data not shown). The DPDI and HBC-acetylene compounds also displayed sharp drops in resistance at 554 and 595 °C, respectively, which is near their decomposition temperatures (Figure 4.18); however, unlike the RuPc complex, the resistance did not increase again after decomposition of the compounds, but remained below 10 kΩ. Since these compounds are composed of multiple aromatic rings, it is possible that the decomposition products contain semi-conductive forms of carbon such as graphite, leading to the drops in resistance seen at their decomposition temperatures. Overall, the unbound stabilisers and blank substrate had very high electrical resistances and therefore have little influence on the measured conductivity of the AuNP mixtures.

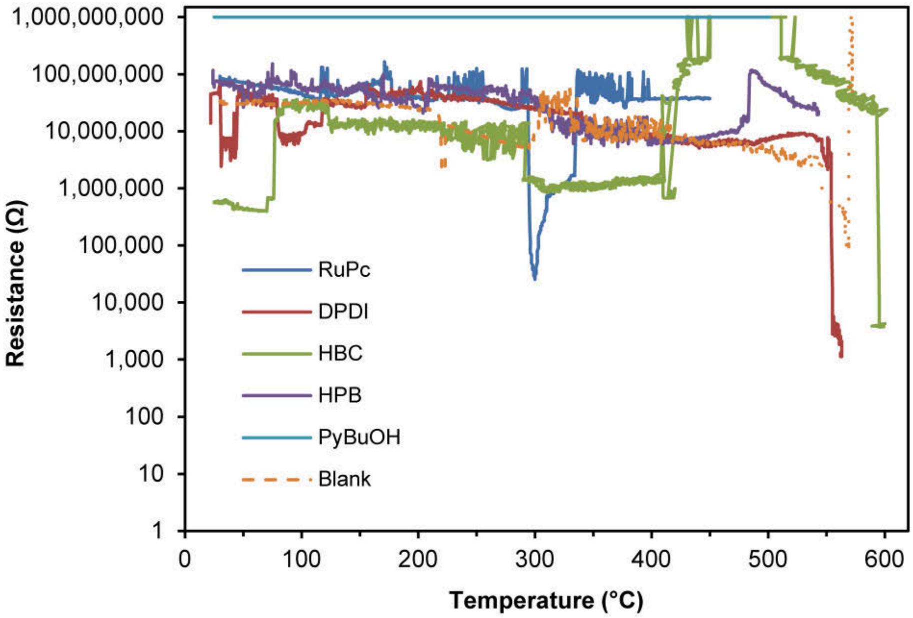

Figure 4.26. Raw data for resistance versus temperature measurements of the solid unbound stabilisers and a blank substrate with electrodes, heated at 10 °C min^{-1} in air.

Since a number of the unbound stabilisers were ineffective or less effective than expected considering their thermal stability, the interactions between the unbound stabilisers and the thiol capping ligands on the AuNPs was explored. The stabiliser HD was added to both BT@AuNPs and to AuNPs stabilised with octanethiol (OT@AuNPs), and the mixtures were sintered. The addition of HD had no discernible influence on the T_{SE} of BT@AuNPs (Figure 4.23), but adding

HD to OT@AuNPs increased their T_{SE} by ~30 °C. Furthermore, the T_{SE} of OT@AuNPs + HD (208 °C) is closer to the T_{SE} of the bound stabiliser analogue, HDT@AuNPs (221 °C), than to the OT@AuNPs without HD (177 °C). The data in Table 4.5 show that the addition to OT@AuNPs of more than 100 molecules/NP of HD did not provide any further increases in thermal stability. These data suggest that there are greater intermolecular interactions between the unbound HD and the bound OT than between HD and BT, due to the longer carbon chain length of OT compared to BT (Figure 4.27). This effect demonstrates the importance of the unbound stabiliser having an affinity with the capping ligands on the AuNPs in order to function as effective stabilisers against sintering.

Table 4.5. T_{SE} data for OT@AuNPs mixed with HD at different ratios of molecules/NP.

Molecules/NP	T_{SE} (°C)
0	177
100	208
1000	208
10000	203

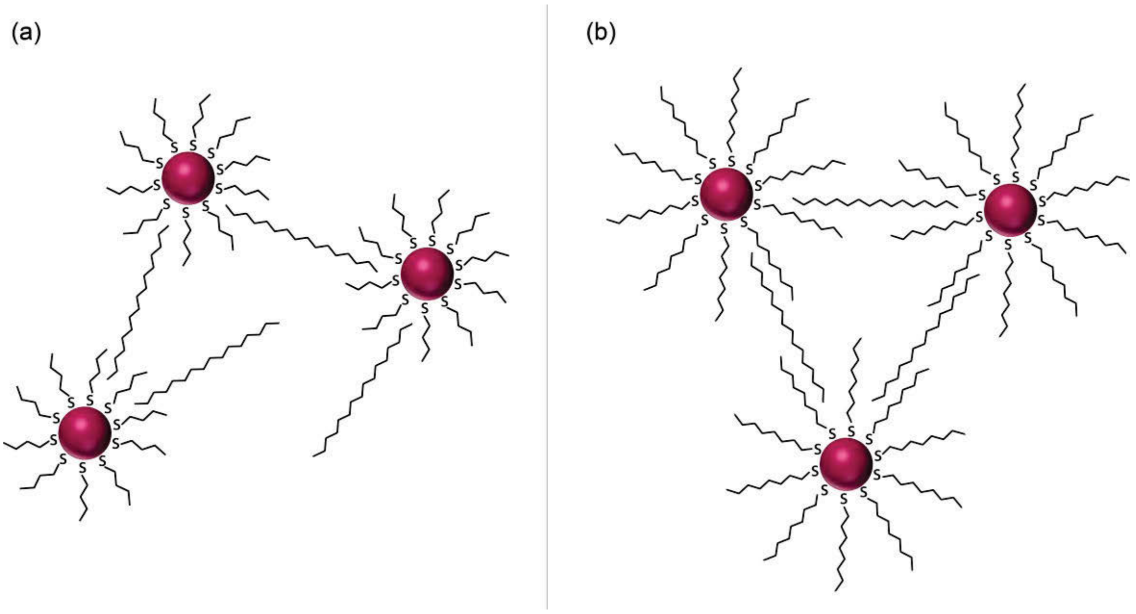

Figure 4.27. Schematic diagram of (a) BT@AuNPs and (b) OT@AuNPs, both with HD interspersed between the particles, depicting the greater intermolecular attraction possible with the longer alkane chains on OT@AuNPs than with BT@AuNPs.

This effect was also observed for films of BT@AuNPs mixed with [RuPc(4-py^{t}Bu)$_2$] upon characterisation by SEM. Clusters of material (Figure 4.28) were dotted throughout the films amongst the AuNPs, with specimens prepared at a higher ratio of molecules/NP containing a greater abundance of these clusters than those at a lower ratio (Figure 4.29). As discussed in more detail below, the clusters contained crystals of [RuPc(4-py^{t}Bu)$_2$].

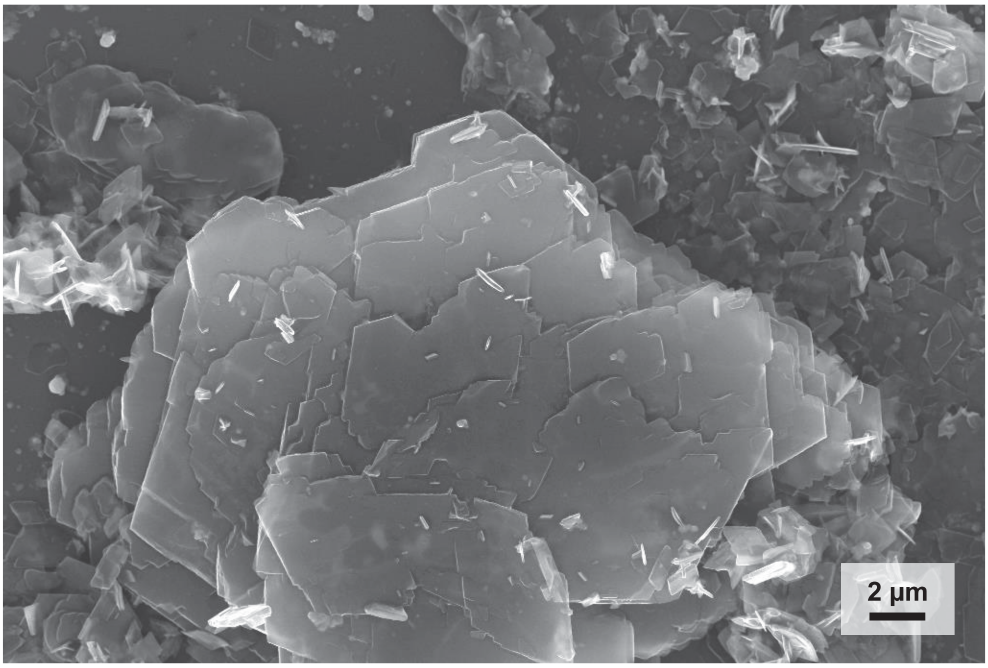

Figure 4.28. SEM image of a mixture of BT@AuNPs and [RuPc(4-py^{t}Bu)$_2$] at a ratio of 250 molecules/NP, deposited using THF.

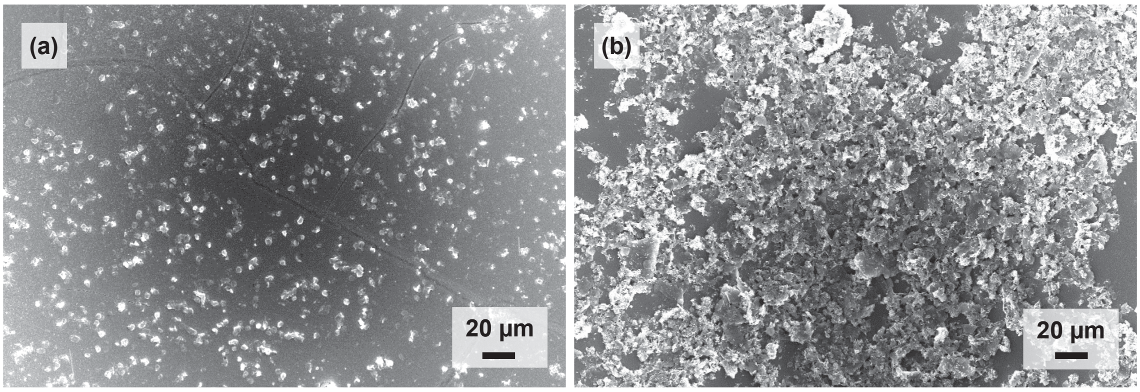

Figure 4.29. SEM images of films of BT@AuNPs mixed with [RuPc(4-py^{t}Bu)$_2$] deposited using THF, prepared at concentrations of (a) 100 and (b) 250 molecules/NP. The higher contrast material in both specimens is identified as crystalline [RuPc(4-py^{t}Bu)$_2$].

Films of a mixture of BT@AuNPs and [RuPc(4-py^{t}Bu)$_2$] at 250 molecules/NP were heated using the same setup used for the electrical resistance measurements, and were removed at certain temperatures to then be imaged by SEM (Figure 4.30). Figure 4.30 a shows an unheated specimen, where the ~3 nm BT@AuNPs are visible on the surface of a RuPc crystal (the same one as shown in Figure 4.28). Layers of AuNPs were also seen directly on the substrate, between the RuPc crystals. At 100 °C (Figure 4.30 b) the film of AuNPs in the regions between the crystals shows the initial sintering stages of diffusion and neck formation between adjacent particles.[16,22] By 200 °C these AuNPs have coarsened into much larger particles of ~20 nm diameter (Figure 4.30 c), while the AuNPs coating the RuPc crystals display a lesser degree of coarsening at this temperature. After heating to 280 °C the crystals develop multiple small holes (Figure 4.30 d), possibly due to the formation of gaseous combustion products (this temperature is near the onset of decomposition of [RuPc(4-py^{t}Bu)$_2$] as measured by TGA (Figure 4.18 c)). By 350 °C the crystals have decomposed, leaving behind distinct outlines containing partially sintered AuNPs where smaller crystals had been (Figure 4.30 e) and formations of gold aggregates where larger crystals had been (Figure 4.30 f). These formations persist upon heating to at least 450 °C (data not shown).

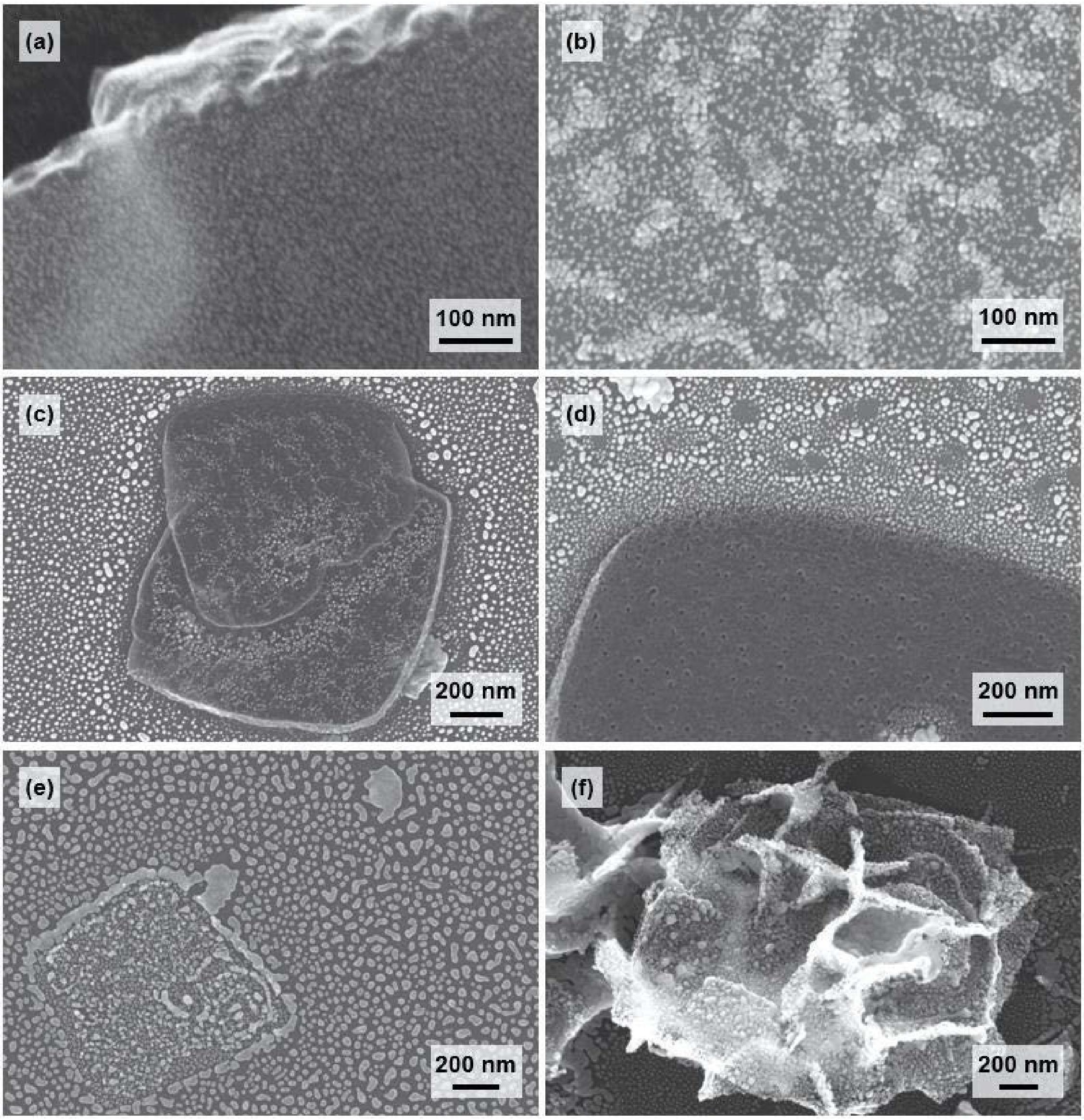

Figure 4.30. SEM images of mixtures of BT@AuNPs and [RuPc(4-py^{t}Bu)$_2$] at a ratio of 250 molecules/NP deposited using THF, (a) unheated and after heating at 10 °C min^{-1} to (b) 100, (c) 200, (d) 280 and (e and f) 350 °C.

The structure of the films formed from these mixtures was found to be dependent on the solvent used to deposit the material onto the substrate. Samples deposited from chloroform dried into ring shaped structures (visible to the eye) with most of the material accumulating around the edge of the ring, leaving a thin blue film (from the colour of the RuPc) in the centre. These samples sintered at temperatures only slightly higher than the T_{SE} of BT@AuNPs (Figure 4.23), with the edge of the ring changing colour from a dark brownish blue to shiny gold while the centre remained blue. SEM was then conducted to examine the microstructure of these deposited films, both before and after heating. Figure 4.31 a shows a segment of the ring structure that formed when using chloroform and Figure 4.31 b shows a similar segment after heating, where the AuNPs have sintered. Closer inspection of the inner edge of the ring structure before heating revealed the presence of large clusters of crystalline [RuPc(4-py^{t}Bu)$_2$] among layers of AuNPs (Figure 4.31 c). Unlike those that formed when using THF (Figure 4.30 a), these crystals are not coated in AuNPs. After heating the sample to 350 °C the crystals disappeared, leaving an uneven film of sintered AuNPs (Figure 4.31 d).

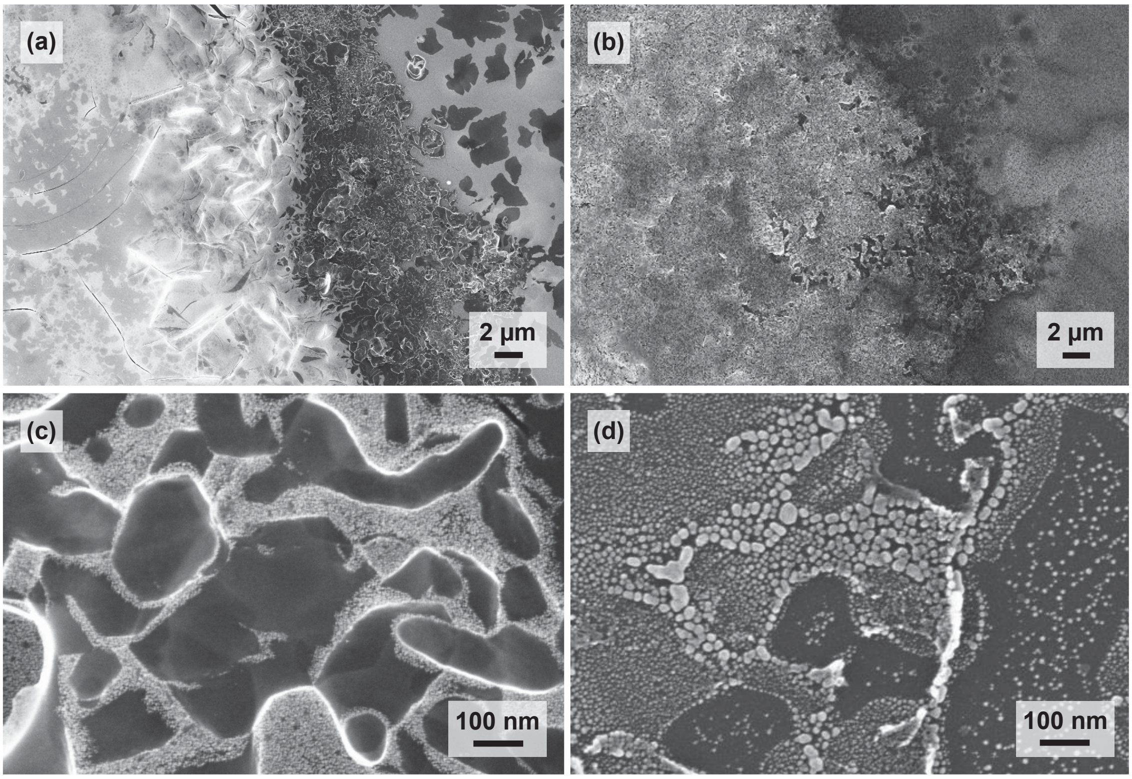

Figure 4.31. SEM images of BT@AuNPs mixed with [RuPc(4-py^{t}Bu)$_2$] at a ratio of 100 molecules/NP deposited using chloroform, (a and c) before heating and (b and d) after heating at 10 °C min^{-1} to 350 °C.

Mixtures of BT@AuNPs and [RuPc(4-py^{t}Bu)$_2$] deposited using THF formed far more uniform films after evaporation of the solvent than films deposited using chloroform. Figure 4.32 a shows a reasonably uniform film of unheated AuNPs deposited using THF. The AuNPs and RuPc molecules have not separated into distinct areas within the film as seen when using chloroform, but the RuPc has still aggregated into crystals that are dotted throughout the sample (Figure 4.32 a). As explained earlier and also shown in Figure 4.30, these crystals decompose after heating to 350 °C (Figure 4.32 b).

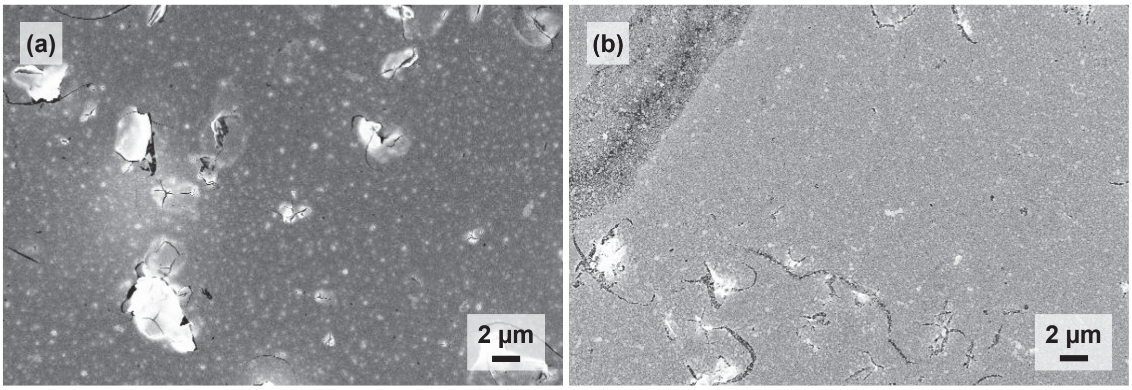

Figure 4.32. SEM images of BT@AuNPs mixed with [RuPc(4-py^{t}Bu)$_2$] at a ratio of 100 molecules/NP deposited using THF, (a) before heating and (b) after heating at 10 °C min^{-1} to 350 °C.

4.5. Summary

The research presented in this chapter shows that the thermal stability of AuNPs can be significantly increased through the use of stabilising compounds with high decomposition temperatures. The stabilising molecules act a robust physical barrier between the particles, and can thus delay the onset of sintering until the decomposition of the stabiliser. This concept was tested here first with AuNPs functionalised with the RuPc complex [RuPc(4-py(CH$_2$)$_3$SAc)(4-py^{t}Bu)], which decomposes at ~350 °C as determined by TGA/DSC. The T_{SE} values for the RuPc-AuNP nanocomposite correlated closely with the TGA results for the onset of decomposition of the RuPc complex, ~330 °C, and were higher than any other results found in the literature for ligand-stabilised AuNPs. The RuPc complex, however, was found to leave behind oxidised ruthenium after its combustion, which led to lower conductivity in sintered films of the nanocomposite compared to sintered films of BT@AuNPs. It was also found that using a RuPc complex with sulfur groups on both axial ligands, namely [RuPc(4-pyCH$_2$SAc)$_2$], caused the AuNPs to form insoluble aggregates of interconnected particles.

After the success of [RuPc(4-py(CH$_2$)$_3$SAc)(4-py^{t}Bu)] as a stabiliser to increase the thermal stability of AuNPs, a number of other compounds were tested for their ability to impart thermal stability to AuNPs. Alkanethiol-stabilised AuNPs followed the known trend of increased thermal stability with increasing alkane chain length. OA@AuNPs sintered at ~320 °C, similar to the RuPc-AuNP nanocomposite, while the stabiliser PyBuSH was found to be significantly more effective, with Py@AuNPs sintering at ~390 °C.

It was hypothesised that stabilising compounds need not be anchored to the AuNPs by Au–S bonds, but that AuNPs could be stabilised to high temperatures by the simple inclusion of thermally stable nonthiolated compounds. The compounds selected included some that were analogous to the chosen thiolated compounds, to allow for more direct comparisons to be made between bound and unbound stabilisers, and a range of ratios of molecules to particles was tested for each stabiliser. Many of the unbound stabilisers, namely DD, HD, $[RuPc(4\text{-}py^tBu)_2]$, HPB and PyBuOH, had minimal effects on the thermal stability of BT@AuNPs, even at high ratios of molecules/NP. However, three of the unbound stabilisers were found to be very effective: unbound oleylamine gave T_{SE} values of ~280 °C; HBC-acetylene prevented sintering up to ~350 °C; and DPDI produced T_{SE} values up to ~540 °C, a result that is unprecedented for ligand-stabilised AuNPs. Most of the unbound stabilisers were found to be largely independent of the ratio of molecules/NP in the ranges tested, though the reason for this is as yet unknown. The T_{SE} results for BT@AuNPs mixed with HPB highlight the importance of the AuNPs and stabilising compounds having compatible solubilities.

In the comparisons between analogous bound and unbound stabilisers, the bound stabilisers were generally far more effective, with oleylamine being the only stabiliser to have a comparable effect on thermal stability as both bound and unbound. The greater increase in thermal stability observed for mixtures of HD with OT@AuNPs than for HD with BT@AuNPs demonstrates the need for unbound stabilising compounds to have an affinity for the capping ligands on the AuNPs in order to function as effective stabilisers against sintering. The film structures observed by SEM for mixtures of BT@AuNPs and $[RuPc(4\text{-}py^tBu)_2]$ demonstrate that without an anchoring group, the RuPc molecules do not become homogeneously distributed between the AuNPs in the film but instead aggregate into distinct crystals, in contrast to films formed using $[RuPc(4\text{-}py(CH_2)_3SAc)(4\text{-}py^tBu)]$ as stabiliser. This behaviour leaves the AuNPs vulnerable to sintering at lower temperatures than when the stabiliser is anchored directly to the particles. These results suggest that the primary role of the anchoring group in a stabilising compound is to ensure that the molecules are homogeneously distributed between the AuNPs in a film and remain so during heating, thereby allowing them to act as physical barriers to sintering until the decomposition of the compound.

Chapter 5:

Development of Optical Properties and Microstructure during Thermal Coarsening of Gold Nanoparticle Composites

Chapter 5: Development of Optical Properties and Microstructure during Thermal Coarsening of Gold Nanoparticle Composites

5.1. Introduction

In addition to a significant increase in conductivity, the sintering of a film of AuNPs results in a visible colour change from the dark colour of the strongly absorbing nanoparticles to the lustrous yellow of bulk gold. This change in the optical properties is a result of the Drude response[149] of the electrically conductive gold film; the reflectivity in the near-infrared (NIR) region of the spectrum decreases with increasing wavelength for a film of separated particles, but increases with increasing wavelength when the particles coalesce and the film becomes electrically percolating.[150,151]

A few studies have investigated the effects of heating on the optical properties of AuNP thin films (from one to a few nanoparticle layers thick) and the underlying changes in film morphology.[152–154] Both red- and blue-shifts in the LSPR peak wavelength were observed, depending on the film thickness and temperature or annealing time. Unlike the temperature dependence of the LSPR of individual particles, these changes were not reversible upon returning the films to room temperature. Most of the films used in these studies were too thin to become electrically percolating upon heating, but instead became rougher with the formation of relatively large, discrete islands of gold as the particles coalesced.

The results presented in Chapter 4 showed that certain organic compounds with high decomposition temperatures could increase the thermal stability of AuNPs. In addition to sintering at higher temperatures, AuNPs stabilised with these compounds also sintered far more gradually than the AuNPs stabilised with alkanethiols. This prolonged sintering event provides a window for monitoring the changes to the optical properties of AuNP films throughout the sintering process, and over a greater temperature range than would otherwise be possible with AuNPs of lower thermal stability. Knowledge of such changes may be applied in the development of sensors such as thermal history indicators, which indicate whether a temperature sensitive material has at some point been exposed to temperatures above a critical level.[155]

Due to their small size, the atoms in nanoparticles are often not particularly well ordered, but as AuNPs are heated, allowing them to grow and sinter, the gold can become more crystalline, a process known as annealing or recrystallisation.[16,156] Changes in the microstructure of some of the stabilised AuNPs from Chapter 4 were monitored by XRD during heating, to see if the stabilisers had an effect on the recrystallisation of the particles. The coalescence and recrystallisation of BT@AuNPs has already been studied by Cortie *et al.*,[16] allowing for direct comparison here with BT@AuNPs mixed with unbound stabilisers to determine what effects the stabilisers may have on the recrystallisation of the gold.

5.2. Changes in Optical Properties of AuNP Films with Temperature

Films of AuNPs were prepared on glass slides and the optical properties of the films were monitored by *in situ* reflectance spectroscopy during heating. The AuNPs were stabilised with one of four ligands: 1-butanethiol, 1-octanethiol, oleylamine and PyBuSH. These compounds were chosen since they are reasonably transparent in the visible and NIR regions of the electromagnetic spectrum, and oleylamine and PyBuSH both greatly increase the thermal stability of AuNPs (Chapter 4.4). 1-Butanethiol and 1-octanethiol were included as low thermal stability comparisons.

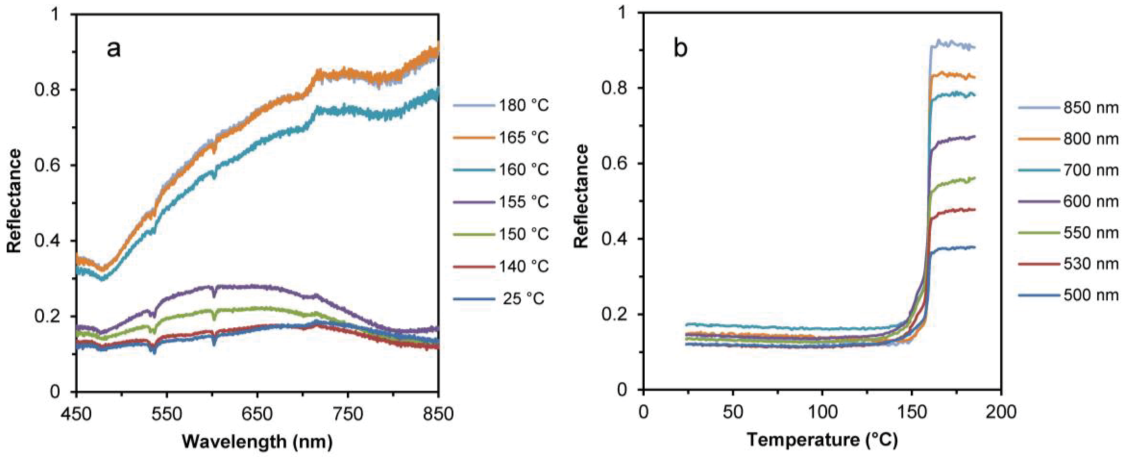

Figure 5.1. Raw reflectance data obtained from a film of BT@AuNPs during heating: (a) as a function of wavelength and (b) as a function of temperature.

The *in situ* reflectance data for a film of BT@AuNPs upon heating are shown in Figure 5.1, and the data for a film of OT@AuNPs are shown in Figure 5.2, both as a function of wavelength (Figures 5.1 a and 5.2 a) and as a function of temperature (Figures 5.1 b and 5.2 b). For the sake of clarity, only a select few of the collected spectra are displayed here. The as-prepared BT@AuNP film appeared dark brown in colour and its initial spectrum lacked a plasmon resonance peak (Figure 5.1 a), due to the small size of the AuNPs.[127] The as-prepared film of OT@AuNPs was a dark purple colour, and its initial spectrum showed a plasmon resonance peak at ~600 nm, which is red-shifted compared to that of the colloidal suspension (518 nm). This red-shift is caused by complex electromagnetic interactions between AuNPs that are in close proximity (but not touching).[29,157] The initial reflectance of both films was low and the spectra remained largely unchanged up to the sintering events, whereupon the reflectance rapidly increased, particularly in the NIR region, indicating that the films had percolated to become electrically conductive.[151] This sharp increase in reflectance occurred between 155 and 160 °C for BT@AuNPs (Figure 5.1) and between 226 and 228 °C for OT@AuNPs (Figure 5.2). The resulting spectra resembled the reflectance spectrum of bulk gold, with its characteristic absorption edge in the mid-visible (Figure 5.3),[158] confirming that sintering had occurred.[16]

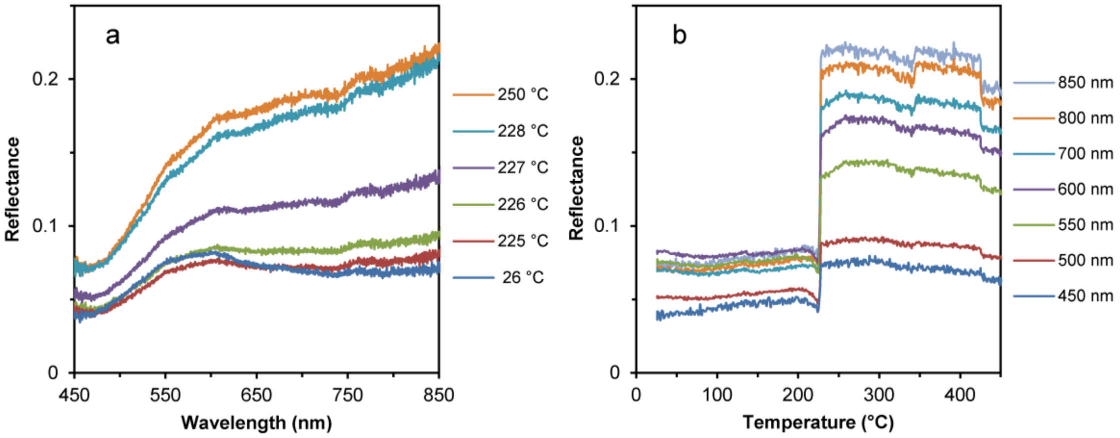

Figure 5.2. Raw reflectance data obtained from a film of OT@AuNPs during heating: (a) as a function of wavelength and (b) as a function of temperature.

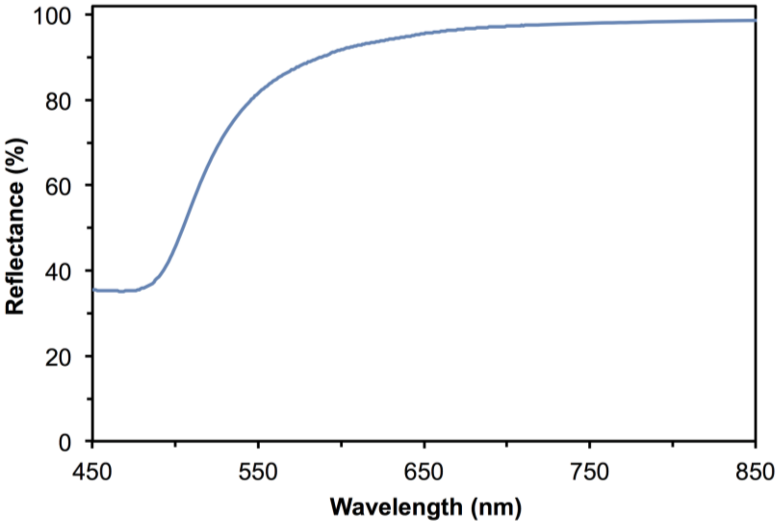

Figure 5.3. Reflectance spectrum of bulk gold.

It is interesting to note that the reflectance peak detected for the film of OT@AuNPs prior to sintering (Figure 5.2 a) represents only a small component of the LSPR of the particles; a larger resonance peak would be observed if measuring transmission. Modelling (performed by Dr Angus Gentle of UTS) of the transmission and reflection spectra of AuNPs using the Maxwell Garnett effective medium approximation[159] shows a small reflection peak and a larger transmission trough at ~520 nm (Figure 5.4). Calculating the amount of incident light absorbed by a film of AuNPs must therefore take into account the light reflected from the surface as well as the light transmitted through the film.[160] Thus the absorption spectrum in Figure 5.4 is a result of subtracting both the transmission and reflection spectra from the total incident light.

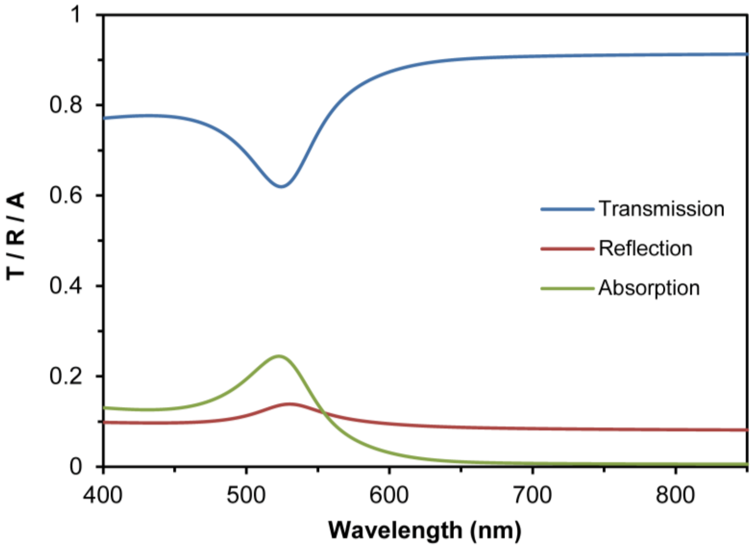

Figure 5.4. Spectra calculated by Dr Angus Gentle (UTS) of transmission, reflection and absorption for 30% gold spheres in air (20 nm thick) on glass, using the Maxwell Garnett effective medium approximation.

In terms of probing the optical properties and structural changes occurring during the sintering process, BT@AuNPs and OT@AuNPs sinter far too rapidly for any useful information on this transition to be acquired.

OA@AuNPs have much greater thermal stability than alkanethiol-stabilised AuNPs (Chapter 4.4), with a T_{SE} as high as ~320 °C (Table 4.4). Additionally, the sintering event occurs over a much wider temperature range, on the order of ~100 °C (Figure 4.22). The reflectance spectra collected while heating a film of OA@AuNPs are displayed in Figure 5.5, and the same reflectance data as a function of temperature are shown in Figure 5.6. The initial film reflectance (Figure 5.5 a) was low, with a plasmon resonance peak at ~546 nm. Up to 100 °C, heating caused a slight decrease in the plasmon peak amplitude (Figure 5.5 a), consistent with literature describing the temperature dependence of the LSPR of AuNPs.[68,78] Heating from 100 to 200 °C (Figure 5.5 b) resulted in a red-shift of the plasmon peak and a more than doubling of its reflectance, along with a broadening of the spectrum. This change may be attributed to partial coalescence of the AuNPs to form various configurations containing fused particles.[22,67] Between 200 and 340 °C (Figure 5.5 c) the reflectance at wavelengths longer than 630 nm increased incrementally as more particles coalesced, with the film becoming fully sintered (and therefore conductive) by 320 °C. This gradual change in reflectance is consistent with the electrical resistance data for OA@AuNPs (Figure 4.22) where the change in resistance decreases gradually between ~260 and 350 °C, with the maximum rate of change (the definition of T_{SE}) at ~320 °C. Upon heating the film above 340 °C, a decrease in film reflectance across the spectrum was observed (Figure 5.5 d)

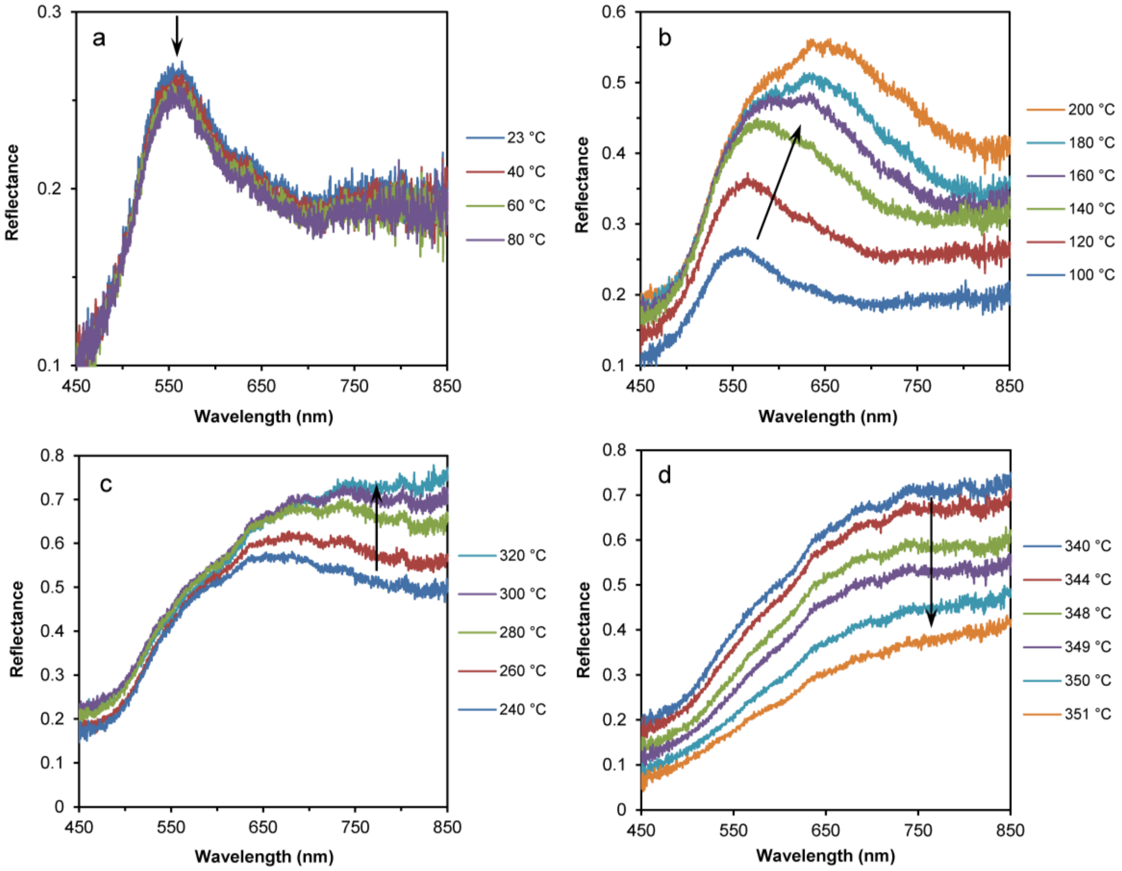

Figure 5.5. Reflectance spectra obtained from a film of OA@AuNPs during heating, separated into selected temperature ranges: (a) 23–80 °C, (b) 100–200 °C, (c) 200–340 °C and (d) 340–351 °C.

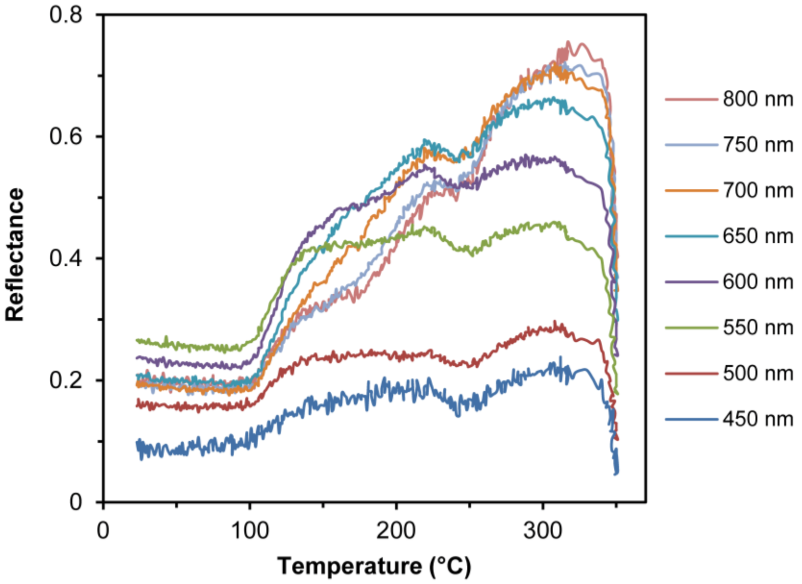

Figure 5.6. Reflectance as a function of temperature for a film of OA@AuNPs at a range of wavelengths.

Analysis of the sintered film by SEM revealed this decrease to be the result of the film breaking up into islands, causing more of the incident light to be scattered or transmitted rather than reflected. The process of island formation, or de-wetting, upon the annealing of thin metallic films has been examined in the literature,[161] and is driven by the kinetic process of surface energy minimisation.[141] Thinner films undergo de-wetting at lower temperature and form smaller islands than thicker films,[161] as demonstrated in Figure 5.7, which shows the border between a thicker region of the sintered film (left) and a thinner region (right). The thinner region had entirely broken up into sub-micron sized islands, while the thicker area remained as a continuous film. The boundary between the two regions shows the intermediate phases of hole development and the separation of the gold into islands via neck formation.

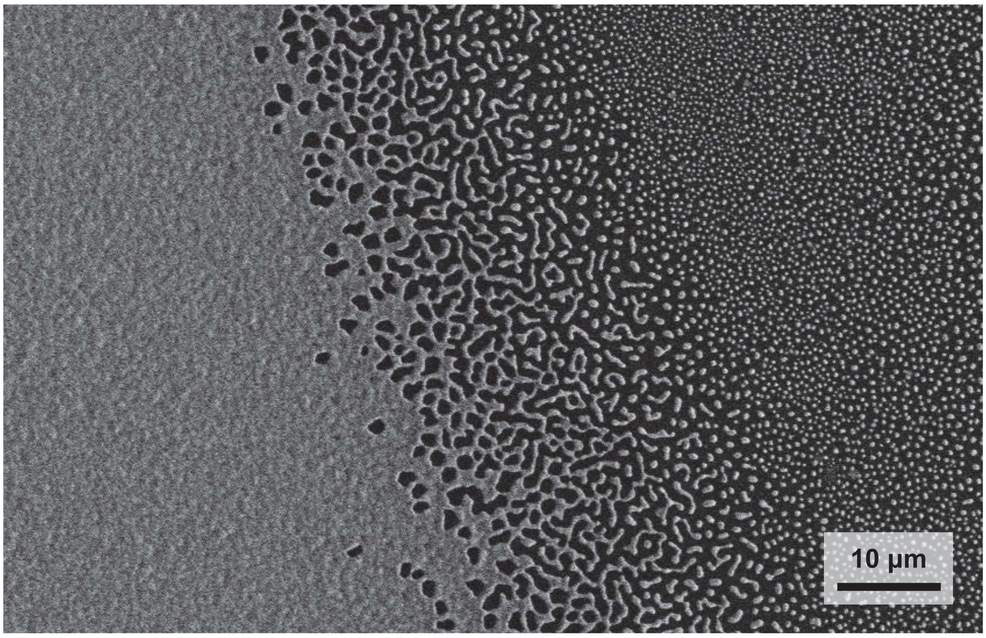

Figure 5.7. SEM image of a sintered film of OA@AuNPs on glass after being heated to 350 °C.

The changes in particle and film structure that correspond to the changes in optical properties were probed by preparing films of OA@AuNPs and heating each film to a particular temperature while recording its reflectance, and then analysing the films by SEM. Schematic illustrations and SEM images of the resulting particle shapes are displayed in Figures 5.8 a and 5.8 b, respectively. The sample shown in Figure 5.8 b at 25 °C has a lower coverage of AuNPs than the others. At 25 °C, the OA@AuNPs were at their original size and shape (~5 nm diameter and spherical). By 135 °C the particles began to coarsen, increasing in diameter to ~15–20 nm, though they maintained a spherical shape; this corresponds to the increased reflectance measured at this temperature (Figure 5.8 c). Upon heating to 173 °C, the particles became significantly larger in diameter and developed into a number of different shapes, such as rods, hexagons and triangles. The corresponding reflectance spectrum indicates that this film was not electrically conductive and thus the particles were still insulated from each other. At

295 °C the particles were only slightly larger than at 173 °C and with the same variety of shapes present, though lower magnification SEM images (Figure 5.9) show that microstructures had developed in the film that were not present at 173 °C. The significant increase in the NIR reflectance at 295 °C (Figure 5.8 c) shows that the film is very close to the electrical percolation threshold.[150] By 472 °C large islands of sintered gold are observed, which correlates with the measured decrease in reflectance after prolonged heating (Figure 5.5 d).

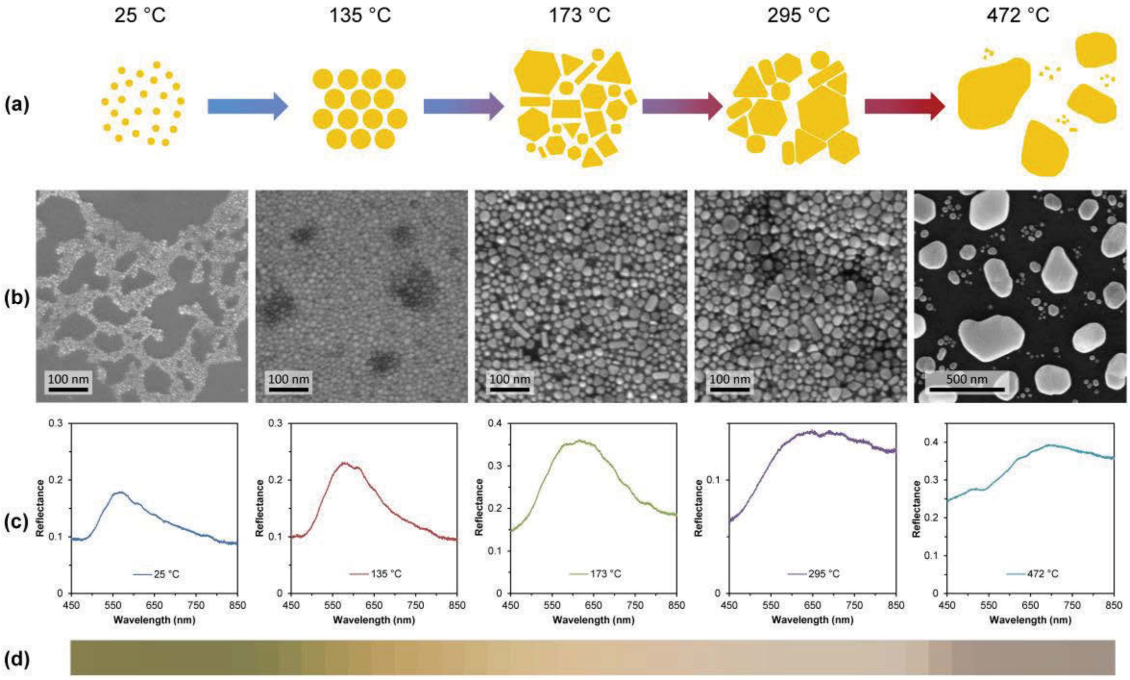

Figure 5.8. Particle structure and corresponding optical properties for films of OA@AuNPs heated from room temperature (left) to certain temperatures up to 472 °C (right): (a) schematic illustrations of the particle morphology, (b) SEM images of the AuNP films after heating to each temperature, (c) optical reflectance spectra collected *in situ* (at temperature) for the films shown in (b), and (d) RGB colors recovered from the reflectance spectra of the film heated from room temperature to 472 °C using standard tables for CIE XYZ and CIE L*a*b*.

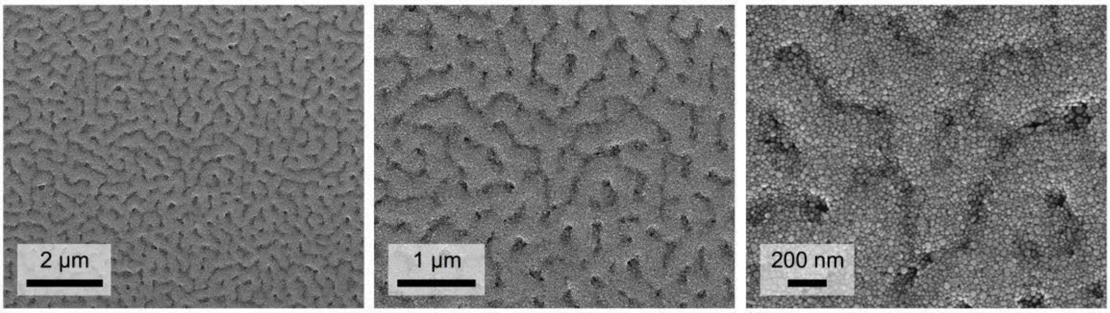

Figure 5.9. SEM images of a film of OA@AuNPs on silicon, heated to 295 °C.

The changing colour of a film of OA@AuNPs as it was heated was extracted by Prof. Michael Cortie (UTS) from the recorded reflectance spectra of the film heated to 472 °C, using the widely used CIE L*a*b* colour coordinates (Figure 5.8 d). L (luminance) indicates how bright the colour is, a* parameterises the green to red components, and b* the blue to yellow components. The colour of the film as seen by the naked eye varies somewhat depending on the viewing angle (due to its shininess), so the colours extracted from the reflectance spectra are specific to the angle of the instrument's detector (15° from normal incidence to the sample). Figure 5.8 d shows the colour of the film evolving from a tarnished brass colour to the bright yellow of bulk gold with a strong increase in luminance. Then after prolonged heating, the colour darkens as the reflectance decreases, due to the roughening of the film as it forms islands.

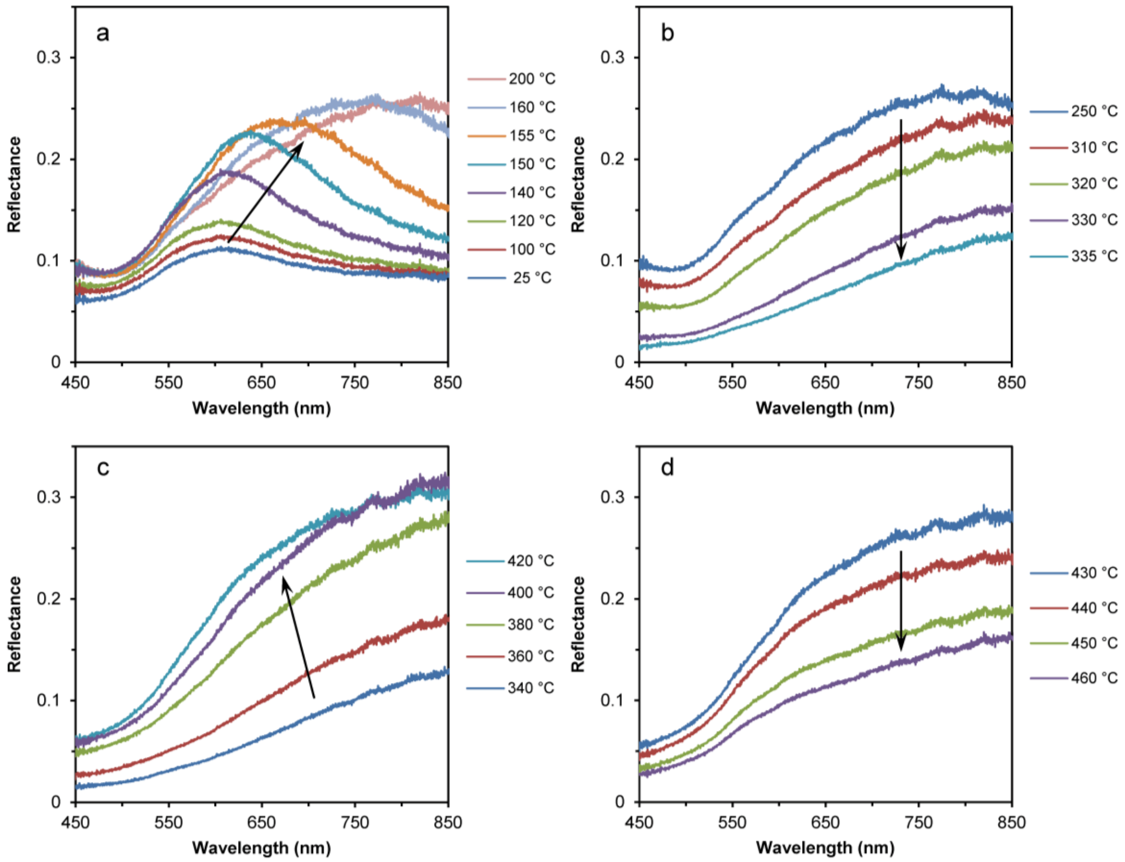

Figure 5.10. Reflectance spectra obtained from a film of Py@AuNPs during heating, separated into selected temperature ranges: (a) 25–200 °C, (b) 250–335 °C, (c) 340–420 °C and (d) 430–460 °C.

Py@AuNPs also have very high thermal stability, with a T_{SE} of ~390 °C (Table 4.4), and sinter over a wide temperature range (Figure 4.21). The reflectance data for a film of Py@AuNPs during heating are shown in Figures 5.10 and 5.11. At 25 °C a plasmon resonance peak is observed at ~600 nm (Figure 5.10 a). The spectra remained virtually unchanged up to ~80 °C, then between 80 and 200 °C the reflectance of the plasmon peak significantly increased and red-shifted to ~800 nm (Figure 5.10 a). This trend is very similar to that observed with the OA@AuNPs in the same temperature range (Figure 5.5 b), and suggests the Py@AuNPs are also coarsening without yet sintering (decreasing NIR reflectance with increasing wavelength at

200 °C (Figure 5.10 a) indicates the film was not conductive).[150] There was very little change in the spectra from 200 to 250 °C (Figure 5.11), but then between 250 and 335 °C the reflectance of the film significantly decreased across the spectrum (Figure 5.10 b). This decrease may be due to changes in the optical properties of the PyBuSH stabiliser as it decomposes (which TGA shows occurs within this temperature range (Figure 4.18 b)), such as a darkening of the colour and roughening of the texture, which would cause less light to be reflected. These changes were observed during the heating of the analogous unbound stabiliser PyBuOH (Figure 5.12). The NIR reflectance of the Py@AuNP film also began increasing with increasing wavelength between 250 and 335 °C (Figure 5.10 b), suggesting the gold has crossed the percolation threshold to become conductive, which is expected to coincide with the decomposition of the stabilising compound. Between 340 and 420 °C the reflectance of the film greatly increased (Figure 5.10 c) until the spectrum resembled that of bulk gold (Figure 5.3), which may be from the removal of the PyBuSH and its decomposition by-products and the consequent development of the gold into a more continuous film. The decreasing reflectance between 430 and 460 °C (Figure 5.10 d) is again due to the breaking up of the gold film into discrete islands.[161]

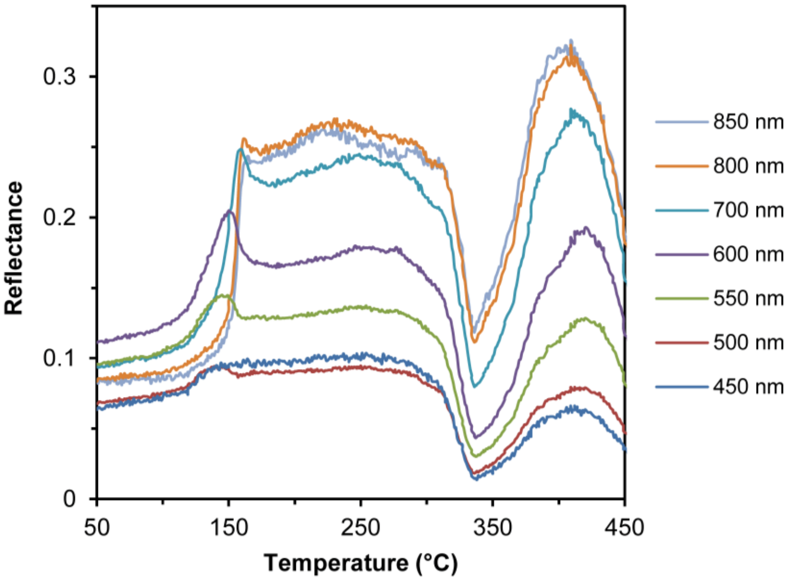

Figure 5.11. Reflectance as a function of temperature for a film of Py@AuNPs at a range of wavelengths.

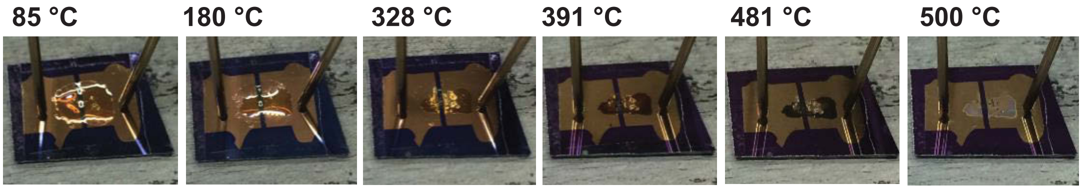

Figure 5.12. Photos of PyBuOH on a silicon/gold substrate as it is heated at 10 °C min^{-1} in air, showing the colour changes as the compound decomposes (m.p. 81 °C).

Another film of Py@AuNPs that was heated while measuring its reflectance spectrum broke up into islands small enough that a plasmon peak reappeared at ~550 nm. The LabVIEW programme was then set to continue collecting reflectance spectra after the heat source was turned off and the film was allowed to cool. As shown in Figure 5.13, the plasmon peak steadily increased in reflectance and blue-shifted slightly as the film cooled to near room temperature. This observation is consistent with the known, reversible effects of temperature on the LSPR of AuNPs: when heated, the plasmon peak red-shifts from thermal lattice expansion and also broadens and decreases in intensity due to increased electron-phonon scattering.[78] However, this may be the first time the phenomenon has been observed in AuNPs that formed from the de-wetting of a continuous gold film on a substrate, as opposed to AuNPs embedded within glass or silica to prevent them sintering at the extreme temperatures required to observe this phenomenon.

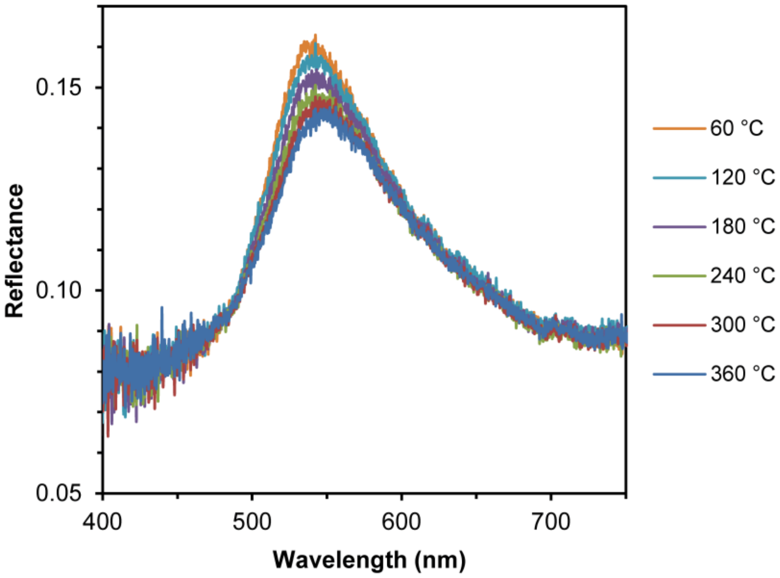

Figure 5.13. Reflectance spectra of a film of Py@AuNPs as it cooled after being heated to 450 °C.

5.3. Recrystallisation of Stabilised AuNPs

OA@AuNPs and mixtures of BT@AuNPs with the unbound stabilisers [RuPc(4-py^{t}Bu)$_2$] and DPDI were taken to the Australian Synchrotron to monitor the changes in their crystal structures during heating. Mixtures were prepared at two ratios for each stabiliser: 100 and 500 molecules/NP, and have been labelled here as RuPc-100, RuPc-500, DPDI-100 and DPDI-500. All samples were heated at 10 °C min^{-1}, but RuPc-500 was also heated at 2, 15 and 25 °C min^{-1}.

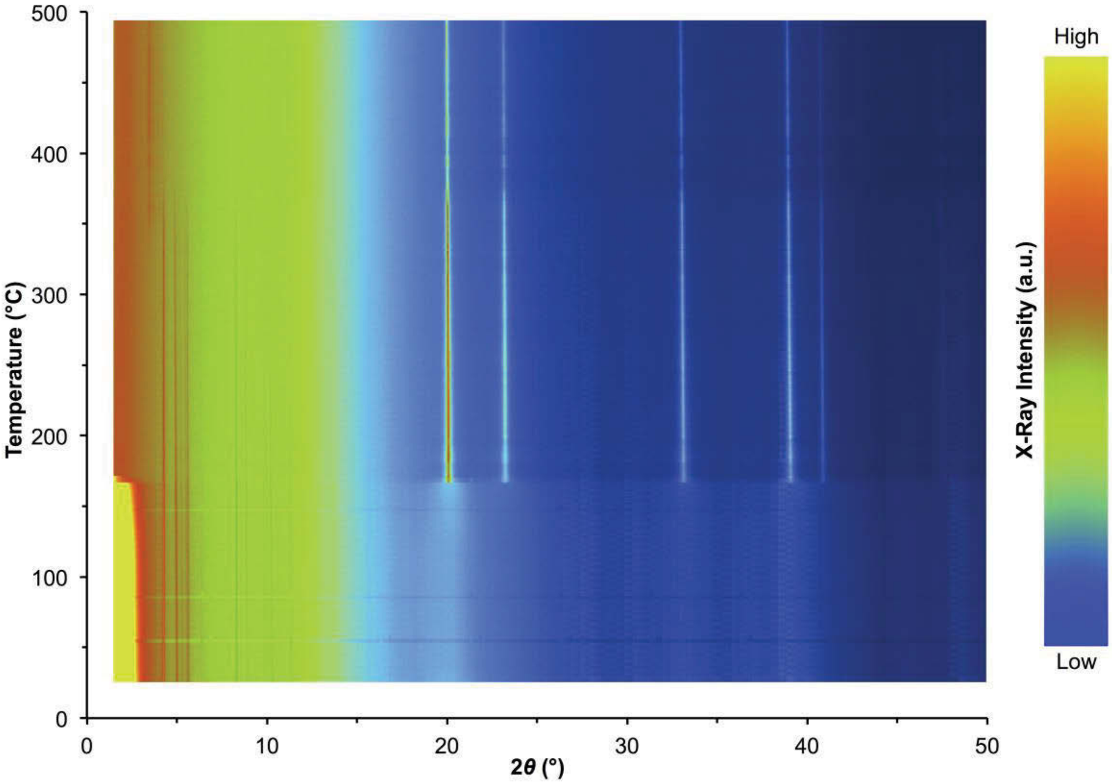

Figure 5.14. X-ray intensity plot for RuPc-500 heated at 2 °C min^{-1}.

The X-ray patterns displayed a few similarities between each of the samples. Figure 5.14 shows an X-ray intensity plot for RuPc-500 heated at 2 °C min^{-1} as an example. A broad, intense peak was present at ~1.7° 2θ, which represents particle-to-particle scattering. This peak disappeared at ~170 °C (for most samples it was observed to increase in intensity before shifting off the scale to lower angles), which coincided with the recrystallisation of the gold, seen as the appearance of a number of sharp peaks; the most intense of these is the gold {111} peak at ~20° 2θ, while the other peaks between 20 and 40° 2θ correspond to other planes of the gold crystal. For the samples RuPc-100 and RuPc-500, several sharp peaks were evident between 4 and 11° 2θ that faded out at ~370 °C. Since no phthalocyanines could be found in databases of XRD patterns for known compounds, powder diffraction was performed on [RuPc(4-py^{t}Bu)$_2$] (Figure 5.15). After adjusting the data for the different X-ray wavelength used, which shifted all the peaks to lower angles (data not shown), the peaks in the XRD pattern lined up with those observed for RuPc-500 (Figure 5.14). A new peak at ~3° 2θ appeared as the RuPc peaks disappeared at ~370 °C, indicating the RuPc had converted to another compound. However, this new peak did not match the XRD pattern for any form of oxidised ruthenium, nor any other compound in the database, so its identity remains unknown. The intensity of the gold peaks also decreased at ~370 °C. It was observed for many of the samples containing RuPc that gases were generated as the RuPc decomposed, causing gaps to open in some of the sample material in the capillaries, which likely explains this reduced peak intensity.

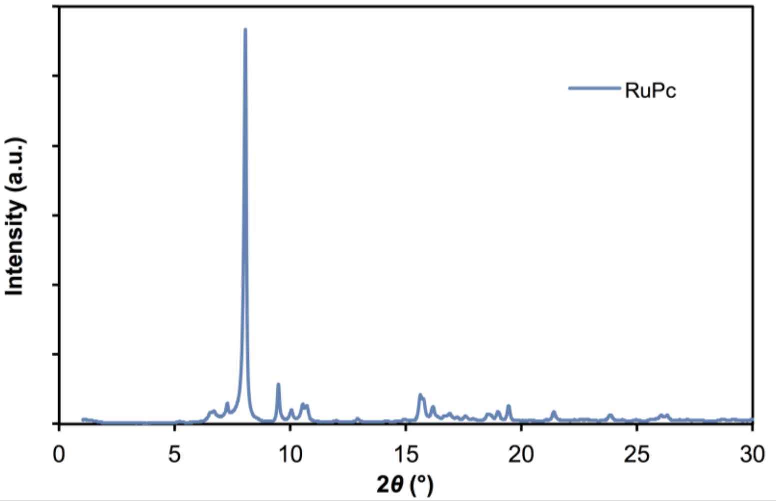

Figure 5.15. Powder diffraction pattern for [RuPc(4-py^{t}Bu)$_2$].

Figure 5.16 a shows the height of the gold {111} peak as a function of temperature for each of the samples heated at 10 °C min^{-1}, and Figure 5.16 b shows the corresponding full width at half maximum (FWHM). The sudden increase in peak height and simultaneous fall in FWHM for each sample indicates the recrystallisation and coarsening of the AuNPs. The recrystallisation temperature was only slightly affected by the identity of the unbound stabilisers tested here (DPDI and RuPc), occurring around 180–190 °C for mixtures of BT@AuNPs with RuPc and around 190–210 °C for mixtures with DPDI (Figure 5.16 a). This temperature range is very similar to that reported in XRD studies on BT@AuNPs by themselves.[16] In contrast, recrystallisation of the OA@AuNPs occurred at a higher temperature and over a significantly wider range (230–350 °C). This result correlates with both the reflectance spectroscopy measurements and electrical resistance measurements of OA@AuNPs, where the films were observed to slowly become conductive between 240 and 320 °C in the former (Figure 5.5 c), and between 260 and 350 °C in the latter (Figure 4.22). The FWHM of the gold {111} peak for OA@AuNPs was also much smaller than for the mixtures (Figure 5.16 b), indicating larger and more perfectly formed grains, which is likely due to the OA@AuNPs being larger than the BT@AuNPs.

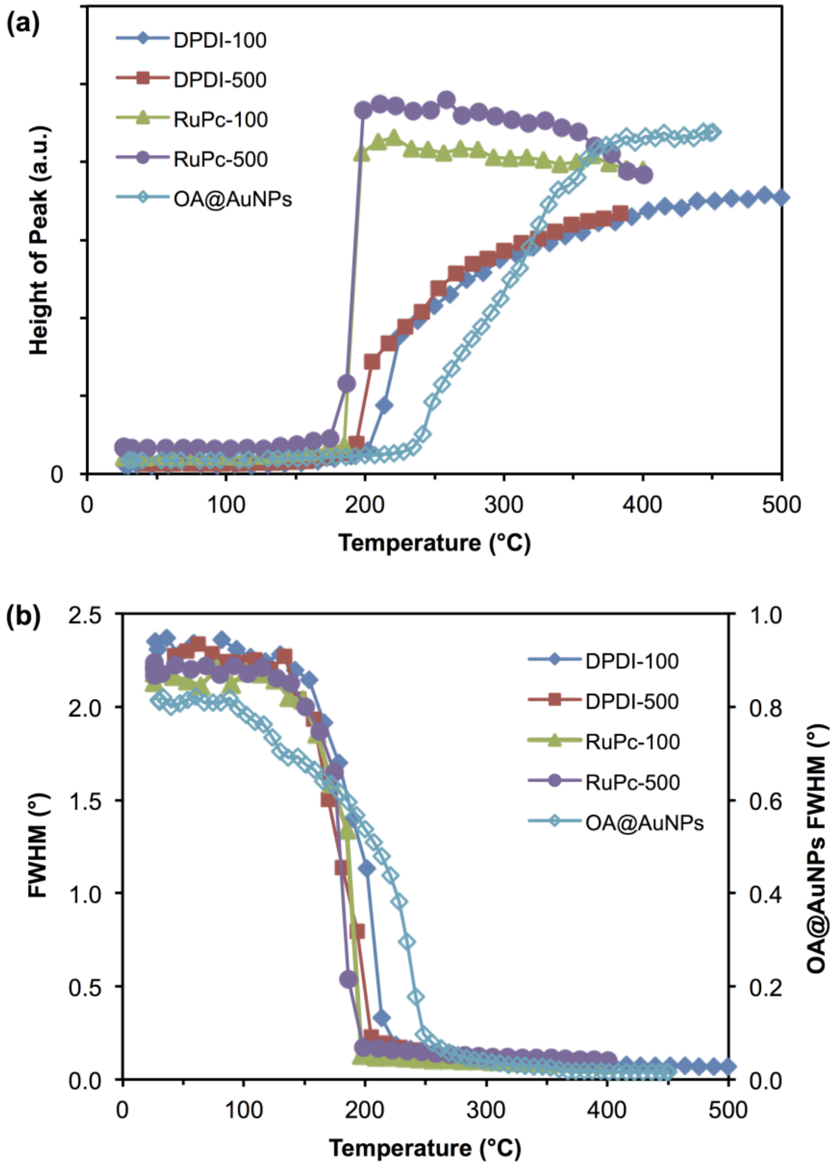

Figure 5.16. Characteristics of the diffraction peak for Au {111} as a function of temperature. Ramp rate for all data was 10 °C min^{-1}. (a) Peak height for OA@AuNPs, DPDI and RuPc samples versus temperature. (b) Full width at half maximum (FWHM) value of peak for OA@AuNPs, DPDI and RuPc samples versus temperature.

The effect of heating rate (between 2 and 25 °C min^{-1}) on the recrystallisation of the gold was also examined, using the RuPc-500 mixture (Figure 5.17). The rapid increase in peak height associated with recrystallisation occurred at a slightly lower temperature for the sample heated at 2 °C min^{-1}, at ~170 °C, while the onset of recrystallisation occurred at ~190 °C for the samples heated at 10 and 15 °C min^{-1} and at ~200 °C for the sample heated at 25 °C min^{-1}. This trend is consistent with that seen in the XRD results of Cortie *et al.*[16] and may be explained since recrystallisation, like sintering, is a thermally activated kinetic process that therefore depends on heating rate.[15,156]

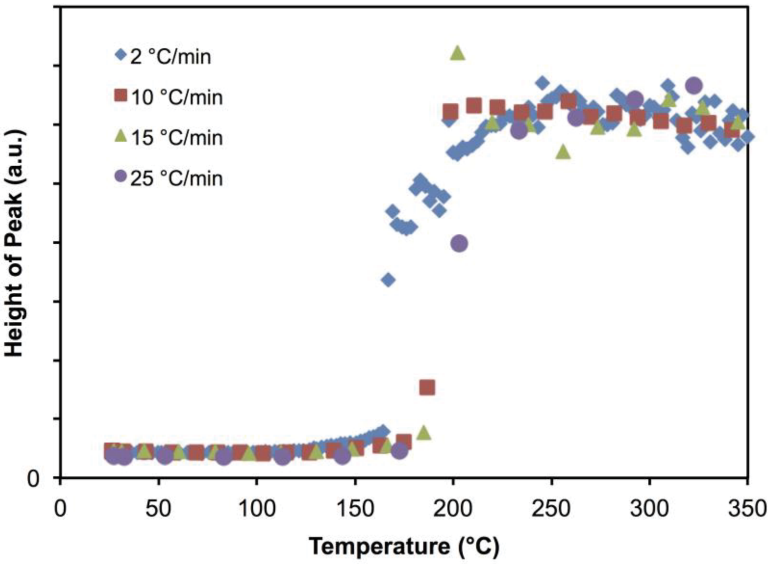

Figure 5.17. Height of the Au {111} peak in the sample RuPc-500, as measured at various heating rates.

Figure 5.18 shows the height and FWHM of the peak at ~4.3° 2θ, which belongs to the RuPc in the RuPc-500 mixture and corresponds to a crystal lattice spacing of 11.05 Å. Depending on the heating rate, the complex decomposed by 380–420 °C, which correlates reasonably well with the TGA results of the RuPc complex (Figure 4.18 c). It is important to note that the AuNPs recrystallised long before the RuPc peaks disappeared from the XRD pattern (Figure 5.14). Similarly, TGA results for the DPDI stabiliser (Figure 4.18 d) showed the majority of its mass loss occurring around 600 °C, yet the DPDI-100 and DPDI-500 samples recrystallised at ~200 °C despite the continued presence of the stabiliser (which is inferred from TGA results since the waxy DPDI compound could not be detected by XRD). In terms of electrical resistance measurements, BT@AuNPs mixed with DPDI at 100 molecules/NP sintered to become electrically conductive at ~150 °C (Figure 4.23), which is somewhat lower than their recrystallisation temperature, but BT@AuNPs with 500 molecules/NP of DPDI sintered at ~485 °C (Figure 4.24), which is much higher than the recrystallisation temperature. These results suggest that sintering and recrystallisation are independent events, with sintering able to occur either before or after recrystallisation, depending on the chosen stabiliser. Knowledge of this flexibility in the sequence of these phenomena may provide additional degrees of freedom in the development of various nanomaterials such as gold sinter inks.

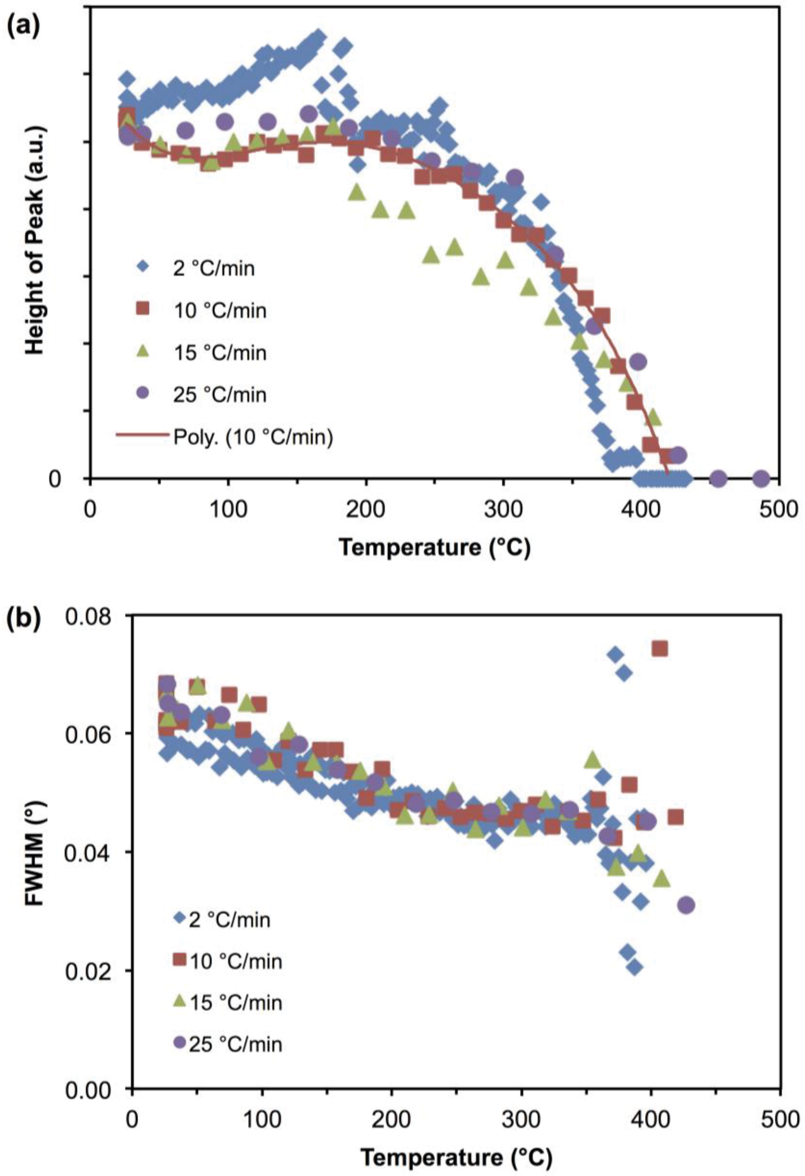

Figure 5.18. (a) Peak height and (b) FWHM of the RuPc peak at 4.3° 2θ, as detected in the RuPc-500 mixture at various temperatures and ramp rates.

5.4. Summary

In this chapter, the effects of temperature on the optical properties and microstructure of AuNPs stabilised by different compounds were examined via *in situ* reflectance spectroscopy, SEM and synchrotron XRD. The sintering characteristics of these AuNPs depend on the nature of their stabilising ligands. For example, AuNPs stabilised with 1-butanethiol or 1-octanethiol sinter very rapidly, which was seen by reflectance spectroscopy as a sharp transition from the spectrum of a dark film of nanoparticles to the spectrum of lustrous bulk gold. Conversely, the sintering of AuNPs stabilised with oleylamine or PyBuSH proceeds much more gradually than the BT@AuNPs and OT@AuNPs, as well as at a higher temperature. Reflectance measurements of films of OA@AuNPs showed a gradual but significant red-shift in the LSPR peak wavelength and a more than doubling of its reflectance between 100 and 200 °C, which indicates a process of nanoparticle coarsening prior to sintering. This coarsening was confirmed by SEM analysis, which revealed both an increase in particle size and a change in particle shape from spherical to a range of shapes such as rods, hexagons and triangles. Heating the films to 300 °C led to a change in the reflectance spectrum to that of bulk gold as the particles sintered and the film became electrically percolating. Continued heating caused the film to undergo surface tension-driven island formation, resulting in a decrease in reflectance. Reflectance measurements of films of Py@AuNPs displayed similar characteristics to those of OA@AuNPs, though with some possible interference from the decomposition by-products of the stabiliser. The reversible effects of temperature on the LSPR of AuNPs were observed during the cooling of a film of gold that had broken up into islands small enough to display plasmon resonance effects. The dramatic changes in optical properties of these AuNP films over such a wide temperature range make them promising candidates for use in sensing technologies.

In situ XRD analysis was performed on OA@AuNPs and mixtures of BT@AuNPs with DPDI and [RuPc(4-py^{t}Bu)$_2$]. Recrystallisation of the gold occurred at 180–190 °C with the RuPc stabiliser and at 190–210 °C with the DPDI stabiliser, which is similar to BT@AuNPs on their own (~200 °C),[16] indicating little influence from these stabilisers. The OA@AuNPs behaved differently than the BT@AuNP mixtures, with recrystallisation beginning at a higher temperature of ~230 °C and continuing until ~350 °C, which correlates with the gradual nanoparticle coarsening observed prior to sintering in reflectance spectroscopy and SEM measurements. The RuPc complex produced sharp crystalline peaks in the XRD patterns of samples where it was present, which matches the observation of RuPc crystals in these mixtures in SEM analysis (Figure 4.28). These peaks disappeared at ~400 °C, long after the appearance of the gold crystal peaks. The heating ramp rate had a small effect on the recrystallisation of the gold in the mixtures of BT@AuNPs with RuPc, with slower heating rates leading to recrystallisation at lower temperatures than faster heating rates. For mixtures of BT@AuNPs with RuPc or DPDI, the temperatures of recrystallisation differ from the temperatures of sintering, most notably for the sample DPDI-500, suggesting that the phenomena of sintering and recrystallisation are independent from each other.

Chapter 6:
Conclusions

Chapter 6: Conclusions

This thesis examined the thermal stability of gold nanoparticles stabilised by various organic compounds. The research aims, as outlined in Chapter 1.4, have been addressed and new areas for further study have become apparent.

Firstly, the synthesis of high purity gold chloride using a straightforward procedure was reliably and reproducibly achieved, as presented in Chapter 3. The method was adapted for the laboratory from an industrial gold mining technique, and uses chlorine gas to oxidise the gold and form aqueous solutions of $HAuCl_4$ that can be used directly for nanoparticle synthesis. Not only were the resulting solutions free from impurities, they were also found to be remarkably stable, with a shelf life of at least 3 years, in sharp contrast to the highly unstable commercial gold chloride powder and the aqueous solutions produced by the hypochlorite method, with shelf lives on the order of days or weeks. The reaction is scalable and provides a straightforward means for determining, or even controlling, the final concentration. These properties combine to make the chlorine gas method ideal for use in AuNP synthesis.

The investigation into the thermal stability of AuNPs is reported in Chapter 4, with the aim of determining how different organic stabilisers affect AuNP thermal stability, and probing the upper temperature limits for stabilising AuNPs with organic compounds. It was discovered that thiol and amine stabilisers with high decomposition temperatures could greatly increase the thermal stability of films of AuNPs by acting as robust physical barriers between the particles, thus preventing sintering until the stabilisers decomposed. AuNPs stabilised with the compounds oleylamine, $[RuPc(4\text{-}py(CH_2)_3SAc)(4\text{-}py^tBu)]$ or PyBuSH resisted sintering up to temperatures well over 300 °C, which is significantly higher than for AuNPs stabilised with the longest alkanethiol tested here, hexadecanethiol (T_{SE} = 221 °C).

Stabilisers without anchoring groups to bind them to the gold were generally less effective than bound stabilisers at increasing the AuNP thermal stability. Analysis indicated that this reduced effectiveness is due to a lack of affinity and/or difference in solubility between the unbound stabilising compound and the AuNPs, leading to non-uniform distributions in the film. Therefore, it appears that the primary role of the anchoring group in a stabilising compound is to ensure a homogeneous distribution of molecules between the particles in a film in order to prevent sintering until the stabiliser's decomposition, and does not depend on the temperature at which the Au–S bond is cleaved. Nevertheless, a few of the unbound stabilisers did induce notably high thermal stability in the AuNP films, namely HBC-acetylene, oleylamine and DPDI, with DPDI giving unprecedented levels of thermal stability for AuNPs stabilised by organic compounds (T_{SE} ~ 540 °C). In the case of HBC-acetylene and DPDI, the results raise the question of how much more effective these stabilisers could be if they were initially bound to the AuNPs, especially considering they both have material remaining up to 600 °C according to TGA measurements. Future work in this area may involve synthesising thiolated analogues of these compounds and testing their effectiveness as stabilisers against sintering. Other combinations of alkanethiol-capped AuNPs and unbound stabilisers could also be tested, since the compound PyBuOH was more effective when mixed with OT@AuNPs than with BT@AuNPs.

In terms of applications, future studies could test if the stabilising compounds increase the shelf life of the AuNPs, either as a powder or as a film. Sintering is a kinetic process and so AuNPs will eventually sinter at room temperature. Stabilising compounds create an activation energy barrier to the sintering process, as described in Chapter 1.2.2; as such, compounds that stabilise AuNPs to high temperatures may also provide a larger activation energy barrier than compounds of lower thermal stability, thereby increasing the AuNP shelf life. If the stabilising compound is not bound to the gold (and is compatible enough to be an effective stabiliser), it may be possible to later remove it from the AuNPs via washing with a suitable solvent, so that the added stabiliser would not affect the originally intended function of the particles when they are eventually used.

Chapter 5 explored the changes in optical and structural properties of thermally stable AuNPs during the heating process. *In situ* film reflectance measurements revealed that OA@AuNPs and Py@AuNPs coarsen over a wide temperature range before they sinter, seen as significant red-shifting of the plasmon peaks and increases in reflectance over a period of ~200 °C before the films become electrically percolating. This coarsening was also observed for OA@AuNPs in SEM analysis, which showed a change in particle shape as well as particle size. Future studies could perform SEM analysis on Py@AuNPs to confirm the particle coarsening indicated by the reflectance measurements. The structural properties of OA@AuNPs and mixtures of BT@AuNPs with [RuPc(4-py^{t}Bu)$_2$] and DPDI were monitored during heating by *in situ* XRD analysis. The BT@AuNP mixtures rapidly recrystallised at ~200 °C, much like the BT@AuNPs by themselves, while the OA@AuNPs recrystallised gradually from 230 to 350 °C. Discrepancies between the temperatures for sintering and recrystallisation for the BT@AuNP mixtures suggest that these are independent phenomena, which is significant since it was previously assumed that the processes of sintering, percolation and recrystallisation occur simultaneously, while the results presented here show this is not the case. The independence of these phenomena and the flexibility in the sequence of their occurrence provide additional degrees of freedom in developing new nanomaterials. For example, the sintering of AuNPs can be designed to occur either before or after their recrystallisation through careful selection of the stabilising compounds, in order to produce materials that are sintered but not fully crystalline, materials that are crystalline but not sintered or electrically percolating, or materials that are both sintered and crystalline. Further study using other stabilisers could help elucidate the exact processes involved in the microstructural transitions involved in these phenomena. Overall, the results presented in this chapter may be utilised in applications such as high temperature sensing technologies and in the improved development of nanomaterials.

Appendix

A.1. Functionalisation of AuNPs

The UV-visible spectra of the functionalised AuNPs used in this project (except for the spectrum of RuPc-AuNPs, which is presented in Figure 4.3) are shown in Figure A1. The spectrum of the stabiliser PyBuSH reveals the origins of the sharp peak at 376 nm in the spectrum of Py@AuNPs. The plasmon peak of Py@AuNPs is also slightly red-shifted compared to the other AuNPs, which may be due to the dielectric properties of the PyBuSH stabiliser.

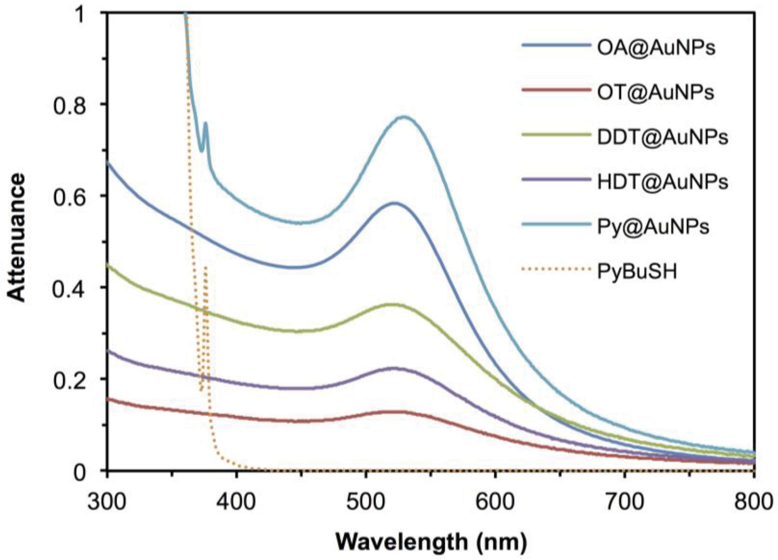

Figure A1. UV-visible spectra of OA@AuNPs, AuNPs functionalised from OA@AuNPs, and the compound PyBuSH. AuNP suspensions are at varying concentrations, and [PyBuSH] = 0.7 mM.

When functionalising AuNPs with alkanethiols, the stability of the resulting colloid was found to depend on the alkanethiol chain length. Attempts to functionalise ~5 nm OA@AuNPs with 1-butanethiol resulted in the particles permanently aggregating and precipitating, leaving the solvent virtually colourless. SEM images of samples of the precipitate are shown in Figure A2. Functionalising AuNPs with 1-octanethiol caused a precipitate to form, but enough particles remained in suspension to give a dark burgundy colloid. SEM showed the OT@AuNPs in the colloid to be very monodisperse with a diameter of ~4 nm (Figure A3). Functionalising AuNPs with 1-dodecanethiol produced less precipitate than with 1-octanethiol, and functionalising with 1-hexadecanethiol produced less still. The DDT@AuNPs appeared slightly less monodisperse than the OT@AuNPs (Figure A4) with diameters of ~4–5 nm, and the HDT@AuNPs resembled the original OA@AuNPs with a diameter range of ~4–6 nm (Figure A5). These observations suggest there is a size limit to particles that a given alkanethiol can stabilise; longer alkanethiols can stabilise larger AuNPs.[88] 1-Butanethiol is evidently too short to stabilise AuNPs ≥4 nm in diameter by ligand substitution; therefore the BT@AuNPs used throughout this project were synthesised directly rather than via OA@AuNPs, and were also smaller in size. OT@AuNPs were also synthesised directly, since functionalising OA@AuNPs with 1-octanethiol resulted in roughly half of the gold (by mass) being lost as a precipitate.

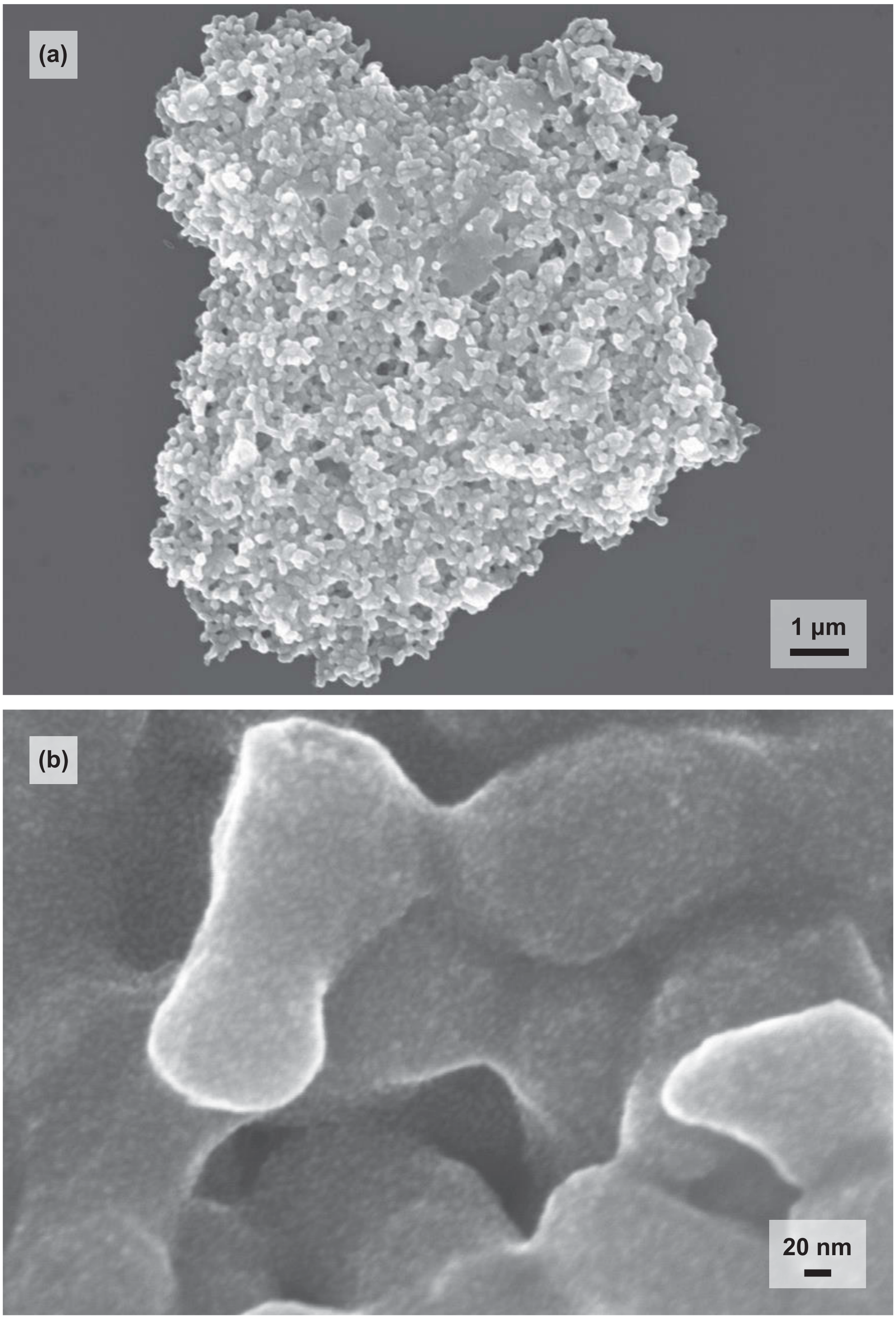

Figure A2. SEM images of precipitate from the functionalisation of OA@AuNPs with 1-butanethiol.

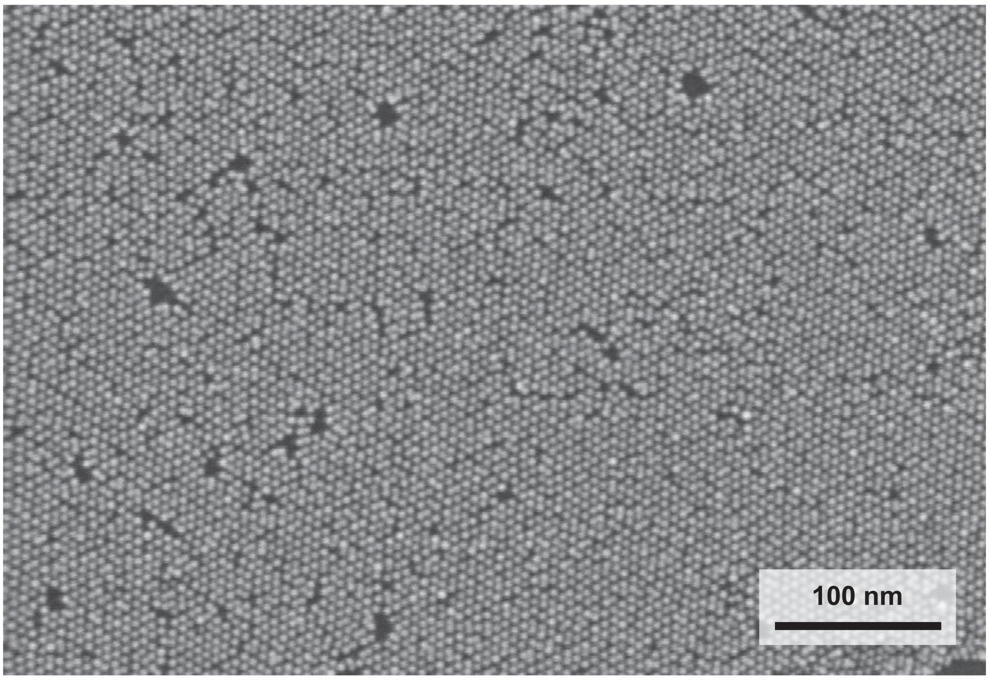

Figure A3. SEM image of OT@AuNPs.

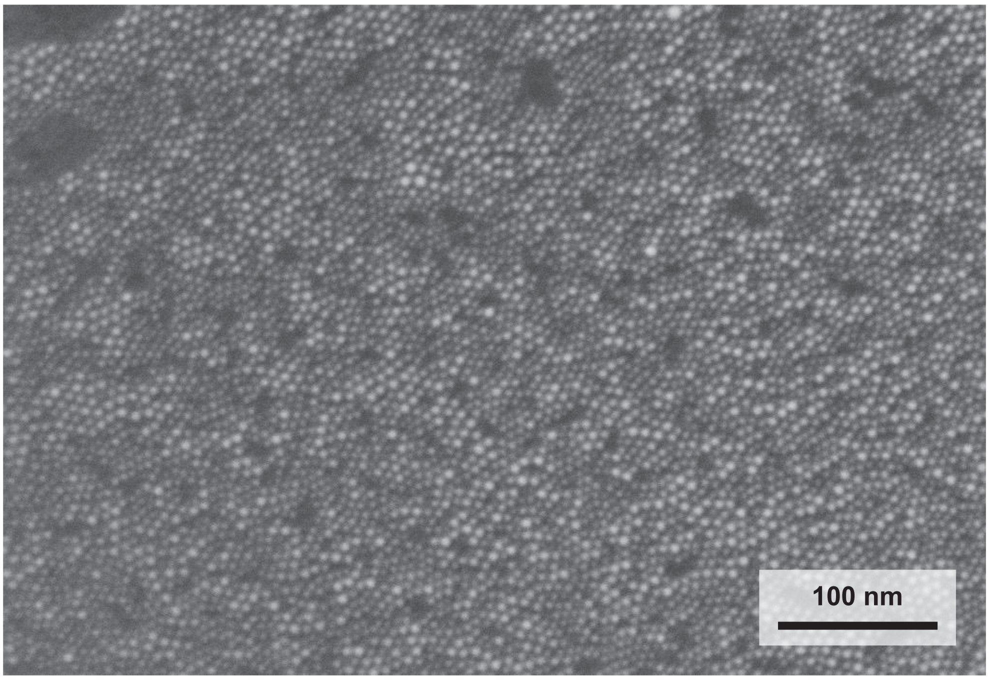

Figure A4. SEM image of DDT@AuNPs.

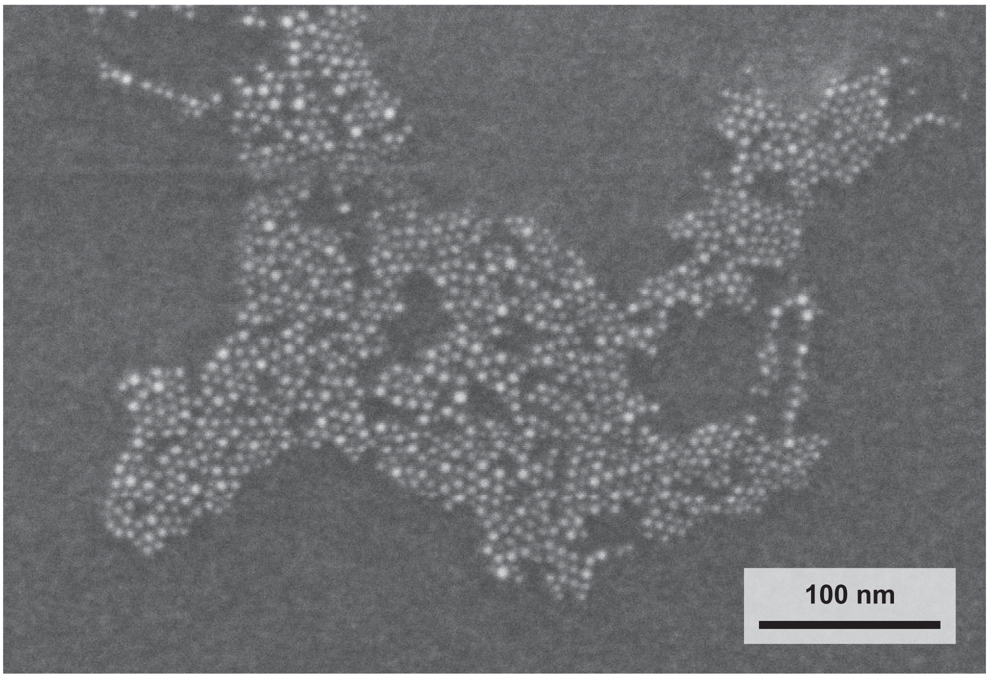

Figure A5. SEM image of HDT@AuNPs.

Functionalising AuNPs with PyBuSH did not result in the formation of any precipitate, and the particles resembled the original OA@AuNPs in terms of their size and shape (Figure A6).

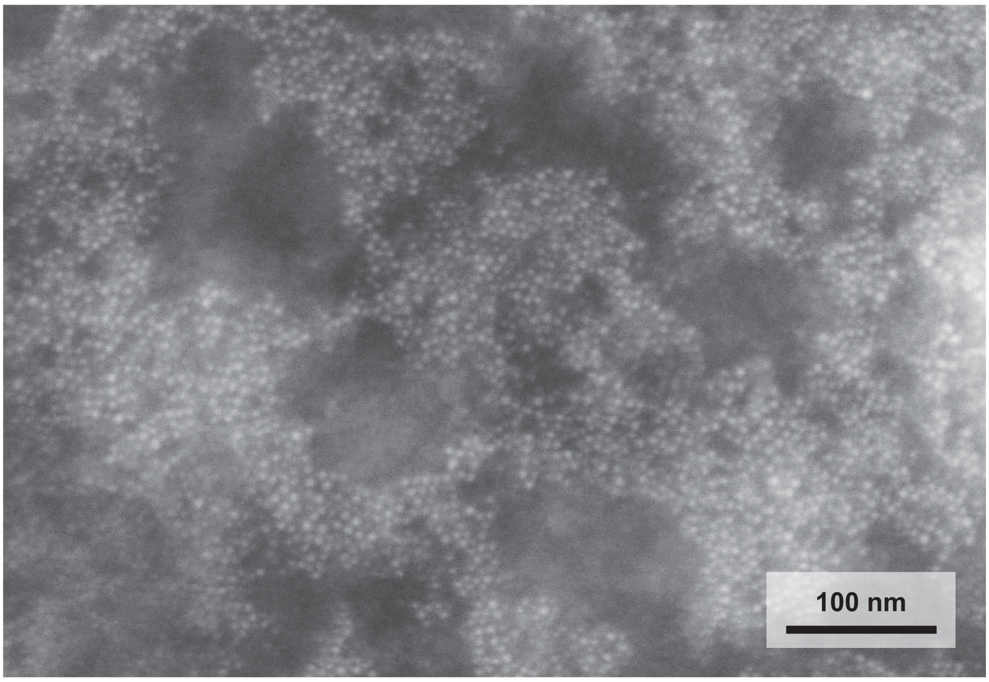

Figure A6. SEM image of Py@AuNPs.

A.2. TEM of AuNPs

TEM images were taken of OA@AuNPs (Figure A7) and BT@AuNPs (Figures A8 and A9) in order to more clearly determine the particle diameters.

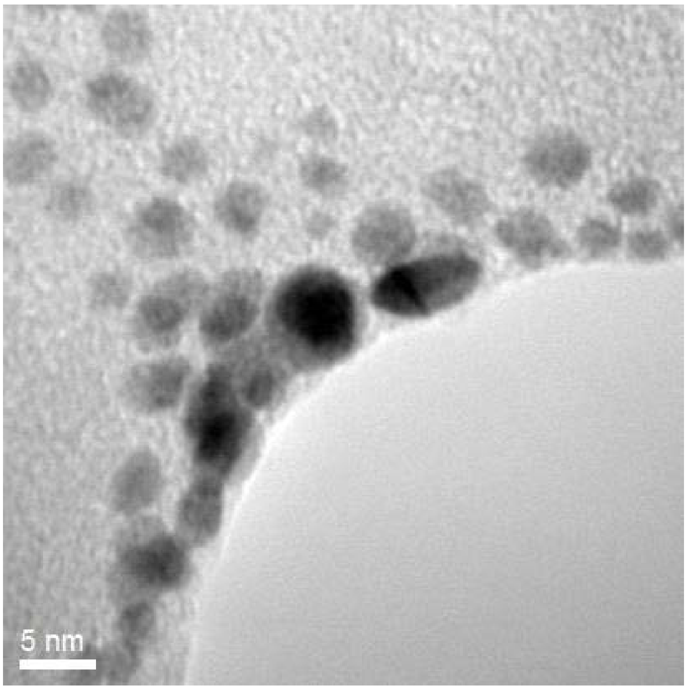

Figure A7. TEM image of OA@AuNPs, taken by Mr Daniel Totonjian (UTS).

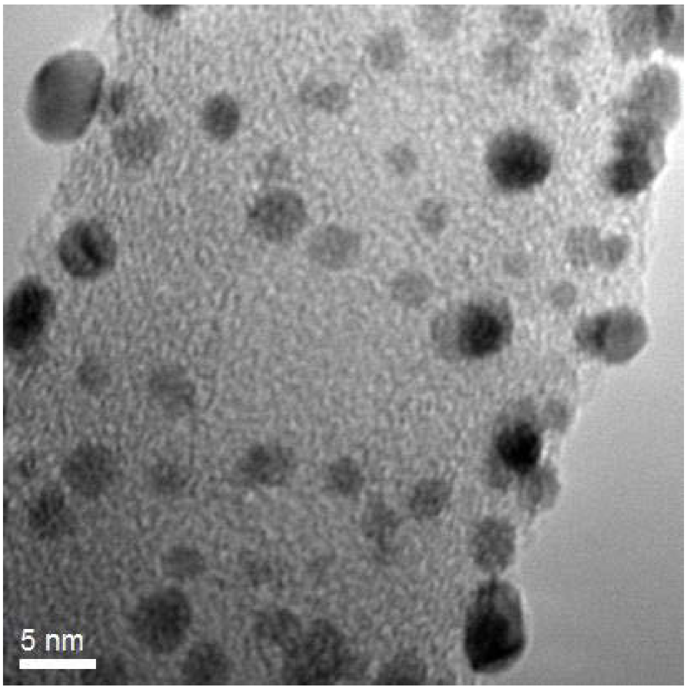

Figure A8. TEM image of BT@AuNPs, taken by Mr Daniel Totonjian (UTS).

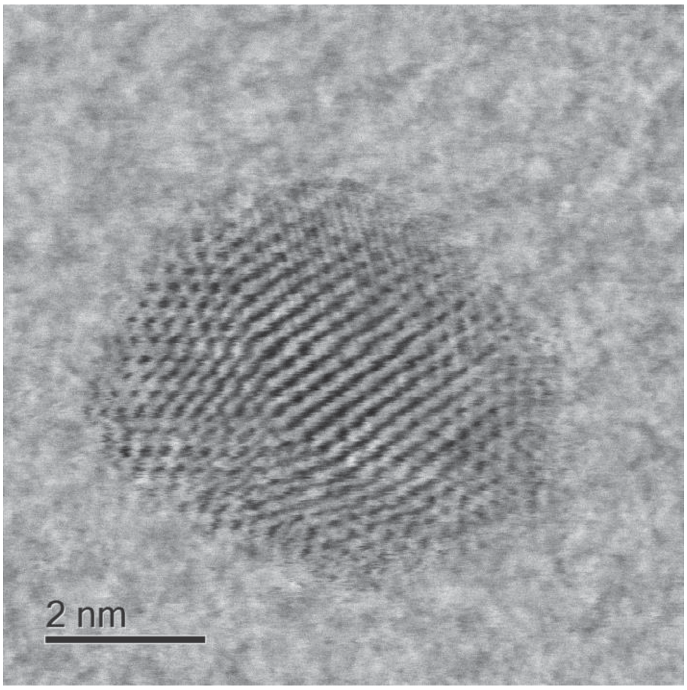

Figure A9. TEM image of a BT@AuNP, taken by Dr David Mitchell (UOW).

References

(1) ASTM International. E 2456-06 Terminology for Nanotechnology. *Annual Book of ASTM Standards*. ASTM International 2006, pp 1–5.

(2) Cortie, M. B. The Weird World of Nanoscale Gold. *Gold Bull.* **2004**, *37* (1–2), 12–19.

(3) Daniel, M.-C.; Astruc, D. Gold Nanoparticles: Assembly, Supramolecular Chemistry, Quantum-Size-Related Properties, and Applications toward Biology, Catalysis, and Nanotechnology. *Chem. Rev.* **2004**, *104* (1), 293–346.

(4) Faraday, M. The Bakerian Lecture: Experimental Relations of Gold (and Other Metals) to Light. *Philos. Trans. R. Soc. London* **1857**, *147*, 145–181.

(5) Feynman, R. P. There's Plenty of Room at the Bottom. *Eng. Sci.* **1960**, *23*, 22–36.

(6) Kreuter, J.; Täuber, U.; Illi, V. Distribution and Elimination of Poly(methyl-2-^{14}C-methacrylate) Nanoparticle Radioactivity after Injection in Rats and Mice. *J. Pharm. Sci.* **1979**, *68* (11), 1443–1447.

(7) Saha, K.; Agasti, S. S.; Kim, C.; Li, X.; Rotello, V. M. Gold Nanoparticles in Chemical and Biological Sensing. *Chem. Rev.* **2012**, *112* (5), 2739–2779.

(8) Zijlstra, P.; Chon, J. W. M.; Gu, M. Five-Dimensional Optical Recording Mediated by Surface Plasmons in Gold Nanorods. *Nature* **2009**, *459* (7245), 410–413.

(9) Rosi, N. L.; Mirkin, C. A. Nanostructures in Biodiagnostics. *Chem. Rev.* **2005**, *105* (4), 1547–1562.

(10) Giljohann, D. A.; Seferos, D. S.; Daniel, W. L.; Massich, M. D.; Patel, P. C.; Mirkin, C. A. Gold Nanoparticles for Biology and Medicine. *Angew. Chem. Int. Ed. Engl.* **2010**, *49* (19), 3280–3294.

(11) Beija, M.; Salvayre, R.; Lauth-de Viguerie, N.; Marty, J.-D. Colloidal Systems for Drug Delivery: From Design to Therapy. *Trends Biotechnol.* **2012**, *30* (9), 485–496.

(12) Stratakis, M.; Garcia, H. Catalysis by Supported Gold Nanoparticles: Beyond Aerobic Oxidative Processes. *Chem. Rev.* **2012**, *112* (8), 4469–4506.

(13) Bishop, P. T.; Ashfield, L. J.; Berzins, A.; Boardman, A.; Buche, V.; Cookson, J.; Gordon, R. J.; Salcianu, C.; Sutton, P. A. Printed Gold for Electronic Applications. *Gold Bull.* **2010**, *43* (3), 181–188.

(14) Ko, H.; Singamaneni, S.; Tsukruk, V. V. Nanostructured Surfaces and Assemblies as SERS Media. *Small* **2008**, *4* (10), 1576–1599.

(15) Coutts, M. J.; Cortie, M. B.; Ford, M. J.; McDonagh, A. M. Rapid and Controllable Sintering of Gold Nanoparticle Inks at Room Temperature Using a Chemical Agent. *J. Phys. Chem. C* **2009**, *113* (4), 1325–1328.

(16) Cortie, M. B.; Coutts, M. J.; Ton-That, C.; Dowd, A.; Keast, V. J.; McDonagh, A. M. On the Coalescence of Nanoparticulate Gold Sinter Ink. *J. Phys. Chem. C* **2013**, *117* (21), 11377–11384.

(17) Wünscher, S.; Abbel, R.; Perelaer, J.; Schubert, U. S. Progress of Alternative Sintering Approaches of Inkjet-Printed Metal Inks and Their Application for Manufacturing of Flexible Electronic Devices. *J. Mater. Chem. C* **2014**, *2* (48), 10232–10261.

(18) Hansen, T. W.; Delariva, A. T.; Challa, S. R.; Datye, A. K. Sintering of Catalytic Nanoparticles: Particle Migration or Ostwald Ripening? *Acc. Chem. Res.* **2012**, *46* (8), 1720–1730.

(19) Korotcenkov, G.; Brinzari, V.; Cho, B. K. Conductometric Gas Sensors Based on Metal Oxides Modified with Gold Nanoparticles: A Review. *Microchim. Acta* **2016**, *183* (3), 1033–1054.

(20) Gupta, A.; Mandal, S.; Katiyar, M.; Mohapatra, Y. N. Film Processing Characteristics of Nano Gold Suitable for Conductive Application on Flexible Substrates. *Thin Solid Films* **2012**, *520* (17), 5664–5670.

(21) Watanabe, A. Laser Sintering of Metal Nanoparticle Film. *J. Photopolym. Sci. Technol.* **2013**, *26* (2), 199–205.

(22) Chen, Y.; Palmer, R. E.; Wilcoxon, J. P. Sintering of Passivated Gold Nanoparticles under the Electron Beam. *Langmuir* **2006**, *22* (6), 2851–2855.

(23) Voorhees, P. W. The Theory of Ostwald Ripening. *J. Stat. Phys.* **1985**, *38* (1–2), 231–252.

(24) Wang, F.; Richards, V. N.; Shields, S. P.; Buhro, W. E. Kinetics and Mechanisms of Aggregative Nanocrystal Growth. *Chem. Mater.* **2014**, *26* (1), 5–21.

(25) Bartholomew, C. H. Mechanisms of Catalyst Deactivation. *Appl. Catal. A Gen.* **2001**, *212* (1–2), 17–60.

(26) Bore, M. T.; Pham, H. N.; Switzer, E. E.; Ward, T. L.; Fukuoka, A.; Datye, A. K. The Role of Pore Size and Structure on the Thermal Stability of Gold Nanoparticles within Mesoporous Silica. *J. Phys. Chem. B* **2005**, *109* (7), 2873–2880.

(27) Lehtinen, K. E. J.; Zachariah, M. R. Effect of Coalescence Energy Release on the Temporal Shape Evolution of Nanoparticles. *Phys. Rev. B* **2001**, *63* (20), 205402.

(28) Lehtinen, K. E. J.; Zachariah, M. R. Energy Accumulation in Nanoparticle Collision and Coalescence Processes. *J. Aerosol Sci.* **2002**, *33* (2), 357–368.

(29) Martin, J. E.; Odinek, J.; Wilcoxon, J. P.; Anderson, R. A.; Provencio, P. Sintering of Alkanethiol-Capped Gold and Platinum Nanoclusters. *J. Phys. Chem. B* **2003**, *107* (2), 430–434.

(30) Smith, B. L.; Hutchison, J. E. Transformations during Sintering of Small ($D_{\mathrm{core}} < 2$ nm) Ligand-Stabilized Gold Nanoparticles: Influence of Ligand Functionality and Core Size. *J. Phys. Chem. C* **2013**, *117* (47), 25127–25137.

(31) Huang, D.; Liao, F.; Molesa, S.; Redinger, D.; Subramanian, V. Plastic-Compatible Low Resistance Printable Gold Nanoparticle Conductors for Flexible Electronics. *J. Electrochem. Soc.* **2003**, *150* (7), G412–G417.

(32) Joseph, Y.; Guse, B.; Nelles, G. Aging of 1,ω-Alkyldithiol Interlinked Au Nanoparticle Networks. *Chem. Mater.* **2009**, *21* (8), 1670–1676.

(33) Yu, Y.; Goodfellow, B. W.; Rasch, M. R.; Bosoy, C.; Smilgies, D.; Korgel, B. A. Role of Halides in the Ordered Structure Transitions of Heated Gold Nanocrystal Superlattices. *Langmuir* **2015**, *31* (24), 6924–6932.

(34) Shim, J.-H.; Lee, B.-J.; Cho, Y. W. Thermal Stability of Unsupported Gold Nanoparticle: A Molecular Dynamics Study. *Surf. Sci.* **2002**, *512* (3), 262–268.

(35) Lewis, L. J.; Jensen, P.; Barrat, J.-L. Melting, Freezing, and Coalescence of Gold Nanoclusters. *Phys. Rev. B* **1997**, *56* (4), 2248–2257.

(36) Buffat, P.; Borel, J. P. Size Effect on the Melting Temperature of Gold Particles. *Phys. Rev. A* **1976**, *13* (6), 2287–2298.

(37) Sambles, J. R. An Electron Microscope Study of Evaporating Gold Particles: The Kelvin Equation for Liquid Gold and the Lowering of the Melting Point of Solid Gold Particles. *Proc. R. Soc. A Math. Phys. Eng. Sci.* **1971**, *324* (1558), 339–351.

(38) Dick, K.; Dhanasekaran, T.; Zhang, Z.; Meisel, D. Size-Dependent Melting of Silica-Encapsulated Gold Nanoparticles. *J. Am. Chem. Soc.* **2002**, *124* (10), 2312–2317.

(39) Wu, Y.; Li, Y.; Liu, P.; Gardner, S.; Ong, B. S. Studies of Gold Nanoparticles as Precursors to Printed Conductive Features for Thin-Film Transistors. *Chem. Mater.* **2006**, *18* (19), 4627–4632.

(40) Polavarapu, L.; Manga, K. K.; Yu, K.; Ang, P. K.; Cao, H. D.; Balapanuru, J.; Loh, K.

P.; Xu, Q.-H. Alkylamine Capped Metal Nanoparticle "Inks" for Printable SERS Substrates, Electronics and Broadband Photodetectors. *Nanoscale* **2011**, *3* (5), 2268–2274.

(41) Deng, M.; Zhang, X.; Zhang, Z.; Xin, Z.; Song, Y. A Gold Nanoparticle Ink Suitable for the Fabrication of Electrochemical Electrode by Inkjet Printing. *J. Nanosci. Nanotechnol.* **2014**, *14* (7), 5114–5119.

(42) Liana, D. D.; Raguse, B.; Wieczorek, L.; Baxter, G. R.; Chuah, K.; Gooding, J. J.; Chow, E. Sintered Gold Nanoparticles as an Electrode Material for Paper-Based Electrochemical Sensors. *RSC Adv.* **2013**, *3* (23), 8683.

(43) Anklekar, R. M.; Bauer, K.; Agrawal, D. K.; Roy, R. Improved Mechanical Properties and Microstructural Development of Microwave Sintered Copper and Nickel Steel PM Parts. *Powder Metall.* **2005**, *48* (1), 39–46.

(44) Allen, M.; Alastalo, A.; Suhonen, M.; Mattila, T.; Leppäniemi, J.; Seppä, H. Contactless Electrical Sintering of Silver Nanoparticles on Flexible Substrates. *IEEE Trans. Microw. Theory Tech.* **2011**, *59* (5), 1419–1429.

(45) Reinhold, I.; Hendriks, C. E.; Eckardt, R.; Kranenburg, J. M.; Perelaer, J.; Baumann, R. R.; Schubert, U. S. Argon Plasma Sintering of Inkjet Printed Silver Tracks on Polymer Substrates. *J. Mater. Chem.* **2009**, *19* (21), 3384.

(46) Buso, D.; Post, M.; Cantalini, C.; Mulvaney, P.; Martucci, A. Gold Nanoparticle-Doped TiO_2 Semiconductor Thin Films: Gas Sensing Properties. *Adv. Funct. Mater.* **2008**, *18* (23), 3843–3849.

(47) Ohodnicki Jr., P. R.; Buric, M. P.; Brown, T. D.; Matranga, C.; Wang, C.; Baltrus, J.; Andio, M. Plasmonic Nanocomposite Thin Film Enabled Fiber Optic Sensors for Simultaneous Gas and Temperature Sensing at Extreme Temperatures. *Nanoscale* **2013**, *5* (19), 9030–9039.

(48) Ohodnicki Jr., P. R. A Review and Perspective: Thin Films for Optical Based Chemical Sensing at Extreme Temperatures. *2012 Futur. Instrum. Int. Work. Proc.* **2012**, 1–4.

(49) Ohodnicki Jr., P. R.; Wang, C.; Natesakhawat, S.; Baltrus, J. P.; Brown, T. D. In-Situ and Ex-Situ Characterization of TiO_2 and Au Nanoparticle Incorporated TiO_2 Thin Films for Optical Gas Sensing at Extreme Temperatures. *J. Appl. Phys.* **2012**, *111* (6), 64311–64320.

(50) Ohodnicki Jr., P. R.; Wang, C.; Andio, M. Plasmonic Transparent Conducting Metal Oxide Nanoparticles and Nanoparticle Films for Optical Sensing Applications. *Thin Solid Films* **2013**, *539*, 327–336.

(51) Ohodnicki Jr., P. R.; Brown, T. D.; Holcomb, G. R.; Tylczak, J.; Schultz, A. M.; Baltrus, J. P. High Temperature Optical Sensing of Gas and Temperature Using Au-Nanoparticle Incorporated Oxides. *Sensors Actuators B Chem.* **2014**, *202*, 489–499.

(52) Padbury, R. P.; Halbur, J. C.; Krommenhoek, P. J.; Tracy, J. B.; Jur, J. S. Thermal Stability of Gold Nanoparticles Embedded within Metal Oxide Frameworks Fabricated by Hybrid Modifications onto Sacrificial Textile Templates. *Langmuir* **2015**, *31* (3), 1135–1141.

(53) Haruta, M. Nanoparticulate Gold Catalysts for Low-Temperature CO Oxidation. *J. New Mater. Electrochem. Syst.* **2004**, *7*, 163–172.

(54) Puértolas, B.; Mayoral, Á.; Arenal, R.; Solsona, B.; Moragues, A.; Murcia-Mascaros, S.; Amorós, P.; Hungría, A. B.; Taylor, S. H.; García, T. High-Temperature Stable Gold Nanoparticle Catalysts for Application under Severe Conditions: The Role of TiO_2 Nanodomains in Structure and Activity. *ACS Catal.* **2015**, *5* (2), 1078–1086.

(55) Lee, I.; Joo, J. B.; Yin, Y.; Zaera, F. A Yolk@Shell Nanoarchitecture for Au/TiO_2 Catalysts. *Angew. Chem.* **2011**, *123* (43), 10390–10393.

(56) Campbell, C. T.; Parker, S. C.; Starr, D. E. The Effect of Size-Dependent Nanoparticle

Energetics on Catalyst Sintering. *Science* **2002**, *298* (5594), 811–815.

(57) Parker, S. C.; Campbell, C. T. Reactivity and Sintering Kinetics of Au/TiO$_2$(110) Model Catalysts: Particle Size Effects. *Top. Catal.* **2007**, *44* (1–2), 3–13.

(58) Shivhare, A.; Chevrier, D. M.; Purves, R. W.; Scott, R. W. J. Following the Thermal Activation of Au$_{25}$(SR)$_{18}$ Clusters for Catalysis by X-Ray Absorption Spectroscopy. *J. Phys. Chem. C* **2013**, *117* (39), 20007–20016.

(59) Wang, J.; Lu, A.-H.; Li, M.; Zhang, W.; Chen, Y.-S.; Tian, D.-X.; Li, W.-C. Thin Porous Alumina Sheets as Supports for Stabilizing Gold. *ACS Nano* **2013**, *7* (6), 4902–4910.

(60) Yan, W.; Chen, B.; Mahurin, S. M.; Hagaman, E. W.; Dai, S.; Overbury, S. H. Surface Sol−Gel Modification of Mesoporous Silica Materials with TiO$_2$ for the Assembly of Ultrasmall Gold Nanoparticles. *J. Phys. Chem. B* **2004**, *108* (9), 2793–2796.

(61) Yan, W.; Mahurin, S. M.; Pan, Z.; Overbury, S. H.; Dai, S. Ultrastable Au Nanocatalyst Supported on Surface-Modified TiO$_2$ Nanocrystals. *J. Am. Chem. Soc.* **2005**, *127* (30), 10480–10481.

(62) Joo, S. H.; Park, J. Y.; Tsung, C.-K.; Yamada, Y.; Yang, P.; Somorjai, G. A. Thermally Stable Pt/Mesoporous Silica Core-Shell Nanocatalysts for High-Temperature Reactions. *Nat. Mater.* **2009**, *8* (2), 126–131.

(63) Ge, J.; Zhang, Q.; Zhang, T.; Yin, Y. Core-Satellite Nanocomposite Catalysts Protected by a Porous Silica Shell: Controllable Reactivity, High Stability, and Magnetic Recyclability. *Angew. Chem. Int. Ed. Engl.* **2008**, *47* (46), 8924–8928.

(64) Kelly, K. L.; Coronado, E.; Zhao, L. L.; Schatz, G. C. The Optical Properties of Metal Nanoparticles: The Influence of Size, Shape, and Dielectric Environment. *J. Phys. Chem. B* **2003**, *107* (3), 668–677.

(65) Ghosh, S. K.; Pal, T. Interparticle Coupling Effect on the Surface Plasmon Resonance of Gold Nanoparticles: From Theory to Applications. *Chem. Rev.* **2007**, *107* (11), 4797–4862.

(66) Petryayeva, E.; Krull, U. J. Localized Surface Plasmon Resonance: Nanostructures, Bioassays and Biosensing – A Review. *Anal. Chim. Acta* **2011**, *706* (1), 8–24.

(67) Eustis, S.; El-Sayed, M. A. Why Gold Nanoparticles Are More Precious than Pretty Gold: Noble Metal Surface Plasmon Resonance and its Enhancement of the Radiative and Nonradiative Properties of Nanocrystals of Different Shapes. *Chem. Soc. Rev.* **2006**, *35* (3), 209–217.

(68) Link, S.; El-Sayed, M. A. Size and Temperature Dependence of the Plasmon Absorption of Colloidal Gold Nanoparticles. *J. Phys. Chem. B* **1999**, *103* (21), 4212–4217.

(69) Chen, Y.; Cheng, W. DNA-Based Plasmonic Nanoarchitectures: From Structural Design to Emerging Applications. *Wiley Interdiscip. Rev. Nanomed. Nanobiotechnol.* **2012**, *4* (6), 587–604.

(70) Lee, J.-H.; Jun, Y.-W.; Yeon, S.-I.; Shin, J.-S.; Cheon, J. Dual-Mode Nanoparticle Probes for High-Performance Magnetic Resonance and Fluorescence Imaging of Neuroblastoma. *Angew. Chem. Int. Ed. Engl.* **2006**, *45* (48), 8160–8162.

(71) Jain, P. K.; El-Sayed, M. A. Plasmonic Coupling in Noble Metal Nanostructures. *Chem. Phys. Lett.* **2010**, *487* (4–6), 153–164.

(72) Maurya, M. R.; Toutam, V. Size-Independent Parameter for Temperature-Dependent Surface Plasmon Resonance in Metal Nanoparticles. *J. Phys. Chem. C* **2016**, *120* (34), 19316–19321.

(73) Rechberger, W.; Hohenau, a.; Leitner, a.; Krenn, J. R. R. R.; Lamprecht, B.; Aussenegg, F. R. R. R. Optical Properties of Two Interacting Gold Nanoparticles. *Opt. Commun.* **2003**, *220* (1–3), 137–141.

(74) Sebba, D. S.; LaBean, T. H.; Lazarides, A. A. Plasmon Coupling in Binary Metal Core–

satellite Assemblies. *Appl. Phys. B* **2008**, *93* (1), 69–78.

(75) Chen, S.-Y.; Lazarides, A. A. Quantitative Amplification of Cy5 SERS in “Warm Spots” Created by Plasmonic Coupling in Nanoparticle Assemblies of Controlled Structure. *J. Phys. Chem. C* **2009**, *113* (28), 12167–12175.

(76) Gandra, N.; Singamaneni, S. “Clicked” plasmonic Core-Satellites: Covalently Assembled Gold Nanoparticles. *Chem. Commun.* **2012**, *48* (94), 11540–11542.

(77) Gellner, M.; Steinigeweg, D.; Ichilmann, S.; Salehi, M.; Schütz, M.; Kömpe, K.; Haase, M.; Schlücker, S. 3D Self-Assembled Plasmonic Superstructures of Gold Nanospheres: Synthesis and Characterization at the Single-Particle Level. *Small* **2011**, *7* (24), 3445–3451.

(78) Yeshchenko, O. A.; Bondarchuk, I. S.; Gurin, V. S.; Dmitruk, I. M.; Kotko, A. V. Temperature Dependence of the Surface Plasmon Resonance in Gold Nanoparticles. *Surf. Sci.* **2013**, *608*, 275–281.

(79) Kreibig, U. Electronic Properties of Small Silver Particles: The Optical Constants and Their Temperature Dependence. *J. Phys. F Met. Phys.* **1974**, *4* (7), 999–1014.

(80) Doremus, R. H. Optical Properties of Small Gold Particles. *J. Chem. Phys.* **1964**, *40* (8), 2389–2396.

(81) King, S. R.; Massicot, J.; McDonagh, A. M. A Straightforward Route to Tetrachloroauric Acid from Gold Metal and Molecular Chlorine for Nanoparticle Synthesis. *Metals* **2015**, *5* (3), 1454–1461.

(82) King, S. R.; Shimmon, S.; Gentle, A. R.; Westerhausen, M. T.; Dowd, A.; McDonagh, A. M. Remarkable Thermal Stability of Gold Nanoparticles Functionalised with Ruthenium Phthalocyanine Complexes. *Nanotechnology* **2016**, *27* (21), 215702.

(83) King, S. R.; Shimmon, S.; Totonjian, D. D.; McDonagh, A. M. Influence of Bound versus Non-Bound Stabilizing Molecules on the Thermal Stability of Gold Nanoparticles. *J. Phys. Chem. C* **2017**, *121* (25), 13944–13951.

(84) Wright, J. R.; Crowley, J. D.; Lucas, N. T. Carbon-Rich “Click” 1,2,3-Triazoles: Hexaphenylbenzene and Hexa-Peri-Hexabenzocoronene-Based Ligands for Suzuki–Miyaura Catalysts. *Chem. Commun.* **2016**, *52* (88), 12976–12979.

(85) Skoog, D. A.; West, D. M.; Holler, F. J. *Fundamentals of Analytical Chemistry*, 6th ed.; Saunders College Publishing: Sydney, 1992, pp 373–374.

(86) Puvvada, G. V. K.; Murthy, D. S. R. Selective Precious Metals Leaching from a Chalcopyrite Concentrate Using Chloride/Hypochlorite Media. *Hydrometallurgy* **2000**, *58* (3), 185–191.

(87) Choi, H.; Chen, W. T.; Kamat, P. V. K. Know Thy Nano Neighbor. Plasmonic versus Electron Charging Effects of Metal Nanoparticles in Dye-Sensitized Solar Cells. *ACS Nano* **2012**, *6* (5), 4418–4427.

(88) Yang, Y.; Yan, Y.; Wang, W.; Li, J. Precise Size Control of Hydrophobic Gold Nanoparticles Using Cooperative Effect of Refluxing Ripening and Seeding Growth. *Nanotechnology* **2008**, *19*, 175603.

(89) Turkevich, J.; Stevenson, P. C.; Hillier, J. A Study of the Nucleation and Growth Process in the Synthesis of Colloidal Gold. *Discuss. Faraday Soc.* **1951**, *11*, 55–75.

(90) Choi, M. J.; Smoother, T.; Martin, A. A.; McDonagh, A. M.; Maynard, P. J.; Lennard, C.; Roux, C. Fluorescent TiO_2 Powders Prepared Using a New Perylene Diimide Dye: Applications in Latent Fingermark Detection. *Forensic Sci. Int.* **2007**, *173* (2–3), 154–160.

(91) Battistini, G.; Cozzi, P. G.; Jalkanen, J. P.; Montalti, M.; Prodi, L.; Zaccheroni, N.; Zerbetto, F. The Erratic Emission of Pyrene on Gold Nanoparticles. *ACS Nano* **2008**, *2* (1), 77–84.

(92) Han, C.-C.; Balakumar, R. Mild and Efficient Methods for the Conversion of Benzylic Bromides to Benzylic Thiols. *Tetrahedron Lett.* **2006**, *47* (47), 8255–8258.

(93) Bossard, G. E.; Abrams, M. J.; Darkes, M. C.; Vollano, J. F.; Brooks, R. C. Convenient Synthesis of Water Soluble, Isomerically Pure Ruthenium Phthalocyanine Complexes. *Inorg. Chem.* **1995**, *34* (6), 1524–1527.

(94) Rawling, T.; Austin, C. E.; Hare, D.; Doble, P. A.; Zareie, H. M.; McDonagh, A. M. Thin Films of Ruthenium Phthalocyanine Complexes. *Nano Res.* **2009**, *2* (9), 678–687.

(95) Farrell, N. P.; Murray, A. J.; Thornback, J. R.; Dolphin, D. H.; James, B. R. Phthalocyanine Complexes of Ruthenium(II). *Inorganica Chim. Acta* **1978**, *28*, L144–L146.

(96) Bastin, G. F.; Heijligers, H. J. M.; Van Loo, F. J. J. The Performance of the Modified ϕ(ρz) Approach as Compared to the Love and Scott, Ruste and Standard ZAF Correction Procedures in Quantitative Electron Probe Microanalysis. *Scanning* **1984**, *6* (1), 58–68.

(97) Goldstein, J.; Newbury, D. E.; Echlin, P.; Joy, D. C.; Romig Jr, A. D.; Lyman, C. E.; Fiori, C.; Lifshin, E. *Scanning Electron Microscopy and X-Ray Microanalysis: A Text for Biologists, Materials Scientists, and Geologists*; Springer Science & Business Media, 2012.

(98) Nam, K. S.; Jung, B. H.; An, J. W.; Ha, T. J.; Tran, T.; Kim, M. J. Use of Chloride–Hypochlorite Leachants to Recover Gold from Tailing. *Int. J. Miner. Process.* **2008**, *86*, 131–140.

(99) Mellor, J. W. *A Comprehensive Treatise on Inorganic and Theoretical Chemistry*, 2nd ed.; Longmans, Green and Co. Ltd.: London, 1928; Vol. 3, pp 491–618.

(100) Konyratbekova, S. S.; Baikonurova, A.; Akcil, A. Non-Cyanide Leaching Processes in Gold Hydrometallurgy and Iodine-Iodide Applications: A Review. *Miner. Process. Extr. M.* **2014**, *36* (3), 198–212.

(101) French, A. Process of Obtaining Gold, Silver and Copper from Ores. *U.S. Pat. Off.* **1893**, US490193.

(102) La Brooy, S. R.; Linge, H. G.; Walker, G. S. Review of Gold Extraction from Ores. *Miner. Eng.* **1994**, *7* (10), 1213–1241.

(103) Syed, S. Recovery of Gold from Secondary Sources – A Review. *Hydrometallurgy* **2012**, *115–116*, 30–51.

(104) Kallmes, J. Improvement in Treating Gold and Silver Ores. *U.S. Pat. Off.* **1873**, US138500.

(105) Hasab, M. G.; Rashchi, F.; Raygan, S. Chloride–Hypochlorite Oxidation and Leaching of Refractory Sulfide Gold Concentrate. *Physicochem. Probl. Miner. Process.* **2013**, *49* (1), 61–70.

(106) Simpson, C. H. Chlorination Process for Removing Precious Metals from Ore. *U.S. Pat. Off.* **1984**, US4439235.

(107) Marczenko, Z.; Kowalski, T. The Extraction of Gold(III) from Nitric Acid Medium. *Anal. Chim. Acta* **1984**, *156* (C), 193–199.

(108) Turkevich, J. Colloidal Gold. Part II Colour, Coagulation, Adhesion, Alloying and Catalytic Properties. *Gold Bull.* **1985**, *18* (4), 125–131.

(109) Chakravorty, A. U.V. Spectrum of $KAuCl_4$. *Naturwissenschaften* **1961**, *48* (9), 375.

(110) Gangopadhayay, A. K.; Chakravorty, A. Charge Transfer Spectra of Some Gold(III) Complexes. *J. Chem. Phys.* **1961**, *35* (6), 2206–2209.

(111) Carlin, R. L. *Transition Metal Chemistry*; Marcel Dekker, Inc.: New York, 1965, pp 245–253.

(112) Diaz, M. A.; Kelsall, G. H.; Welham, N. J. Electrowinning Coupled to Gold Leaching by Electrogenerated Chlorine: I. Au(III)–Au(I)/Au Kinetics in Aqueous Cl_2/Cl^- Electrolytes.

J. Electroanal. Chem. **1993**, *361* (1–2), 25–38.

(113) Sun, T. M.; Yen, W. T. Kinetics of Gold Chloride Adsorption onto Activated Carbon. *Miner. Eng.* **1993**, *6* (1), 17–29.

(114) Viñals, J.; Núñez, C.; Herroros, O. Kinetics of the Aqueous Chlorination of Gold in Suspended Particles. *Hydrometallurgy* **1995**, *38*, 125–147.

(115) Alkan, M.; Oktay, M.; Kocakerim, M. M.; Çopur, M. Solubility of Chlorine in Aqueous Hydrochloric Acid Solutions. *J. Hazard. Mater.* **2005**, *119* (1–3), 13–18.

(116) Wang, S.; Qian, K.; Bi, X.; Huang, W. Influence of Speciation of Aqueous $HAuCl_4$ on the Synthesis, Structure, and Property of Au Colloids. *J. Phys. Chem. C* **2009**, *113* (16), 6505–6510.

(117) Peck, J. A.; Tait, C. D.; Swanson, B. I.; Brown Jr, G. E. Speciation of Aqueous Gold(III) Chlorides from Ultraviolet/Visible Absorption and Raman/Resonance Raman Spectroscopies. *Geochim. Cosmochim. Ac.* **1991**, *55* (3), 671–676.

(118) Moreau, F.; Bond, G. C.; Taylor, A. O. Gold on Titania Catalysts for the Oxidation of Carbon Monoxide: Control of pH during Preparation with Various Gold Contents. *J. Catal.* **2005**, *231* (1), 105–114.

(119) Robb, W. Kinetics and Mechanisms of Reactions of Gold(III) Complexes. I. The Equilibrium Hydrolysis of Tetrachlorogold(III) in Acid Medium. *Inorg. Chem.* **1967**, *6* (2), 382–386.

(120) Eustis, S. Gold and Silver Nanoparticles: Characterization of Their Interesting Optical Properties and the Mechanism of Their Photochemical Formation, Georgia Institute of Technology, 2006.

(121) Huang, Z.; Geyer, N.; Werner, P.; De Boor, J.; Gösele, U. Metal- Assisted Chemical Etching of Silicon: A Review. *Adv. Mater.* **2011**, *23* (2), 285–308.

(122) Dubois, L. H.; Nuzzo, R. G. Synthesis, Structure, and Properties of Model Organic Surfaces. *Annu. Rev. Phys. Chem.* **1992**, *43* (1), 437–463.

(123) Frens, G. Controlled Nucleation for the Regulation of the Particle Size in Monodisperse Gold Suspensions. *Nat. Phys. Sci.* **1973**, *241*, 20–22.

(124) Brust, M.; Walker, M.; Bethell, D.; Schiffrin, D. J.; Whyman, R. Synthesis of Thiol-Derivatised Gold Nanoparticles in a Two-Phase Liquid-Liquid System. *J. Chem. Soc. Chem. Commun.* **1994**, No. 7, 801–802.

(125) Hoft, R. C.; Ford, M. J.; McDonagh, A. M.; Cortie, M. B. Adsorption of Amine Compounds on the Au(111) Surface: A Density Functional Study. *J. Phys. Chem. C* **2007**, *111* (37), 13886–13891.

(126) Bürgi, T. Properties of the Gold–Sulphur Interface: From Self-Assembled Monolayers to Clusters. *Nanoscale* **2015**, *7* (38), 15553–15567.

(127) Malola, S.; Lehtovaara, L.; Enkovaara, J.; Häkkinen, H. Birth of the Localized Surface Plasmon Resonance in Monolayer-Protected Gold Nanoclusters. *ACS Nano* **2013**, *7* (11), 10263–10270.

(128) Zhang, J. Z.; Noguez, C. Plasmonic Optical Properties and Applications of Metal Nanostructures. *Plasmonics* **2008**, *3* (4), 127–150.

(129) Kneipp, K.; Kneipp, H.; Kneipp, J. Surface-Enhanced Raman Scattering in Local Optical Fields of Silver and Gold Nanoaggregates – From Single-Molecule Raman Spectroscopy to Ultrasensitive Probing in Live Cells. *Acc. Chem. Res.* **2006**, *39* (7), 443–450.

(130) Xue, Y.; Li, X.; Li, H.; Zhang, W. Quantifying Thiol-Gold Interactions towards the Efficient Strength Control. *Nat. Commun.* **2014**, *5*, 4348.

(131) Mourdikoudis, S.; Liz-Marzan, L. M. Oleylamine in Nanoparticle Synthesis. *Chem. Mater.* **2013**, *25*, 1465–1476.

(132) Nyokong, T.; Antunes, E. Influence of Nanoparticle Materials on the Photophysical

Behavior of Phthalocyanines. *Coord. Chem. Rev.* **2013**, *257* (15–16), 2401–2418.

(133) Ishii, K. Functional Singlet Oxygen Generators Based on Phthalocyanines. *Coord. Chem. Rev.* **2012**, *256*, 1556–1568.

(134) Linstead, R. P. Phthalocyanines. Part I. A New Type of Synthetic Colouring Matters. *J. Chem. Soc.* **1934**, No. 0, 1016–1017.

(135) Rawling, T.; McDonagh, A. Ruthenium Phthalocyanine and Naphthalocyanine Complexes: Synthesis, Properties and Applications. *Coord. Chem. Rev.* **2007**, *251*, 1128–1157.

(136) de la Torre, G.; Claessens, C. G.; Torres, T. Phthalocyanines: Old Dyes, New Materials. Putting Color in Nanotechnology. *Chem. Commun.* **2007**, No. 20, 2000–2015.

(137) Han, M.; Zhang, X.; Zhang, X.; Liao, C.; Zhu, B.; Li, Q. Azo-Coupled Zinc Phthalocyanines: Towards Broad Absorption and Application in Dye-Sensitized Solar Cells. *Polyhedron* **2015**, *85*, 864–873.

(138) Forteath, S.; Antunes, E.; Chidawanyika, W.; Nyokong, T. Unquenched Fluorescence Lifetime for β-Phenylthio Substituted Zinc Phthalocyanine upon Conjugation to Gold Nanoparticles. *Polyhedron* **2012**, *34*, 114–120.

(139) Dynich, R. A.; Ponyavina, A. N.; Filippov, V. V. Effect of the Material of Metal Nanoparticles on Local Field Intensification in Copper Phthalocyanine. *Opt. Spectrosc.* **2011**, *110* (6), 909–915.

(140) Stuzhin, P. A.; Vagin, S. I.; Hanack, M. Synthesis and Spectral Properties of Bisaxially Coordinated (Octaphenyltetraazaporphyrinato)ruthenium(II) Complexes. *Inorg. Chem.* **1998**, *37* (11), 2655–2662.

(141) Presland, A. E. B.; Price, G. L.; Trimm, D. L. Kinetics of Hillock and Island Formation during Annealing of Thin Silver Films. *Prog. Surf. Sci.* **1972**, *3* (1), 63–96.

(142) Rolison, D. R.; Hagans, P. L.; Swider, K. E.; Long, J. W. Role of Hydrous Ruthenium Oxide in Pt–Ru Direct Methanol Fuel Cell Anode Electrocatalysts: The Importance of Mixed Electron/Proton Conductivity. *Langmuir* **1999**, *15* (3), 774–779.

(143) Campbell, P. F.; Ortner, M. H.; Anderson, C. J. Differential Thermal Analysis and Thermogravimetric Analysis of Fission Product Oxides and Nitrates to 1500 °C. *Anal. Chem.* **1961**, *33* (1), 58–61.

(144) Snow, A. W. Phthalocyanine Aggregation. In *The Porphyrin Handbook. Phthalocyanines: Properties and Materials*; Kadish, K. M., Smith, K. M., Guilard, R., Eds.; Academic Press: New York, 2003; p 130.

(145) Goworek, J.; Kierys, A.; Gac, W.; Borówka, A.; Kusak, R. Thermal Degradation of CTAB in As-Synthesized MCM-41. *J. Therm. Anal. Calorim.* **2009**, *96* (2), 375–382.

(146) Kleitz, F.; Schmidt, W.; Schüth, F. Evolution of Mesoporous Materials during the Calcination Process: Structural and Chemical Behavior. *Microporous Mesoporous Mater.* **2001**, *44–45*, 95–109.

(147) Kruk, M.; Jaroniec, M.; Sayari, A. A Unified Interpretation of High-Temperature Pore Size Expansion Processes in MCM-41 Mesoporous Silicas. *J. Phys. Chem. B* **1999**, *103*, 4590–4598.

(148) Kota, R.; Samudrala, R.; Mattern, D. L. Synthesis of Donor-σ-Perylenebisimide-Acceptor Molecules Having PEG Swallowtails and Sulfur Anchors. *J. Org. Chem.* **2012**, *77* (21), 9641–9651.

(149) Dressel, M.; Scheffler, M. Verifying the Drude Response. *Ann. der Phys.* **2006**, *15* (7–8), 535–544.

(150) Gadenne, P.; Beghdadi, A.; Lafait, J. Optical Cross-over Analysis of Granular Gold Films at Percolation. *Opt. Commun.* **1988**, *65* (1), 17–21.

(151) Brandt, T.; Hövel, M.; Gompf, B.; Dressel, M. Temperature- and Frequency-Dependent

Optical Properties of Ultrathin Au Films. *Phys. Rev. B – Condens. Matter Mater. Phys.* **2008**, *78* (20), 1–7.

(152) Hardy, N. J.; Richardson, T. H. Temperature Effects on the Optical Properties of Thiol Encapsulated Gold Nanoparticle Thin Films. *Colloids Surfaces A Physicochem. Eng. Asp.* **2008**, *321* (1–3), 285–291.

(153) Abbas, R. R.; Richardson, T. H.; Hobson, A.; Hassan, A.; Abbas, T. R. Effect of Annealing on the Surface Plasmon Resonance of Dodecanethiol Encapsulated Gold Nanoparticles Langmuir-Schafer Thin Films. *Colloids Surfaces A Physicochem. Eng. Asp.* **2014**, *444*, 95–103.

(154) Švorčík, V.; Kvítek, O.; Lyutakov, O.; Siegel, J.; Kolská, Z. Annealing of Sputtered Gold Nano-Structures. *Appl. Phys. A Mater. Sci. Process.* **2011**, *102* (3), 747–751.

(155) Wang, Y. C.; Lu, L.; Gunasekaran, S. Biopolymer/Gold Nanoparticles Composite Plasmonic Thermal History Indicator to Monitor Quality and Safety of Perishable Bioproducts. *Biosens. Bioelectron.* **2017**, *92*, 109–116.

(156) Lü, Y.; Molodov, D. A.; Gottstein, G. Recrystallization Kinetics and Microstructure Evolution during Annealing of a Cold-Rolled Fe-Mn-C Alloy. *Acta Mater.* **2011**, *59* (8), 3229–3243.

(157) Pellegrini, G.; Mattei, G.; Bello, V.; Mazzoldi, P. Interacting Metal Nanoparticles: Optical Properties from Nanoparticle Dimers to Core-Satellite Systems. *Mater. Sci. Eng. C* **2007**, *27* (5–8), 1347–1350.

(158) Babar, S.; Weaver, J. H. Optical Constants of Cu, Ag, and Au Revisited. *Appl. Opt.* **2015**, *54* (3), 477–481.

(159) Maxwell Garnett, J. C. Colours in Metal Glasses, in Metallic Films, and in Metallic Solutions – II. *Philos. Trans. R. Soc. London* **1906**, *205*, 237–288.

(160) Stepanov, A. L.; Hole, D. E.; Townsend, P. D. Reflectance of the Dielectric Layers Containing Metal Nanoparticles Formed by Ion Implantation. *J. Non. Cryst. Solids* **1999**, *244* (2–3), 275–279.

(161) Thompson, C. V. Solid-State Dewetting of Thin Films. *Annu. Rev. Mater. Res.* **2012**, *42* (1), 399–434.